Department of Physics and Astronomy

Heidelberg University

Master thesis

in Physics

submitted by

Oliver Diekmann

born in Dillingen a.d. Donau

2021

Inverse design of artificial few-level schemes with Mössbauer nuclei in thin-film cavities

This Master thesis has been carried out by Oliver Diekmann

at the

Max Planck Institute for Nuclear Physics, Heidelberg

under the supervision of

apl. Prof. Dr. Jörg Evers

Inverses Design künstlicher Wenig-Zustands-Quantensysteme mit Mössbauer-Kernen in Dünnschicht-Kavitäten:

In der vorliegenden Masterarbeit wird ein Ansatz zum inversen Design künstlicher quantenoptischer Wenig-Zustands-Systeme im Bereich harter Röntgenstrahlung entwickelt. Derartige Quantensysteme lassen sich mit Schichten schwach getriebener Mössbauer-Kerne in Dünnschicht-Kavitäten verwirklichen. Der in dieser Arbeit verfolgte inverse Ansatz erlaubt es, umfassend zu untersuchen, welche quantenoptischen Schemata realisiert werden können und gibt unmittelbaren Zugang zu den entsprechenden Geometrien der Kavitäten. Die Konstruktion der Kavitäten durch Ausprobieren kann weitgehend durch die entwickelte Methode ersetzt werden. Aufgrund der systematischen Natur des inversen Designs ergeben sich allgemeine und teils unerwartete Erkenntnisse, die womöglich auch die Entwicklung anderer Resonatoren im Röntgenbereich beeinflussen werden. Der Ansatz wird zuerst am Beispiel eines künstlichen Zwei-Level-Systems vorgestellt. Anschließend wird die Verallgemeinerung auf komplexere Niveau-Schemata anhand des Designs von quantenoptischen Effekten im Rahmen eines künstlichen Drei-Level-Systems veranschaulicht. Jenseits dessen kann das inverse Design auch direkt zur Gestaltung des experimentell messbaren Reflektionsspektrums des Kern-Kavität-Systems verwendet werden. Der entwickelte Ansatz verspricht, bestehende Anwendungen zu verbessern und wird mit großer Wahrscheinlichkeit dazu beitragen, den Anwendungsbereich der Röntgenquantenoptik um neue Ideen zu erweitern.

Inverse design of artificial few-level schemes with Mössbauer nuclei in thin-film cavities:

In this thesis, an inverse design approach to the engineering of quantum optical few-level schemes at hard x-ray energies is introduced. Such quantum systems can be realized with layers of Mössbauer nuclei embedded in thin-film cavities and probed with low-intensity x-rays. The approach pursued in the thesis allows to comprehensively study the realizable quantum optical setups and gives immediate access to the geometries they are realized in. This feature alleviates the need for trial-and-error methods and – due to its systematic nature – enables general and partly unexpected insights that might impact x-ray cavities beyond the system under study. The approach is introduced using the example of an artificial two-level scheme and its generalization to more complex level schemes is illustrated with the design of quantum optical effects in an artificial three-level system. Finally, the inverse design is applied to directly shape the observable spectrum of the joint nuclei-cavity system. The results of the thesis promise to enlarge the performance of existing applications and will likely help to extend the scope of x-ray quantum optics towards novel ideas.

Within the framework of this thesis, the following articles were submitted for publication in refereed journals:

[1] Oliver Diekmann, Dominik Lentrodt, and Jörg Evers. Inverse design of artificial two-level systems with Mössbauer nuclei in thin-film cavities. arXiv:2108.01960 [quant-ph], August 2021. URL http://arxiv.org/abs/2108.01960

Outside the scope of this thesis, the following articles were submitted for publication in refereed journals:

[2] Dominik Lentrodt, Oliver Diekmann, Christoph H. Keitel, Stefan Rotter, and Jörg Evers. Classifying and harnessing multi-mode light-matter interaction in lossy resonators. arXiv:2107.11775 [quant-ph], July 2021. URL http://arxiv.org/abs/2107.11775

The thesis author's role in the publication [1] is that of the sole principal author. Part of the publication has been reproduced verbatim throughout the thesis with permission of the coauthors.

Contents

1 Introduction

At present, a multitude of applications making use of quantum mechanics, so-called *quantum technologies*, are experiencing tremendous advancement, both in academia as well as industrially [3–6]. The trend towards deliberately using the quantum advantage over classical systems to perform tasks better or more efficiently is commonly termed the *second quantum revolution* [5, 7]. Where the *first quantum revolution* is thought to have explained the foundations of quantum mechanics, the second one goes beyond and enables the development of technologies, or in the words of Dowling and Milburn [7],

> *"The difference between science and technology is the ability to engineer your surroundings to your own ends, and not just explain them."*

A key ingredient to many emerging quantum technologies has been progress in the field of quantum optics [8–10]. Among a multitude of examples, schemes of quantum computation [11], quantum simulation [12], quantum communication [13] and quantum metrology [14] have been developed on the basis of photonic technologies. Using integrated designs, photonic quantum technologies are guided to a stage where scalability and industrial mass production become feasible [15, 16].

Much of the progress in quantum optics was achieved with light of visible, infrared or microwave frequencies (see [17, 18] and references therein). Opposed to that, the comparatively new field of x-ray quantum optics – the field which this thesis is situated in – strives to realize quantum optical setups at far higher energies [19]. The major reason for the imbalance in the development of x-ray quantum optics is found in the lack of intense coherent light sources [20, 21] comparable to lasers at longer wavelengths. However, x-ray photons themselves also feature properties that are desirable for quantum optics, e.g., a high quantum efficiency in detection [18] and superior focusing capabilities [22]. With the realization and suggestion of ever more powerful x-ray sources [23–26], the field of x-ray quantum optics has gained considerable momentum [18, 27, 28]. On that basis, advancing quantum optical setups in the x-ray regime paves the way towards future x-ray quantum technologies.

Besides using electronic transitions, a complementary approach to x-ray quantum optics is to employ the extreme properties of transitions in Mössbauer nuclei [29–41]. Being subject to the Mössbauer effect, the nuclei may emit and absorb photons with negligible recoil and thus exhibit exceptionally small linewidths [43–45]. The most prominent representative employed in the field of nuclear quantum optics is the ^{57}Fe isotope, which in the absence of magnetic fields can be treated as a two-level system

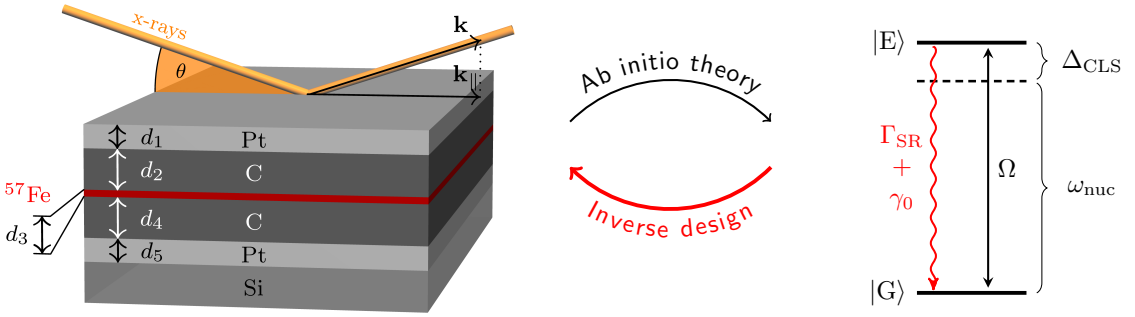

Fig. 1.1: Schematic setup of an archetypal thin-film cavity system and illustration of its relation to the artificial two-level scheme. The cavity consists of a stack of different layers (thicknesses and exemplary materials are indicated) and a single, thin layer of Mössbauer nuclei (here: ^{57}Fe). The cavity is illuminated in grazing incidence with x-rays near-resonant to the nuclear transition frequency. θ, $\boldsymbol{k}$ and $\boldsymbol{k}_\parallel$ are the x-ray incidence angle, the wave vector, and its projection onto the cavity surface, respectively. At low probing intensities, the system features an effective description as an artificial two-level system. As compared to the bare two-level system of individual nuclei with transition frequency ω_{nuc} and decay rate γ_0, it is driven by a cavity- and collectively enhanced Rabi-frequency Ω, and features a level shift Δ_{CLS} and a decay rate enhancement Γ_{SR}. A recently developed ab initio theory allows one to readily derive the artificial level scheme from a given cavity structure [48]. In this thesis, we introduce and develop the *inverse design* of such artificial few-level systems, i.e., we determine cavity structures suitable to the realization of desired level schemes.

with a transition frequency of 14.4 keV and a linewidth as small as 4.7 neV [46]. Such small linewidths correspond to desirably long coherence lifetimes, but also render the strong driving of Mössbauer nuclei a challenge, even at accelerator based x-ray sources. A particularly promising approach to nevertheless work with the nuclei is, firstly, to take a macroscopically large number of nuclei [$\mathcal{O}(10^{23})$], and secondly, to couple the nuclei to one another by placing them in a photonic structure. In the spirit of the Dicke *superatom* [47], the dynamics can then be described in terms of a collectively excited state of the nuclei. This state does not only show enhanced decay, but also has strongly increased coupling to the external driving field.

Efficiently coupling the nuclei by the modes of a photonic structure requires design capabilities on the scale of the light's wavelength. For Mössbauer nuclei, the wavelengths usually lie in the sub-Ångström regime (^{57}Fe: $\lambda = 86\,\mathrm{pm}$) which is below standard lattice constants and hence prevents the design on these scales. One can, however, overcome this problem by using so-called thin-film cavities. The most archetypal setup comprises a guiding layer sandwiched between two cladding layers, where layer thicknesses typically lie on the nm-scale. A layer of Mössbauer nuclei – commonly referred to as *resonant layer* – can then be placed inside the guiding layer, see Fig. 1.1(left). When the structure is probed in grazing incidence, that is at very small angles θ, the top and bottom layers act as mirrors and a standing wave can form normal to the layer surfaces. From a technical perspective, due to the grazing incidence setup, the wave number in this direction is significantly reduced and hence

the effective wavelength normal to the layers enhanced to the nm-scale. Using this waveguide-like setup thus allows the design of a photonic environment at hard x-ray energies.

The key property making the joint nuclei-cavity system of Fig. 1.1 particularly interesting for x-ray quantum optics is that it features an effective description as a two-level scheme in the experimentally relevant low-excitation regime [49]. The levels of the two-level system comprise the true many-body ground state $|\mathrm{G}\rangle$ and a collectively excited state $|\mathrm{E}\rangle$ where a single excitation is coherently spread across all nuclei – the latter we will refer to as a nuclear exciton in the layer. The properties of this collective state strongly depend on the couplings between the nuclei, which are dictated by the cavity. Changing the cavity's geometry thus allows to tune the driving Rabi-frequency, decay rate and transition energy, where the bare properties of the Mössbauer nuclei serve as a reference, see Fig. 1.1(right).

While the inclusion of a single layer of nuclei amounts to the realization of an artificial two-level scheme, more complicated level schemes can be designed embedding several resonant layers into a thin-film cavity. In this case, several collectively excited states take part in the dynamics, and, notably, also cavity-mediated coherent and incoherent couplings between the excited states can be present. These processes are of great interest as they can take the role of coherent driving fields which may compensate for the unavailability of suitable lasers with fixed phase relation in the x-ray regime. In this way, Mössbauer nuclei allow for the realization of advanced quantum optical level schemes otherwise unavailable at hard x-ray energies.

Within this platform for x-ray quantum optics, a number of setups have already been realized experimentally. Among these, one finds the realization of the collective Lamb shift (CLS) and superradiance (SR) [50], electromagnetically induced transparency (EIT) [51], vacuum generated coherences [52], realization of strong coupling [53], Rabi-oscillations [54] and sub-luminal propagation of x-ray pulses [55].

Regarding the theoretical description, extensive work has been devoted to the precise characterization of the nuclear dynamics in the cavity and the resulting observables. Initially, the nuclei-cavity systems were interpreted phenomenologically as effective level schemes on the basis of the experimentally accessible linear reflection spectrum that can be calculated within the semi-classical layer formalism [46, 50, 51]. A quantum optical few-mode theory was subsequently able to provide justification of the level scheme description on a microscopic basis [49, 56]. Remaining inconsistencies in the description were resolved with the introduction of an ab initio few-mode theory [48]. Finally, theories were developed that allow one to calculate the level scheme's parameters on the basis of the electromagnetic Green's function of the thin-film cavity [48, 57]. In particular, the ab initio theory [48] allows for the calculation of the level scheme without the need for any fitting procedure. Since the Green's function for the thin-film cavity is known analytically [58] the level scheme can be calculated efficiently.

While the work cited above primarily focused on the precise description of the nuclear dynamics and the resulting artificial level schemes, this thesis shall – much in the spirit of the above quote by Dowling and Milburn – provide the means *"to engineer your surroundings to your own ends"* in the realm of x-ray quantum optics with Mössbauer nuclei. So far, most suggested and realized setups within the platform have been developed on the basis of intuition and optimized by trial-and-error approaches. However, this is not only cumbersome, but also limits the scope of quantum optical setups by the ever incomplete understanding of the underlying physical processes. A systematic approach to the assessment and design of level-schemes is thus indispensable to exploit the full potential of x-ray cavities with Mössbauer nuclei.

Central results and insights

In the course of this thesis, we develop such an approach on the basis of the ab initio theory in [48]. We address the question which level schemes can be realized with Mössbauer nuclei in thin-film cavities and specify how to realize them. Being able to give explicit cavity geometries for accessible few-level schemes, we implement their *inverse design* [59–61].

To introduce and develop the inverse design, much of the thesis is devoted to the archetypal system shown in Fig. 1.1 – a single resonant layer of nuclei which is associated with a two-level scheme. We provide a comprehensive determination of the accessible properties of this scheme and explain these based on the cavity's underlying mode structure. To each possible choice of properties, we are able to give the explicit cavity geometry, thus achieving the inverse design. We find, however, that two-level schemes with extreme properties are typically not observable experimentally. To allow for a quantitative balance between accessible properties and experimental observability, we introduce a visibility criterion and show how it relates to the properties of the two-level scheme.

While implementing the inverse design, we find a number of unexpected insights into the properties of thin-film cavities with Mössbauer nuclei. Firstly, for practically relevant settings, omitting the top cladding layer can be beneficial for the performance. This comes unexpected as in the analogy to conventional cavities, this would correspond to removing one of the mirrors. Within the grazing incidence operation of the cavities, however, also the guiding material-air interface can take the role of a moderate mirror.

Secondly, our analysis reveals that the decay enhancement Γ_{SR} and the driving Rabi-frequency Ω are maximized in opposite cavity geometries. For standard cavities, however, the maxima of driving field and decay enhancement can typically be expected to coincide. We illustrate this feature by considering the same quantities for a two-level system in a one-dimensional Fabry-Pérot cavity and ultimately find the grazing incidence regime to be the reason for the qualitative difference.

To arrive at a comprehensive discussion of the artificial two-level schemes, we further study the influence of different layer materials on the accessible properties of the two-level scheme. Our results show that low absorption in the cladding layer is significant and suggest that employing a *low-Z cladding – lower-Z guiding* paradigm (where Z is the atomic number) for the materials choice, the performance of thin-film cavity systems can be enhanced. This is surprising as commonly materials are chosen along a *high-Z cladding – low-Z guiding* guideline to enhance the refractive index contrast, and thus the reflectivity, at the cladding-guiding interface.

To conclude the description of artificial two-level schemes, we consider the influence of different Mössbauer isotopes on the capabilities of the inverse design. We find that the intrinsic nuclear properties are not sufficient to evaluate the performance, but the isotope's impact on the photonic environment has to be taken into account.

To illustrate the applicability of the inverse design approach to more complex setups, we subsequently address thin-film cavities comprising two resonant layers. The corresponding level scheme can be shown to involve the ground state and two excited states. One of the archetypal quantum optical setups [62, 63] that can be realized with such a three-level system is the EIT scheme [51, 56]. In its common form, a transition between an upper and a lower level is weakly probed while a strong control laser field couples the upper state to a third one. When the probing field is on resonance with the transition between upper and lower state, it can be shown that instead of the maximal absorption, the probe field can pass the three-level scheme without attenuation in a narrow frequency window – the medium is rendered transparent by the control field.

As the outset of the discussion on artificial three-level systems, we determine the accessible properties for a scheme realized in a cavity setting analogous to Fig. 1.1, but with a second resonant layer embedded in the guiding layer. Analyzing the setup, we find that due to the common mode structure, the properties of the three-level scheme have similar dependencies, e.g., on the angle of incidence, and thus cannot be tuned fully independently from one another. Therefore, a systematic approach to the design is highly beneficial.

On this basis, we then show that not only the inverse design of three-level systems is possible within our approach, but also the design of level scheme parameter ratios which is relevant for tailoring the quantum dynamics in such systems.

We further find that many of the qualitative insights obtained for a single resonant layer, e.g., the significance of low absorption in the cladding or the relevance of cavities without upper cladding, readily extend to the case of multiple layers of nuclei.

Using the example of the EIT scheme, we show that we can design relevant nuclear quantum optical effects. The results suggest, however, that not all interesting nuclear dynamics imprint themselves onto the reflection spectrum. This is possible because

the calculation of the reflection spectrum comprises an additional step of coupling out of the cavity that affects the visible nuclear response.

An alternative approach to the problem is not to consider the bare excitons in both resonant layers, but to diagonalize their non-hermitian coupling matrix. This gives direct access to the spectral imprint of the resulting nuclear excitonic normal modes. On this basis, the suppression of certain spectral signatures can indeed be explained.

Moreover, introducing the description with excitonic normal modes leads to a significant reduction of the number of relevant level-scheme parameters and thus greatly simplifies the inverse design problem for several layers of nuclei. To illustrate the potential, we show that it is possible to suppress the influence of one normal mode while the second one exhibits decay enhancement beyond what is possible with a single resonant layer in an analogous setting. This establishes a two-level scheme with superior tuning capabilities. Only by a systematic analysis of the accessible properties for the normal modes, and the subsequent inverse design, it was possible to reach this novel regime. These results certify the relevance of the inverse design approach also for systems with several resonant layers and illustrate the method's applicability to the design of the observable reflection spectrum.

Brief outline of the thesis

In Chapter 2, the foundations of the description of Mössbauer nuclei in thin-film cavities are presented. Sec. 2.1 introduces the classical description of empty thin-film cavities using simple examples and demonstrates the calculation of relevant observables. Sec. 2.2 revises the quantum optical treatment of nuclei in a thin-film cavity based on the electromagnetic Green's function and derives the description as effective few-level scheme as well as general expressions for the linear reflection spectrum.

In Chapter 3, artificial two-level systems are introduced and exemplified with simple systems. Sec. 3.1 specializes the general theory to the case of a single resonant layer and defines a visibility criterion for the spectral response of the nuclei. Sec. 3.2 subsequently illustrates general properties of the relevant Green's function using the example of a ^{56}Fe/^{57}Fe/^{56}Fe single-layer cavity.

In Chapter 4, the inverse design of artificial two-level schemes is introduced and applied to archetype cavity systems. Sec. 4.1 derives and explains the accessible frequency shifts and decay enhancements. Sec. 4.2 adds the experimental visibility criterion as a design goal. Sec. 4.3 incorporates the intra-cavity field enhancement into the design and highlights differences in the accessible parameters for optical Fabry-Pérot cavities. Finally, Sec. 4.4 and 4.5 discuss the influence of the material and Mössbauer isotope choice on the two-level scheme design, respectively.

In Chapter 5, the inverse design of three-level systems is considered for cavities comprising two resonant layers. Sec. 5.1 adapts the artificial level scheme description

to two resonant layers and derives the reflection spectrum. Sec. 5.2 discusses accessible level-scheme properties in a typical cavity setup and their dependencies on one another. In Sec. 5.3, the inverse approach is applied to design level scheme parameter ratios. Sec. 5.4 discusses the engineering of an EIT effect in a nuclear three-level scheme and raises some open questions regarding the interpretation of the effect. Sec. 5.5 introduces the description of the nuclear response by excitonic normal modes to interpret the spectral response of the cavity-nuclei system and eventually establishes a two-level scheme with enhanced tuning capabilities on the basis of two resonant layers.

In Chapter 6, the numerical methods to determine the accessible properties of few-level schemes are introduced and discussed.

Finally, Chapter 7 summarizes the results and outlines future perspectives.

2 Theoretical description

In this chapter, we introduce the necessary theoretical tools that enable us to describe, and on that basis design, artificial level schemes from Mössbauer nuclei in thin-film cavities. We start out by considering classical observables and their calculation for empty thin-film cavities, i.e., cavities without resonant nuclei. This sets the stage to subsequently revise the quantum optical description of Mössbauer nuclei embedded in such cavities, derive the effective level schemes and give expressions for the reflection spectrum including the nuclear response.

2.1 Empty cavity – Parratt's formalism

Fundamental observables of thin-film cavities are the reflected and transmitted intensity. For an empty cavity these can be calculated using Parratt's formalism [64]. The formalism provides the means to recursively solve for the response of a stratified medium, that is a stack of layers made of different materials, to an incident plane-wave in frequency space [65]. In the absence of any polarization scattering media, which is assumed in this thesis, s- and p-polarization can be treated independently from one another. Since both treatments are analogous and become equivalent for grazing incidence illumination [65], we restrict the analysis to the case of s-polarization. In order to acquaint ourselves with thin-film cavities, we consider simple single-layer systems that can readily be generalized to more complicated layer stacks. In Sec. 2.1.1, we introduce the calculation of the reflected intensity using a layer deposited on a perfect mirror. Here, we also showcase the Mittag-Leffler pole expansion [66–68] that will become important in Chapter 4. Subsequently, in Sec. 2.1.2, we calculate the transmitted intensity for a single layer surrounded by vacuum.

2.1.1 Vacuum/layer/mirror-system

As a first system, we consider a single slab of material deposited on a perfect mirror and probed with x-ray light under a small angle θ, i.e., in grazing incidence, see Fig. 2.1(a). To calculate the response of this simple cavity system with Parratt's formalism, different scattering pathways contributing to the reflected intensity in Fig. 2.1(b) are summed up. This finally leads to a field configuration that is consistent with the incoming plane-wave as well as the boundary conditions imposed by Maxwell's equations [17].

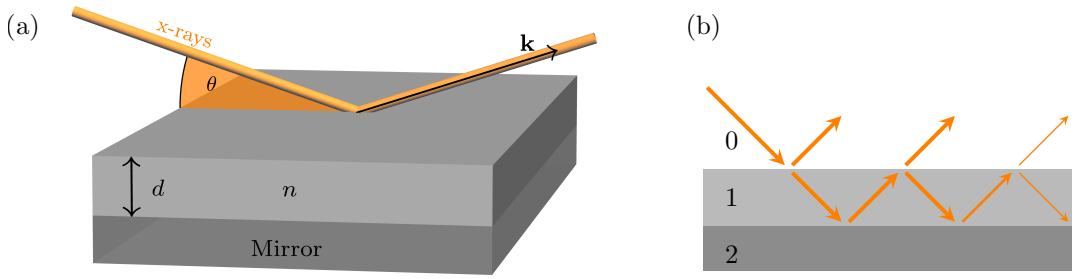

Fig. 2.1: Single layer thin-film cavity deposited on a perfect mirror. (a) The layer of thickness d and refractive index n is probed in grazing incidence under an angle θ with light of wave vector $\boldsymbol{k}$. (b) Schematic representation of the scattering pathways contributing to the calculation in Parratt's formalism.

The lowest order contribution to the reflection coefficient for an incident s-polarized plane-wave with wave number k and the wave number's component normal to the surface, $\beta_0 = k \sin\theta$, is given by the Fresnel coefficient [65],

$$r_{01} = \frac{\beta_0 - \beta_1}{\beta_0 + \beta_1}\,. \tag{2.1}$$

Here, θ is the angle between the surface of the layer and the incident wave vector. For the grazing incidence regime it typically takes values of a few mrad. Further, β_1 is the z-component of the refracted wave vector in the medium, given by

$$\beta_1 = \sqrt{n^2k^2 - (k^2 - \beta_0^2)} = k\sqrt{n^2 - 1 + \sin^2\theta}\,. \tag{2.2}$$

Lastly, $n = n_\mathrm{R} + in_\mathrm{I}$ is the complex-valued refractive index of the layer's material. For materials at x-ray energies, this refractive index is usually written in the form

$$n = 1 - \delta + i\beta. \tag{2.3}$$

The parameters δ and β are positive and very small, leading to the materials being optically thinner than air [65] which in turn yields the effect of total external reflection. For the Fresnel reflection coefficients we use the naming convention that r_{ij} indicates the coefficient for light in material i being reflected at material j. Likewise, the transmission coefficient t_{ij} describes the transmission of light from layer i to layer j. The respective numbering of the layers can be taken from Fig. 2.1(b).

In the second order of the description of the reflected x-ray amplitude, the wave penetrates the layer of thickness d with transmission coefficient $t_{01} = 1 + r_{01}$, picks up a factor of $\exp(2i\beta_1 d)$ upon propagation as well as an additional minus sign due to the reflection at the mirror substrate and leaves the layer with transmission coefficient $t_{10} = 1 - r_{01}$. The third contribution to the reflection coefficient is additionally weighted with the Fresnel coefficient $r_{10} = -r_{01}$ and subsequently picks up another factor analogously to the previous order.

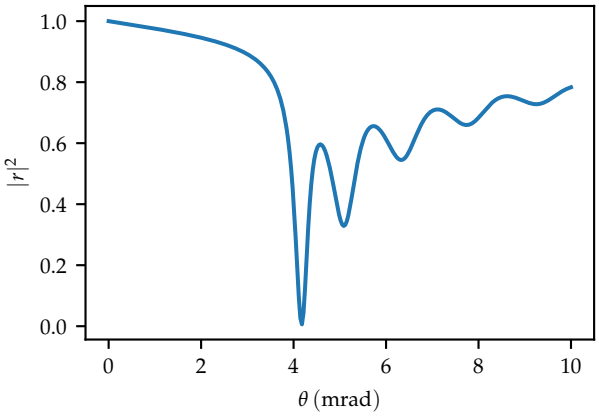

Fig. 2.2: Reflected intensity as a function of the angle of incidence θ for a 25 nm slab of iron (^{56}Fe) on top of a perfect mirror, illuminated at 14.4 keV. Modes are visible in the fringes of the rocking curve.

The total reflected amplitude thus reads

$$\begin{aligned} r &= r_{01} + t_{01}e^{2i\beta_1 d}(-1)t_{10} + t_{01}e^{2i\beta_1 d}(-1)r_{10}e^{2i\beta_1 d}(-1)t_{10} + \ldots = \\ &= r_{01} - \frac{t_{01}t_{10}}{r_{01}} \sum_{m=1}^{\infty} \left(e^{2i\beta_1 d} r_{01}\right)^m = \frac{r_{01} - e^{2i\beta_1 d}}{1 - r_{01}e^{2i\beta_1 d}} , \end{aligned} \tag{2.4}$$

where we used the geometric series in the last step.

Since k cancels in the Fresnel coefficient r_{01}, we can describe the reflection coefficient in terms of a dimensionless wave number $\kappa = kd$ and thus have

$$r = \frac{r_{01} - e^{2i\kappa\sqrt{n^2-1+\sin^2\theta}}}{1 - r_{01}e^{2i\kappa\sqrt{n^2-1+\sin^2\theta}}} . \tag{2.5}$$

Assuming a lossless medium can be used as a plausibility check. For that case, the reflected intensity should amount to one, since there is no transmission through the mirror. Abbreviating $a = e^{2i\kappa\sqrt{n^2-1+\sin^2\theta}}$, the reflected intensity reads

$$|r|^2 = \left|\frac{r_{01} - a}{1 - r_{01}a}\right|^2 = \frac{|r_{01}|^2 - r_{01}a^* - ar_{01}^* + |a|^2}{1 - r_{01}^*a^* - r_{01}a + |r_{01}a|^2} . \tag{2.6}$$

One can distinguish between the case of θ being in the range of normal reflection or total reflection, where the transition occurs sharply at the angle of total reflection for lossless media. For the prior case $r_{01} \in \mathbb{R}$ and $|a| = 1$ hold, thus directly yielding $|r|^2 = 1$. For the case of total reflection, the reflection coefficient satisfies $|r_{01}| = 1$ and with $a \in \mathbb{R}$ the reflectance is again equal to one.

A typical observable of x-ray thin-film cavities is the reflected intensity at fixed x-ray wavelength as a function of the angle of incidence – typically referred to as *rocking curve*. For a thin layer of ordinary iron (i.e. not yet Mössbauer nuclei) on top of a perfect mirror, the rocking curve is shown in Fig. 2.2. For very small angles, light can only enter the cavity evanescently due to total external reflection. For higher angles, standing waves can form with respect to the wave vector component β_1

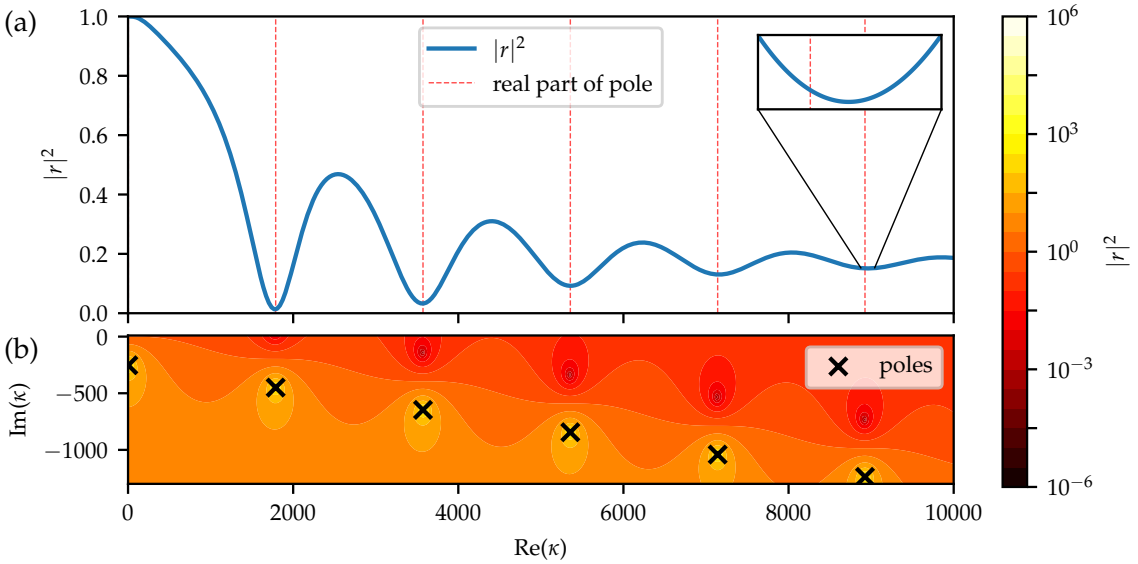

Fig. 2.3: Reflected intensity $|r|^2$ as a function of the dimensionless wave number κ for the vacuum/^{56}Fe/mirror-system at an incident angle of 4.2 mrad. (a) $|r|^2$ as a function of real κ. (b) $|r|^2$ in the complex κ plane. Poles (black xs) of $|r|^2$ and their respective real parts (red dashed lines) are marked in the figure. The inset figure in (a) illustrates the deviation of the real part of the pole from the minimum in the reflected intensity.

normal to the layer's surface. These manifest themselves as the modes of the cavity in the dips of the rocking curve [49]. Towards even higher angles, the effect of the perfectly reflecting mirror becomes dominant as the reflectivity at the vacuum/iron interface decreases due to the comparatively large angle of incidence. Besides the residual attenuation in the iron layer, the incoming light is essentially reflected. This behavior will generally not be observed in realistic thin-film cavities as we cannot realize such a perfect mirror by a simple base layer.

Mode structure and Mittag-Leffler pole expansion

Alternatively to the rocking curve, we can also look at the reflected intensity at fixed angle as a function of the frequency of the probing light. We consider this in Fig. 2.3(a), where we once again employ a ^{56}Fe layer on a perfect mirror. Each of the modes in the rocking curve can be associated to a simple pole in the complex plane [2], which we illustrate in Fig. 2.3(b). Since the algebraic structure of the reflection coefficient is simple, one can readily give analytical expressions for the poles,

$$\kappa_m = \frac{1}{2i\sqrt{n^2 - 1 + \sin^2\theta}} \left[\log\left(r_{01}^{-1}\right) + 2\pi i m\right] , \tag{2.7}$$

where $m \in \mathbb{Z}$ refers to the different branches of the logarithm and n is the refractive index of iron. In Fig. 2.3, the minima in the reflection spectrum in terms of real κ

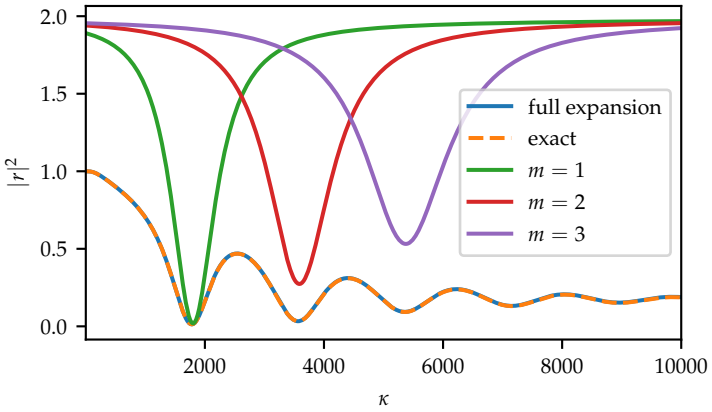

Fig. 2.4: Mittag-Leffler pole expansion for the reflected intensity as a function of κ for the vacuum/^{56}Fe/mirror-system, illuminated at $\theta = 4.2\,\text{mrad}$. The Mittag-Leffler expansion (blue curve) fits very well with the exact reflected intensity when a large number of poles (here about 1000) is taken into account. Attempting an approximation around a single pole (m is the pole index) according to Eq. (2.11), as is done for the first three poles (green, red and purple lines) in this figure, however, leads to non-physical results where the reflected intensity is partly larger than the incoming one. This is to be attributed to overlapping modes of the simple iron-layer cavity.

agree well with the real part of the corresponding κ-pole. However, in the close-up view we can see that deviations between pole and minimum positions are present which can be associated with several modes contributing to the minimum's position in the reflected intensity [2].

We find the reflection coefficient r to have well separated, simple poles such that we can heuristically assume that the conditions of the Mittag-Leffler expansion theorem [66–68] (see Appendix A.2 for the full theorem) are met. For this case, we can express the reflection coefficient as

$$r(\kappa) = r(0) + \sum_m \text{Res}(r, \kappa_m) \left(\frac{1}{\kappa - \kappa_m} + \frac{1}{\kappa_m} \right) . \tag{2.8}$$

The residues can be evaluated analytically and we find all of them to take the same value,

$$\text{Res}(r, \kappa_m) = \frac{2i \sin\theta}{n^2 - 1} . \tag{2.9}$$

Hence, we can express the total reflection coefficient as

$$r(\kappa) = -1 + \frac{2i \sin\theta}{n^2 - 1} \sum_m \left(\frac{1}{\kappa - \kappa_m} + \frac{1}{\kappa_m} \right) . \tag{2.10}$$

The convergence of the expansion is apparent from Fig. 2.4 when a sufficiently large number of poles is taken into account (blue curve). Having the above expansion

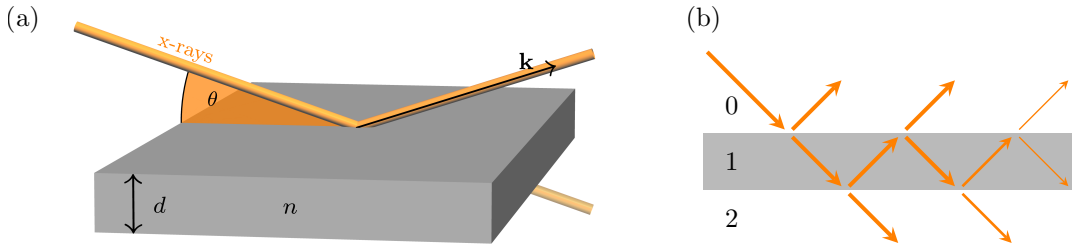

Fig. 2.5: Single layer thin-film cavity surrounded by vacuum on both sides. (a) The layer of thickness d and refractive index n is probed in grazing incidence under an angle θ with light of wave vector $\boldsymbol{k}$. (b) Schematic representation of the scattering pathways contributing to the calculation in Parratt's formalism.

suggests that, when being close to the frequency of one mode, i.e., $\kappa \approx \kappa_m$, we might be able to approximate the reflected intensity as

$$r(\kappa) \approx \mathcal{C} + \frac{2i\sin\theta}{n^2-1}\frac{1}{\kappa-\kappa_m}\,, \tag{2.11}$$

where $\mathcal{C} = -1 + \frac{2i\sin\theta}{n^2-1}\sum_m \frac{1}{\kappa_m}$. This is attempted for some poles in Fig. 2.4. The figure, however, shows that we cannot arrive at a physically meaningful approximation as the resulting approximated curves yield reflected intensities larger than one, that is they violate energy conservation. The failure of the approximation can be attributed to the overlapping mode structure of the spectrum. Only upon considering all poles contributing to a local region, the different phases of the poles can add up destructively to have an overall physical reflectance less than one. For well-separated modes, however, we will later on see that the expansion may be used to approximate relevant observables around a single mode.

In any case, the Mittag-Leffler expansion is found to be a useful tool to link cavity modes to the pole structure of cavity observables. It will play an important role in Chapter 4 and 5 of this thesis.

2.1.2 Vacuum/layer/vacuum-system

We can consider another simple system that will be instructive in the course of the thesis. Here, the mirror from the previous section is replaced by vacuum, i.e. the system acquires a mirror symmetry around the center of the layer, see Fig. 2.5. The reflection coefficient is obtained in an analogous way to the previous setup,

$$r = r_{01}\frac{1-e^{2i\kappa\sqrt{n^2-1+\sin^2\theta}}}{1-r_{01}^2 e^{2i\kappa\sqrt{n^2-1+\sin^2\theta}}}\,, \tag{2.12}$$

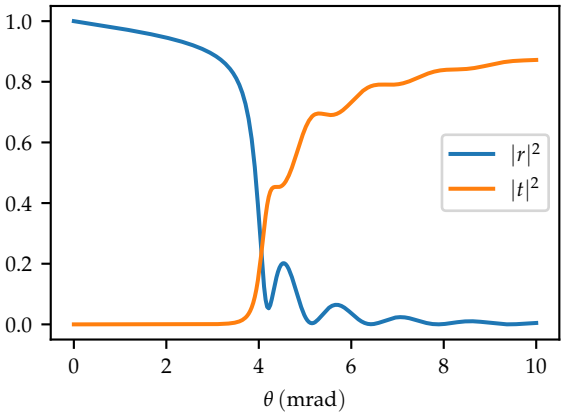

Fig. 2.6: Reflected and transmitted intensity as a function of the angle of incidence θ for a 25 nm slab of iron (^{56}Fe) illuminated at 14.4 keV.

where again $\kappa = kd$. Additionally, for the present system we can also calculate the transmission coefficient by adding up the corresponding scattering contributions in Fig. 2.5(b),

$$t = t_{01}e^{i\beta_1 d}t_{12} + t_{01}e^{i\beta_1 d}r_{12}e^{i\beta_1 d}r_{10}e^{i\beta_1 d}t_{12} + \ldots = t_{01}e^{i\beta_1 d}t_{12}\sum_{j=0}^{\infty}\left(r_{12}r_{10}e^{2i\beta_1 d}\right)^j = \\ = \frac{t_{01}e^{i\beta_1 d}t_{12}}{1 - r_{12}r_{10}e^{2i\beta_1 d}}\,. \tag{2.13}$$

Since the layer is surrounded by vacuum on both sides, we have $r_{10} = r_{12}$ and $t_{10} = t_{12}$. Therefore, we can rewrite the transmission coefficient as

$$t = \frac{(1 + r_{01})(1 - r_{01})e^{i\beta_1 d}}{1 - r_{01}^2 e^{2i\beta_1 d}}\,. \tag{2.14}$$

Fig. 2.6 shows the reflected and transmitted intensity as calculated from the formulae derived above. Modes are visible as for the respective system with mirror. Unlike the previous setup, however, the reflected intensity vanishes for larger angles as the x-rays can easily penetrate the single layer in this case.

This concludes the discussion of empty thin-film cavities. The calculations exemplified in this section readily apply to more complex cavity geometries. The reflected intensity will again be of relevance when the reflection spectrum of thin-film cavities with Mössbauer nuclei is considered.

2.2 Mössbauer nuclei in thin-film cavities – Green's function description

In this section, we revise the quantum optical description of Mössbauer nuclei in thin-film cavities. The key concept underlying the present work is the observation that in the low-excitation limit, thin-film cavities doped with large ensembles of resonant nuclei are analytically equivalent to single artificial few-level systems, see Fig. 1.1. Thereby, they form a platform to realize level schemes otherwise inaccessible at hard x-ray energies. In the following, we summarize the equations of motion governing the nuclei in the waveguide, explain the above-mentioned equivalence to a few-level system, and discuss the relevant observables, within the framework of macroscopic QED. This framework allows one to express the Hamiltonian describing the quantized light field in the cavity, and the coupling to the nuclei embedded therein, in terms of the classical electromagnetic Green's function. Details on the derivation can be found in [28, 48].

2.2.1 Nuclear many-body description in the single-particle basis

The joint dynamics of nuclei and the quantized light field in absorbing media can be described on the basis of macroscopic QED. In the absence of magnetic fields, the Mössbauer nuclei represent two-level systems. Within the Born-Markov approximation, the degrees of freedom of the quantized electromagnetic field are traced out and the system's dynamics can be described via its density operator ρ using a Master equation,

$$\dot{\rho} = -i\Big[\hat{H},\rho\Big] + \mathcal{L}[\rho]\,, \tag{2.15}$$

where we employ natural units, $\hbar = c = 1$, and denote the commutator by $[\cdot,\cdot]$. The Hamiltonian derived from macroscopic QED, given by [69, 70]

$$\hat{H} = \sum_{ln} \frac{\omega_{\mathrm{nuc}}}{2}\hat{\sigma}^z_{ln} - \sum_{ln}\sum_{l'n'} J_{ll'nn'}\hat{\sigma}^+_{ln}\,\hat{\sigma}^-_{l'n'} - \sum_{ln}\Big[\boldsymbol{d}^*_{\boldsymbol{l}}\cdot\boldsymbol{E}_{\mathrm{in}}(\boldsymbol{r}_{ln})\hat{\sigma}^+_{ln} + \mathrm{h.c.}\Big]\,, \tag{2.16}$$

is a standard many-body Hamiltonian and can be interpreted in a straightforward way. The first term describes the excitation energy of the bare nuclei enumerated by indices l, n and characterized by the Pauli operators $\hat{\sigma}^z_{ln}, \hat{\sigma}^{\pm}_{ln}$. Here, l is chosen to indicate which resonant layer the nucleus is located in (for the case of several resonant layers) and n indexes the nuclei within one resonant layer. Further, ω_{nuc} is the bare nuclear transition frequency and $\boldsymbol{d_l}$ the nuclear transition dipole moment. The second part denotes couplings between nuclei ln and $l'n'$ with coupling constant $J_{ll'nn'}$ mediated by the cavity environment (the dependence of the coupling constants on the Green's function will be defined in Sec. 2.2.3 below). The last part describes the driving of the nuclei by an externally applied classical electric field $\boldsymbol{E}_{\mathrm{in}}(\boldsymbol{r}_{ln})$ evaluated at the position of the nuclei. Note that this field in general differs from

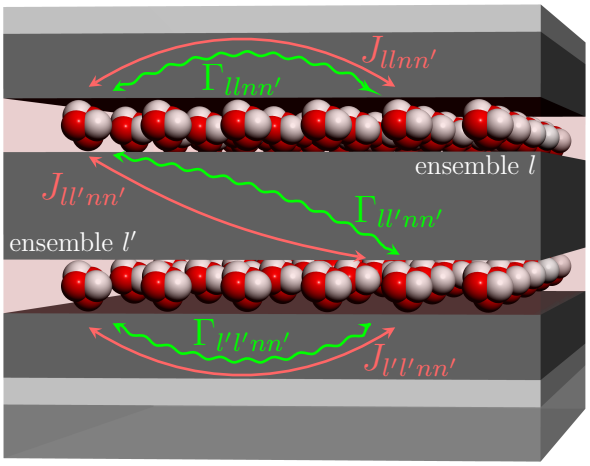

Fig. 2.7: Schematic representation of the different inter-nuclear coupling processes at the example of a two resonant layer system with resonant layers l and l'. Each layer is considered as one ensemble of nuclei although, in principle, very thick layers can be treated as several ensembles. Within one layer, the nuclei are indexed by the second index n. Note that the single nucleus decay enhancement and frequency shift as well as the external driving are not shown.

its free-space value, due to reflections and absorption in the cavity structure, as discussed in Sec. 2.2.3 below.

Similarly, the Lindbladian assumes a standard form,

$$\mathcal{L}[\rho] = \sum_{ln}\sum_{l'n'} \frac{\Gamma_{ll'nn'}}{2}\left[2\hat{\sigma}^-_{l'n'}\rho\hat{\sigma}^+_{ln} - \left\{\hat{\sigma}^+_{ln}\,\hat{\sigma}^-_{l'n'},\rho\right\}\right] + \mathcal{L}_{\mathrm{IC}}[\rho]\,, \tag{2.17}$$

where $\{\cdot,\cdot\}$ is the anti-commutator. Here, $\Gamma_{ll'nn'}$ describes spontaneous emission in the presence of the cavity environment for $ln = l'n'$, and incoherent couplings between the nuclei for $ln \neq l'n'$. The final part $\mathcal{L}_{\mathrm{IC}}[\rho]$ models the single-nucleus decay due to internal conversion with rate γ_{IC} approximately equal to the bare nuclear linewidth γ_0. Fig. 2.7 illustrates the indexing of the nuclei and shows the coherent and incoherent internuclear couplings for a structure comprising two resonant layers.

2.2.2 Nuclear few-level description in the spin-wave basis

Next, following [48], we show that in the low-excitation regime, the above many-body Master equation given by Eqs. (2.16, 2.17) can be rewritten in terms of an effective few-level system by means of a suitable basis transformation.

To motivate this basis transformation, we model the synchrotron radiation impinging in grazing incidence onto the cavity as a classical plane-wave electromagnetic field with wave vector $\boldsymbol{k}$. Due to the grazing incidence geometry, nuclei at different in-plane positions will be driven with relative phase offsets determined by the projection $\boldsymbol{k}_\parallel$ of $\boldsymbol{k}$ onto the nuclear plane (cf. Fig. 1.1). We take this into account by introducing spin-wave operators

$$\hat{\sigma}^\pm_{l,\boldsymbol{k}_\parallel} = \sum_n e^{\pm i\boldsymbol{k}_\parallel\cdot\boldsymbol{r}_{ln\parallel}}\,\hat{\sigma}^\pm_{ln}\,, \tag{2.18}$$

which describe the excitation ($\hat{\sigma}^+_{l,\boldsymbol{k}_\parallel}$) and deexcitation ($\hat{\sigma}^-_{l,\boldsymbol{k}_\parallel}$) of an excitonic spin-wave with wave vector $\boldsymbol{k}_\parallel$ in the nuclear layer l due to the applied driving field, where $\boldsymbol{r}_{ln\parallel}$

is the projection of $\boldsymbol{r}_{ln}$ onto the nuclear plane. Upon operating the thin-film cavity under a well defined angle of incidence, only a single parallel wave vector $\boldsymbol{k}_\parallel$ will be driven. We show that for the present setting this wave vector will be preserved by the dynamics.

Starting from the many-body description (2.15–2.17) the equations of motion for the expectation values $\sigma^-_{ln}(t) \equiv \left\langle \hat{\sigma}^-_{ln} \right\rangle$ in the low-excitation regime read

$$\dot{\sigma}^-_{ln}(t) = -i\left(\omega_{\mathrm{nuc}} - i\frac{\gamma_0}{2}\right)\sigma^-_{ln}(t) + i\sum_{l'n'}\left(J_{ll'nn'} + i\frac{\Gamma_{ll'nn'}}{2}\right)\sigma^-_{l'n'}(t) + i\boldsymbol{d}^*_l \cdot \boldsymbol{E}(\boldsymbol{r}_{ln})\,, \tag{2.19}$$

where we used that the nuclei are very close to their ground state, $\sigma^z_{ln}(t) \approx -1$. Inserting this equation into the definition of the spin-wave operators, Eq. (2.18), and approximating the nuclear layers to be homogeneous, the discrete Fourier transforms introduced by Eq. (2.18) become continuous ones and we can rewrite the equations of motion for the expectation values of the spin-wave operators $\sigma^-_{l,\boldsymbol{k}_\parallel}(t) \equiv \langle \hat{\sigma}^-_{l,\boldsymbol{k}_\parallel} \rangle$ as

$$\dot{\sigma}^-_{l,\boldsymbol{k}_\parallel}(t) = -i(\omega_{\mathrm{nuc}} - i\frac{\gamma_0}{2})\sigma^-_{l,\boldsymbol{k}_\parallel}(t) + i\sum_{l'}\left(\Delta_{ll'} + i\frac{\gamma_{ll'}}{2}\right)\sigma^-_{l',\boldsymbol{k}_\parallel}(t) + i\frac{N}{A}\boldsymbol{d}^*_l \cdot \boldsymbol{E}_{\mathrm{in}}(z_l, \boldsymbol{k}_\parallel)\,, \tag{2.20}$$

where z_l is the position of ensemble l normal to the layer surfaces and the resulting coupling constants are again discussed in the following Sec. 2.2.3. Clearly, only spin-waves with the same parallel wave vector $\boldsymbol{k}_\parallel$ are coupled to one another and thus the dynamics are bound to the subspace spanned by these spin-waves, i.e. the light-matter dynamics in the cavity preserves the parallel wave vector $\boldsymbol{k}_\parallel$ [48]. This is consistent with the expectation that in reflecting light on the cavity, the angles of incidence and reflection coincide for a translationally invariant structure under plane-wave illumination.

When assuming linear response, $\sigma^z_{l,\boldsymbol{k}_\parallel}(t) \approx -1$, the very same equation of motion, Eq. (2.20), can be derived upon calculating the dynamics of $\sigma^-_{l,\boldsymbol{k}_\parallel}(t)$ from the Hamiltonian

$$\hat{H} = \sum_l \frac{\omega_{\mathrm{nuc}}}{2}\hat{\sigma}^z_{l,\boldsymbol{k}_\parallel} - \sum_{ll'}\Delta_{ll'}\hat{\sigma}^+_{l,\boldsymbol{k}_\parallel}\hat{\sigma}^-_{l',\boldsymbol{k}_\parallel} - \sum_l\left(\Omega_l\hat{\sigma}^+_{l,\boldsymbol{k}_\parallel} + \mathrm{h.c.}\right) \tag{2.21}$$

and Lindbladian

$$\mathcal{L}[\rho] = \sum_{ll'}\frac{\gamma_{ll'} + \delta_{ll'}\gamma_0}{2}\left[2\hat{\sigma}^-_{l',\boldsymbol{k}_\parallel}\rho\hat{\sigma}^+_{l,\boldsymbol{k}_\parallel} - \left\{\hat{\sigma}^+_{l,\boldsymbol{k}_\parallel}\hat{\sigma}^-_{l',\boldsymbol{k}_\parallel}, \rho\right\}\right]\,, \tag{2.22}$$

where $\hat{\sigma}^\pm_{l,\boldsymbol{k}_\parallel}$ and $\hat{\sigma}^z_{l,\boldsymbol{k}_\parallel}$ are Pauli operators and $\Omega_l = \boldsymbol{d}^*_l \cdot \boldsymbol{E}_{\mathrm{in}}(z_l, \boldsymbol{k}_\parallel)N/A$ is the effective Rabi-frequency, with the effective in-plane nuclear number density N/A. Since both

descriptions, Eqs. (2.16, 2.17) and Eqs. (2.21, 2.22), yield the same equation of motion, Eq. (2.20), the descriptions are equivalent in the low-excitation regime.

The dimension of the Hilbert space, on which the above Hamiltonian, Eq. (2.21), acts, is significantly reduced as compared to the full many-body description according to Eqs. (2.16) and (2.17). While for the latter case, the dynamics are described by 2^N (with the number of nuclei N) states, the spin-wave basis description uses only 2^L states (with the number of resonant layers L). The number of relevant states in the effective description Eq. (2.21) and (2.22) is reduced even further to $L+1$ relevant states when noticing that only singly excited states, $|\mathrm{E}_{l=1},\mathrm{G}_{l=2},\mathrm{G}_{l=3},...,\mathrm{G}_{l=L}\rangle$, $|\mathrm{G}_{l=1},\mathrm{E}_{l=2},\mathrm{G}_{l=3},...,\mathrm{G}_{l=L}\rangle$, ..., $|\mathrm{G}_{l=1},\mathrm{G}_{l=2},\mathrm{G}_{l=3},...,\mathrm{E}_{l=L}\rangle$ are relevant in the low-excitation regime, where $|\mathrm{E}_l\rangle$ ($|\mathrm{G}_l\rangle$) denotes that the spin-wave in layer l is excited (not excited).

Summarizing, by virtue of the accordance of the equations of motion in the low-excitation regime, we can equally well describe the dynamics of the nuclei in the thin-film cavity by a substantially simplified effective quantum few-level scheme with the equations of motion given by Eqs. (2.21) and (2.22).

2.2.3 Coupling constants

It remains to discuss the coupling constants entering the equations of motion resulting from Eqs. (2.16, 2.17) and (2.21, 2.22) in the many-body and the spin-wave basis, respectively. Within macroscopic QED, these constants can be expressed in terms of the Green's function characterizing the cavity environment [69, 70]. Generally, the electromagnetic Green's function is defined as

$$\boldsymbol{\nabla}\times\boldsymbol{\nabla}\times\boldsymbol{G}(\boldsymbol{r},\boldsymbol{r}',\omega)-\omega^2\varepsilon(\boldsymbol{r},\omega)\boldsymbol{G}(\boldsymbol{r},\boldsymbol{r}',\omega)=\delta(\boldsymbol{r}-\boldsymbol{r}')\,, \tag{2.23}$$

where $\varepsilon(\boldsymbol{r},\omega)$ denotes the dielectric permittivity, $\delta(\cdot)$ is the Dirac delta distribution and $\boldsymbol{\nabla}$ is the nabla operator. Note, that the Green's function is a 3×3 matrix in general.

In the many-body basis, the coupling and (cross-)decay constants evaluate to [48]

$$J_{ll'nn'}=\mu_0\omega_{\mathrm{nuc}}^2\boldsymbol{d}_l^*\cdot\mathrm{Re}\left[\boldsymbol{G}(\boldsymbol{r}_{ln},\boldsymbol{r}_{l'n'},\omega_{\mathrm{nuc}})\right]\cdot\boldsymbol{d}_{l'}\,, \tag{2.24}$$

$$\Gamma_{ll'nn'}=2\mu_0\omega_{\mathrm{nuc}}^2\boldsymbol{d}_l^*\cdot\mathrm{Im}\left[\boldsymbol{G}(\boldsymbol{r}_{ln},\boldsymbol{r}_{l'n'},\omega_{\mathrm{nuc}})\right]\cdot\boldsymbol{d}_{l'}\,, \tag{2.25}$$

where μ_0 is the vacuum permeability and $\boldsymbol{G}(\boldsymbol{r}_{ln},\boldsymbol{r}_{l'n'},\omega_{\mathrm{nuc}})$ the Green's function evaluated at the position of two nuclei $\boldsymbol{r}_{ln},\boldsymbol{r}_{l'n'}$ and the nuclear transition frequency ω_{nuc}.

In the few-level description, the couplings read

$$\Delta_{ll'}=\frac{N}{A}\mu_0\omega_{\mathrm{nuc}}^2\boldsymbol{d}_l^*\cdot\mathrm{Re}\left[\boldsymbol{G}(z_l,z_{l'},\boldsymbol{k}_\parallel,\omega_{\mathrm{nuc}})\right]\cdot\boldsymbol{d}_{l'}\,, \tag{2.26}$$

$$\gamma_{ll'}=2\frac{N}{A}\mu_0\omega_{\mathrm{nuc}}^2\boldsymbol{d}_l^*\cdot\mathrm{Im}\left[\boldsymbol{G}(z_l,z_{l'},\boldsymbol{k}_\parallel,\omega_{\mathrm{nuc}})\right]\cdot\boldsymbol{d}_{l'}\,, \tag{2.27}$$

where $\boldsymbol{G}(z, z', \boldsymbol{k}_\parallel, \omega_{\mathrm{nuc}})$ is the in-plane Fourier transformed electromagnetic Green's function, related to the position-space Green's function via

$$\boldsymbol{G}(\boldsymbol{r}, \boldsymbol{r}', \omega) = \int \frac{\mathrm{d}^2\boldsymbol{k}_\parallel}{(2\pi)^2}\, \boldsymbol{G}(z, z', \boldsymbol{k}_\parallel, \omega)\, e^{i\boldsymbol{k}_\parallel \cdot (\boldsymbol{r}_\parallel - \boldsymbol{r}'_\parallel)}\,. \tag{2.28}$$

Note that in the following mainly the in-plane Fourier transformed Green's function will be of importance such that we will simply refer to it as the Green's function. For the present case of a layered dielectric medium, analytic expressions for the Green's function are derived in [58] and summarized in Appendix A.1.

Finally, we discuss the driving field $\boldsymbol{E}_{\mathrm{in}}(\boldsymbol{k}_\parallel, z)$ appearing in Eq. (2.21). It relates to its real-space representation by the in-plane Fourier transform,

$$\boldsymbol{E}_{\mathrm{in}}(\boldsymbol{r}) = \int \frac{\mathrm{d}^2\boldsymbol{k}_\parallel}{(2\pi)^2}\, \boldsymbol{E}_{\mathrm{in}}(z, \boldsymbol{k}_\parallel)\, e^{i\boldsymbol{k}_\parallel \cdot \boldsymbol{r}_\parallel}\,. \tag{2.29}$$

Inside the cavity, the externally applied field is modified due to absorption and reflection by the cavity materials. Quantitatively, its frequency space solution can be obtained, e.g., by Parratt's formalism [64] similarly to the calculations exemplified in Sec. 2.1. Note that this field is to be calculated without considering the nuclear resonance, but including the electronic index of refraction of the nuclear layer.

2.2.4 Reflection spectrum

The key observable for nuclei embedded in thin-film cavities, dominating the experimental work up to now, is the linear spectrum of the reflected light measured for a fixed angle of incidence of the probing x-rays. Following [48], we summarize the relevant aspects of this observable in the present context.

Fourier transforming $\sigma^-_{l,\boldsymbol{k}_\parallel}(t) = \int \mathrm{d}\omega\, e^{-i\omega t}\sigma^-_{l,\boldsymbol{k}_\parallel}(\omega)$, Eq. (2.20) is readily solved in frequency space. The collective dynamics of the nuclei modify the overall electric field $\boldsymbol{E}(0, \boldsymbol{k}_\parallel, \omega)$ at the surface which can be calculated by the generalized input-output relation [69]

$$\boldsymbol{E}(0, \boldsymbol{k}_\parallel, \omega) = \boldsymbol{E}_{\mathrm{in}}(0, \boldsymbol{k}_\parallel, \omega_{\mathrm{nuc}}) + \mu_0\omega^2_{\mathrm{nuc}} \sum_l \boldsymbol{G}(0, z_l, \boldsymbol{k}_\parallel, \omega_{\mathrm{nuc}}) \cdot \boldsymbol{d}_l\, \sigma^-_{l,\boldsymbol{k}_\parallel}(\omega)\,. \tag{2.30}$$

Note that in Eq. (2.30) we used the fact that the incoming electric field and the Green's function can be approximated as constant in frequency on scales of the nuclear linewidth.

Finally, for the incoming field strength normalized to one, the overall reflection coefficient is given by subtracting the incident field strength from the overall electric field,

$$r(\boldsymbol{k}_\parallel, \omega) = \boldsymbol{E}(0, \boldsymbol{k}_\parallel, \omega) - 1 = \boldsymbol{r}_{\mathrm{el}} + \mu_0\omega^2_{\mathrm{nuc}} \sum_l \boldsymbol{G}(0, z_l, \boldsymbol{k}_\parallel, \omega_{\mathrm{nuc}}) \cdot \boldsymbol{d}_l\, \sigma^-_{l,\boldsymbol{k}_\parallel}(\omega)\,, \tag{2.31}$$

where we used the electronic cavity reflectivity (including polarization),

$$\boldsymbol{r}_{\mathrm{el}} = \boldsymbol{E}_{\mathrm{in}}(0, \boldsymbol{k}_{\parallel}, \omega_{\mathrm{nuc}}) - 1\,, \tag{2.32}$$

given by the (cavity modified) electric field at the cavity surface without the incoming field strength. Noting that the Fresnel coefficients for s- and p-polarization become equivalent at grazing incidence [65], and that the electronic scattering and the scattering on the single unsplit nuclear resonance leave the polarization of the incident x-rays unchanged, we subsequently focus on the treatment of s-polarized light and omit the vectorial nature of the electric field and Green's function throughout the remaining parts of the thesis.

3 Artificial two-level schemes from Mössbauer nuclei

In this chapter, the artificial two-level scheme on the basis of Mössbauer nuclei in thin-film cavities is introduced and its fundamental properties are analyzed. We start out by adapting the general few-level description to the simplest case of a single resonant layer, thus yielding the two-level scheme. We consider the properties of the reflection spectrum and define a criterion of experimental visibility on that basis. Subsequently, we examine a simple thin-film cavity, where the single resonant ^{57}Fe layer is embedded in ordinary ^{56}Fe. Therefore, the electronic refractive index is constant in the layer stack and the theoretical description rather straightforward. This allows the analysis of the Green's function on an analytical level and illustrates fundamental characteristics for the systems.

3.1 Single resonant layer – two-level scheme

For a single resonant layer in the thin-film cavity, only a single spin-wave can be excited and the corresponding effective description of Eqs. (2.21) and (2.22) simplifies to

$$\hat{H} = \frac{\omega_{\mathrm{nuc}}}{2}\hat{\sigma}^{z}_{\boldsymbol{k}_\parallel} + \Delta_{\mathrm{CLS}}\hat{\sigma}^{+}_{\boldsymbol{k}_\parallel}\hat{\sigma}^{-}_{\boldsymbol{k}_\parallel} - \left(\Omega\hat{\sigma}^{+}_{\boldsymbol{k}_\parallel} + \mathrm{h.c.}\right) \tag{3.1}$$

and

$$\mathcal{L}[\rho] = \frac{\Gamma_{\mathrm{SR}} + \gamma_0}{2}\left[2\hat{\sigma}^{-}_{\boldsymbol{k}_\parallel}\rho\hat{\sigma}^{+}_{\boldsymbol{k}_\parallel} - \left\{\hat{\sigma}^{+}_{\boldsymbol{k}_\parallel}\hat{\sigma}^{-}_{\boldsymbol{k}_\parallel},\rho\right\}\right], \tag{3.2}$$

where we have omitted the nuclear layer index and used the decay enhancement Γ_{SR} and frequency shift Δ_{CLS} as defined below. Further, the effective Rabi-frequency is $\Omega = d^{*}E_{\mathrm{in}}(z, \boldsymbol{k}_\parallel)N/A$ with the position z of the resonant layer normal to the layer surfaces.

The Eqs. (3.1, 3.2) indeed have the form of a quantum mechanical two-level system. However, the excited state is now a collective spin-wave excitation in the ensemble of nuclei embedded in the cavity, rather than one of the single-nucleus excitations considered in the many-body Eqs. (2.16, 2.17). Furthermore, the properties of the effective two-level system are different compared to the bare nuclei. First, an additional detuning term Δ_{CLS} appears, which shifts the transition energy of the two-level system, and which is known as the *Collective Lamb Shift* [50, 71–78]. Second,

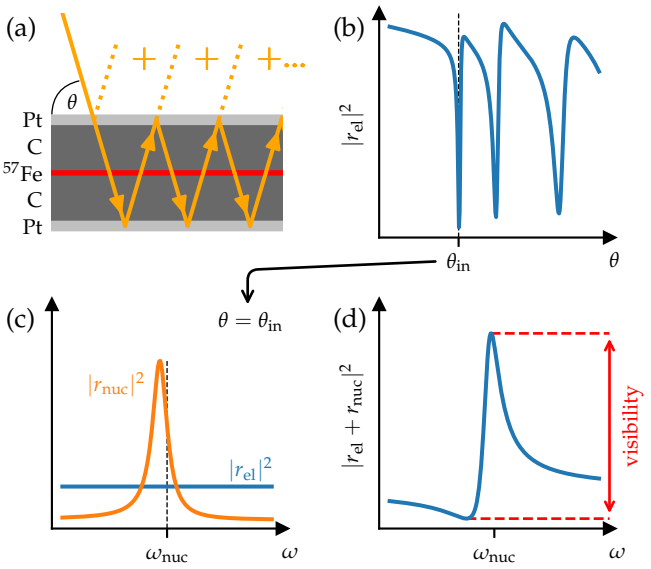

Fig. 3.1: Cavity observables and visibility of the nuclear response in the reflection spectrum. (a) Schematic representation of the leading interfering contributions to the electronic cavity reflectance. For the actual calculation, reflections at the remaining layers, e.g. the ^{57}Fe layer, have to be taken into account as well. (b) Electronically reflected intensity ("rocking curve") as calculated by the contributions in (a) using Parratt's formalism [64]. (c) Electronic r_{el} and nuclear r_{nuc} contributions to the reflectance as function of the frequency ω for a fixed angle of incidence $\theta = \theta_{\mathrm{in}}$. (d) Full reflection spectrum given by the sum of both (complex-valued) contributions. The peak-to-peak amplitude of the resulting Fano-resonance is taken as the visibility criterion.

the radiative decay rate is enhanced by the additional superradiant [47, 75, 79–81] contribution Γ_{SR} as compared to the single-particle decay. Third, the light-matter coupling depends on the effective in-plane nuclear number density N/A, which appears as a result of the two-dimensional in-plane Fourier transformation. The explicit expressions for the frequency shift Δ_{CLS} and the enhancement of the spontaneous decay rate Γ_{SR} can be written as

$$\Delta_{\mathrm{CLS}} = -\frac{N}{A}\mu_0\omega_{\mathrm{nuc}}^2|d|^2\,\mathrm{Re}\left[G(z,z,\boldsymbol{k}_\parallel,\omega_{\mathrm{nuc}})\right]\,, \tag{3.3}$$

$$\Gamma_{\mathrm{SR}} = 2\frac{N}{A}\mu_0\omega_{\mathrm{nuc}}^2|d|^2\,\mathrm{Im}\left[G(z,z,\boldsymbol{k}_\parallel,\omega_{\mathrm{nuc}})\right]\,, \tag{3.4}$$

where both remaining spatial arguments of the Green's function are evaluated at the nuclear layer depth z. Explicit expressions for the Green's function and the field configuration determining the Rabi frequency Ω for the single resonant layer are provided in Appendix A.1. Importantly, they can be tuned via the cavity structure and the angle of incidence of the x-rays. For this reason, we refer to the effective description as a tunable artificial two-level system.

3.1.1 Reflection spectrum

The reflection spectrum comprises contributions by the purely electronic reflection at the different layer boundaries and by the artificial nuclear two-level system. We illustrate these in Fig. 3.1. We calculate the purely electronic reflection r_{el} using Parrat's formalism [64], which sums all the different scattering contributions arising

from the material boundaries (see Sec. 2.1). Although the electronically reflected light is in principle frequency dependent, the dependency can be neglected on scales of the linewidth of the nuclei.

The dynamics of the artificial two-level system from Eq. (2.20) can be solved for in frequency space,

$$\sigma^{-}_{\boldsymbol{k}_\parallel}(\omega) = -\frac{d^* E_{\mathrm{in}}(z, \boldsymbol{k}_\parallel, \omega_{\mathrm{nuc}}) N/A}{\omega - \omega_{\mathrm{nuc}} - \Delta_{\mathrm{CLS}} + i(\gamma_0 + \Gamma_{\mathrm{SR}})/2}\,, \tag{3.5}$$

giving rise to a Lorentzian spectrum in linear response. According to Eq. (2.31), the nuclear response acquires an additional complex-valued weight upon propagation to the cavity surface, and interferes with the complex-valued electronically reflected background, see Fig. 3.1.

Inserting Eq. (3.5) into Eq. (2.31), in turn, yields the overall reflected intensity normalized to the incoming intensity,

$$|r(\omega)|^2 = \left| |r_{\mathrm{el}}| + \frac{|C| e^{i\varphi}}{\Delta + i\Gamma} \right|^2 , \tag{3.6}$$

where the parameters Eqs. (3.7 - 3.10) can be read off.

Depending on the relative phase φ of both contributions, different nuclear Fano lineshapes arise in the spectra [82–85]. The response is centered at the transition frequency $\omega_{\mathrm{nuc}} + \Delta_{\mathrm{CLS}}$ of the collective two-level system and superradiantly broadened by Γ_{SR}, such that

$$\Delta = \omega - (\omega_{\mathrm{nuc}} + \Delta_{\mathrm{CLS}})\,, \tag{3.7}$$

$$\Gamma = (\gamma_0 + \Gamma_{\mathrm{SR}})/2\,. \tag{3.8}$$

The relative weight of the nuclear contribution C, resulting from the coupling of the nuclei to the driving field as well as the propagation of the nuclear response to the cavity surface, can be expressed as

$$C = -\frac{N}{A} \mu_0 \omega_{\mathrm{nuc}}^2 |d|^2 G(0, z, \boldsymbol{k}_\parallel, \omega_{\mathrm{nuc}}) E_{\mathrm{in}}(z, \boldsymbol{k}_\parallel, \omega_{\mathrm{nuc}})\,, \tag{3.9}$$

again using the Green's function. Finally, the relative phase between these two contributions determining the line shape of the nuclear resonance is [82–84]

$$\varphi = \arg(C) - \arg(r_{\mathrm{el}})\,. \tag{3.10}$$

Explicit expressions for the Green's function, the electric field configuration and the electronic cavity reflection in the archetype system of Fig. 1.1 are provided in Appendix A.1.1.

3.1.2 Visibility of the nuclear response

From Eqs. (3.6) and (3.9) it is clear that the nuclear signatures in the reflection spectrum can be strongly suppressed, e.g., by the Green's function contribution. One obvious reason for strong attenuation are thick or highly absorptive cavity layers. This poses the problem that some two-level systems might be not observable via the reflection spectrum. In such situations, the formally best cavity structures may not be the most relevant ones for experimental purposes. This challenge can be tackled by including conditions on the practical relevance, such as the observability, into the design rules.

Considering the lineshape of a Fano-resonance, a suitable criterion for the visibility of the nuclear signature is the peak-to-peak amplitude of the resonance in the normalized reflection spectrum, see. Fig. 3.1(d). In the optimization, one may then set a minimum visibility as a boundary condition, or optimize the visibility for an otherwise specified design goal.

An efficient calculation of the visibility criterion is possible via analytical expressions for the positions of the two extrema of Eq. (3.6) in terms of Δ,

$$\Delta_{\pm} = -\frac{1}{2|r_{\mathrm{el}}|}\Big[|C|\sec(\varphi) + 2|r_{\mathrm{el}}|\Gamma\tan(\varphi) \pm \sec(\varphi)\sqrt{|C|^2 + 4|r_{\mathrm{el}}|^2\Gamma^2 + 4|C||r_{\mathrm{el}}|\Gamma\sin(\varphi)}\Big]. \tag{3.11}$$

The visibility is then defined to be

$$\left|\left||r_{\mathrm{el}}| + \frac{|C|e^{i\varphi}}{\Delta_+ + i\Gamma}\right|^2 - \left||r_{\mathrm{el}}| + \frac{|C|e^{i\varphi}}{\Delta_- + i\Gamma}\right|^2\right|. \tag{3.12}$$

In part of the calculations in Chapter 4, we will use this visibility criterion as a design goal.

3.2 Two-level schemes from ^{56}Fe/^{57}Fe/^{56}Fe systems – analytical treatment

According to Eqs. (3.3) and (3.4), the CLS and SR are proportional to the Green's function, Δ_{CLS}, $\Gamma_{\mathrm{SR}} \propto G(z, z, \boldsymbol{k}_{\parallel}, \omega_{\mathrm{nuc}})$. A simple setting where we can acquaint ourselves with the Green's function and its relation to the mode structure is a ^{56}Fe/^{57}Fe/^{56}Fe layer stack, as is shown in Fig. 3.2. Since the Green's function description is only concerned with the off-resonant field, and the electronic refractive indices of the iron isotopes are the same, the electromagnetic environment corresponds to a single layer, similarly to the ones considered in Sec. 2.1. Hence, the cavity features a comparatively simple description. It should, however, be noted that iron

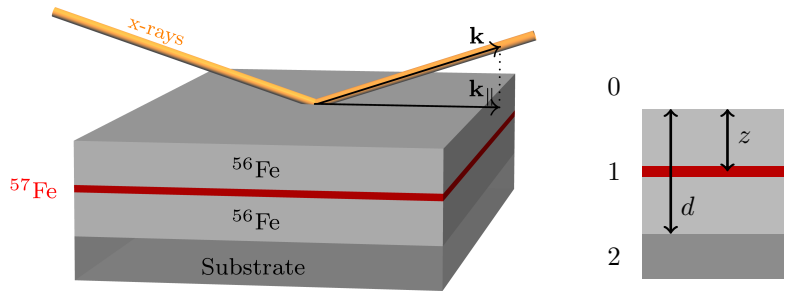

Fig. 3.2: Schematic representation of the ^{56}Fe/^{57}Fe/^{56}Fe cavity setup. The ^{57}Fe layer is chosen ultrathin such that evaluation of the Green's function in its center is justified. Different substrate materials are used in the main text. The enumeration of the layers as well as relevant parameters are indicated on the right hand side.

as a guiding layer is not the most favorable cavity material and the setup thus rather serves as a testbed for the theory that will be applied to realistic settings in the following chapters. For the explicit formulae we will further neglect the absorption in the iron layers for simplicity, while, however, comparing to the absorptive system throughout the analysis.

The Green's function for a single layer cavity, evaluated at the same coordinates $z = z'$, is given by (see Appendix A.1.1 and [58])

$$G(z, z, \boldsymbol{k}_\parallel, \omega_{\mathrm{nuc}}) = \frac{2\pi i}{\beta_1} \frac{\left(1 + r_{12} e^{2i\beta_1(d-z)}\right)\left(1 - r_{01} e^{2i\beta_1 z}\right)}{1 + r_{01} r_{12} e^{2i\beta_1 d}}, \tag{3.13}$$

where the layer indices and coordinate conventions are according to Fig. 3.2 or previous sections. We want to consider two special cases of simple iron layers that we already encountered in Sec. 2.1: Firstly, we assume the iron to be deposited on a perfect mirror as was considered in Sec. 2.1.1. Secondly, we will look at a symmetric system, having vacuum at both sides of the iron layer, see Sec. 2.1.2.

3.2.1 Vacuum/^{56}Fe/^{57}Fe/^{56}Fe/mirror-system

Specializing the general expression Eq. (3.13) to the mirror substrate, we have to set $r_{12} = -1$ and hence arrive at

$$G(z, z, \boldsymbol{k}_\parallel, \omega_{\mathrm{nuc}}) = \frac{2\pi i}{\beta_1} \frac{\left(1 - e^{2i\beta_1(d-z)}\right)\left(1 - r_{01} e^{2i\beta_1 z}\right)}{1 - r_{01} e^{2i\beta_1 d}}\,. \tag{3.14}$$

Comparing the denominator of this equation to the one of the corresponding reflection coefficient, Eq. (2.4), we see that both expressions have the same poles, i.e. they share their mode structure.

For incident angles below the angle of total external reflection, light can only enter the layer evanescently, which is why we restrict the analysis to angles above this critical angle. Approximating the iron layers to be without absorption, we find the

Fresnel coefficient $r_{01}, \beta_1 \in \mathbb{R}$. Separating real and imaginary part, we rephrase the Green's function as

$$\begin{aligned} G =& \frac{2\pi}{\beta} \frac{1}{1 - 2r\cos(2\beta d) + r^2} \\ & \times \Big\{ \Big[(1 + r^2) \sin(2\beta(d - z)) - 4r \cos(\beta(z + d)) \sin(\beta(d - z)) \Big] \\ & + i(1 - r^2) \left[1 - \cos(2\beta(d - z)) \right] \Big\} \,, \end{aligned} \tag{3.15}$$

where we renamed $\beta \equiv \beta_1$, $r \equiv r_{01}$ and omitted the Green's function's arguments for simplicity. To access the properties of the Green's function we start out considering the imaginary part that determines the decay enhancement.

Superradiance – imaginary part

A relevant question is where the SR can be expected to be maximal or minimal. The critical points of the imaginary part as a function of z are determined by

$$\frac{\mathrm{d}\,\mathrm{Im}(G)}{\mathrm{d}z} = 0 \Leftrightarrow (r^2 - 1) \sin(2\beta(d - z)) = 0 \,, \tag{3.16}$$

with the respective solutions,

$$z_m = d - \frac{m\pi}{2\beta} \,, \tag{3.17}$$

for $m \in \mathbb{N}$ in the appropriate range. Being on one of the curves z_m is a necessary condition for an extremum. We can hence eliminate z in the Green's function,

$$\mathrm{Im}(G(z_m(d), d)) = \begin{cases} 0 \,, & m \text{ even}, \\ \dfrac{4\pi}{\beta} \dfrac{1 - r^2}{(1 + r^2) - 4r\cos^2(\beta d)} \,, & m \text{ odd}. \end{cases} \tag{3.18}$$

We find vanishing imaginary part for even integers on the whole curve and a single result for all odd integers. Specializing to odd integers, we can now determine the extrema of the imaginary part in terms of d to be

$$d_l = \frac{l\pi}{\beta}. \tag{3.19}$$

For a fixed incident angle, Fig. 3.3 shows the SR in the (z, d) parameter space for the non-absorptive approximation as well as the full absorbing system. Here, the critical points in z are shown and the local extrema in the (z, d) plane are clearly visible. Although the maxima are reduced in height and less distinguished when absorption is taken into account in Fig. 3.3(a), all structures from the approximated system, Fig. 3.3(b), can be recognized. Thus, we can still retrieve qualitative insights from the approximated formulae.

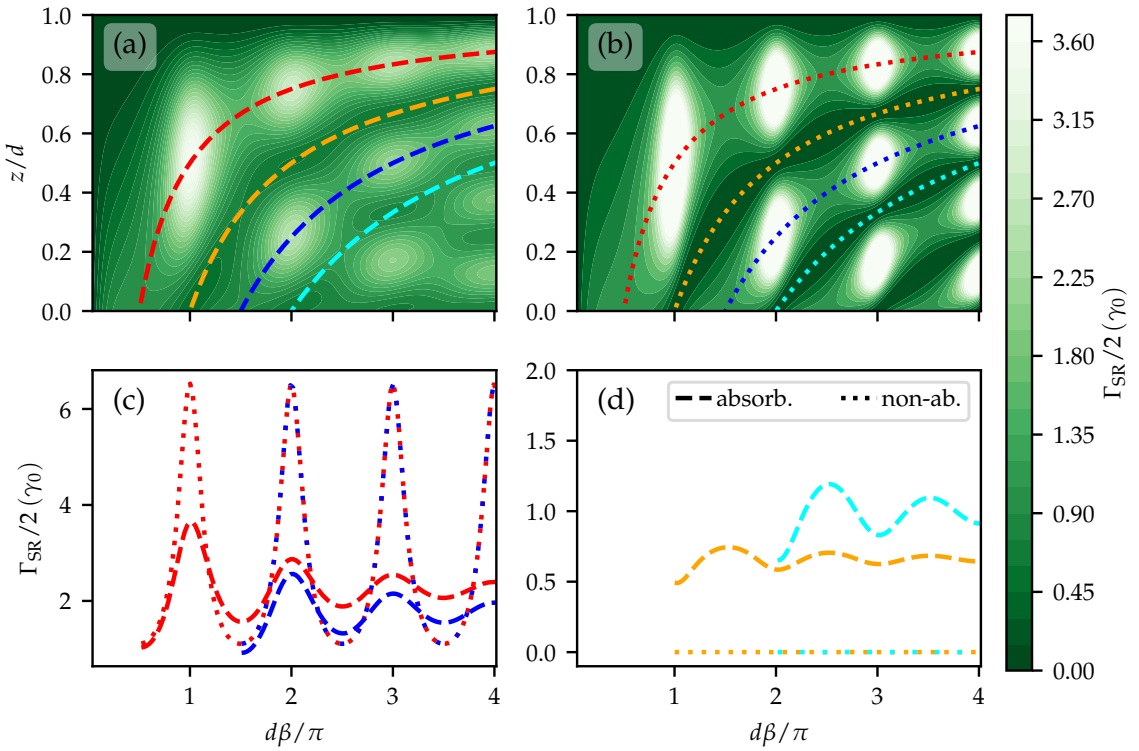

Fig. 3.3: Γ_{SR} for the vacuum/^{56}Fe/^{57}Fe(0.57 nm)/^{56}Fe/mirror-system in terms of non-dimensionalized thickness $d\beta/\pi$ and relative ^{57}Fe position z/d at fixed incident angle of $\theta = 4.2$ mrad. Panel (a) shows the SR taking into account absorption whereas absorption is neglected in panel (b). The colored lines in (a) and (b) correspond to the critical points in z in the non-absorptive case for different m according to Eq. (3.17) and are the same for both panels. Panel (c) shows Γ_{SR} corresponding to the maximal and (d) for the minimal $z_m(d)$ curves, each for the absorptive (dashed) as well as the non-absorptive (dotted) case. The respective colors link the graphs in (a, b) to the ones in (c, d).

To that end, one can define an effective wavelength normal to the layer surfaces, $\lambda_n = 2\pi/\beta$ (where we take β real as from the non-absorbing system). Of course, this wavelength is larger than the physical wavelength in the iron layer, hence allowing for resonances with nano-meter scale layer thicknesses. The thickness d of the iron slab is non-dimensionalized by dividing by half of this effective wavelength in Fig. 3.3. The local maxima in the SR thus occur whenever the thickness is a multiple of $\lambda_n/2$. This fits with the expectation that the photonic density of states, accessible for the spontaneous emission [86], is largest in the anti-nodes of eigenmodes of the system. The in-plane Fourier transformed Green's function (3.13) is analytically equivalent to the real space Green's function of a one-dimensional resonator in combination with the effective wavelength λ_n and suitable reflection coefficients [87]. Although the nuclei are in principle coupled by the cavity and only therefore become an artificial quantum system, this suggests that an instructive viewpoint is to also consider the

nuclei as a collective quantum system placed inside a one-dimensional cavity. In Sec. 4.3.2, we will, however, compare the properties of a genuine two-level system inside a lossy one-dimensional cavity and also find differences to the x-ray thin-film setting that are based on the different behavior of the reflection coefficients.

Fig. 3.3(c) and (d) show the evaluation of the SR on the maximal and minimal curves $z_m(d)$, respectively, where dotted lines correspond to the non-absorptive and dashed lines describe the SR for absorbing system. For the absorbing system one can see that with increasing thickness d, i.e. with increasing length of the path in the absorbing medium, the local maxima loose in height whereas they stay constant for the non-absorptive approximation. For realistic systems, the first mode therefore is of special significance for large SR.

In a last step we can now evaluate the imaginary part for the non-absorptive approximation for d_l and arrive at

$$\mathrm{Im}\left[G(\theta)\right] = \frac{4\pi}{\beta_1}\frac{1+r_{01}}{1-r_{01}} = 4\pi\frac{\beta_0}{\beta_1^2} = \frac{4\pi}{k_0}\frac{\sin\theta}{n_{\mathrm{Fe}}^2-\cos^2\theta} = \frac{4\pi}{k_0}\frac{\sin\theta}{\cos^2\theta_{\mathrm{c}}-\cos^2\theta}, \tag{3.20}$$

where $\theta_{\mathrm{c}} = \arccos(\mathrm{Re}[n_{\mathrm{Fe}}])$ denotes the angle of total reflection and, for clarity, we added the indices to β_1 and r_{01}. For the non-absorbing system, all maxima have the same value and diverge for the angle approaching total reflection. Clearly, this is where the absorption plays a crucial part as the transition from total to normal reflection is smoothed out.

Collective Lamb shift – real part

For the frequency shift of the two-level system we can in principle proceed as we did for the SR. The critical points in terms of z for the real part are given by

$$\frac{\mathrm{d}\,\mathrm{Re}(G)}{\mathrm{d}z} = 0 \Leftrightarrow (1+r^2)\cos(2\beta(d-z)) - 4r\cos(2\beta z) = 0. \tag{3.21}$$

The solution of this equation, however, turns out to be not as simple as it was for the case of the SR. Therefore, we will not consider the CLS at this point, but perform the respective analysis in the context of the subsequent part where the substrate mirror layer is replaced by vacuum.

3.2.2 Vacuum/^{56}Fe/^{57}Fe/^{56}Fe/vacuum-system

Specializing the bottom layer to vacuum we have to set $r_{12} = -r_{01}$ and hence arrive at

$$G(z,z,\boldsymbol{k}_{\parallel},\omega) = \frac{2\pi i}{\beta_1}\frac{\left(1-r_{01}e^{2i\beta_1(d-z)}\right)\left(1-r_{01}e^{2i\beta_1 z}\right)}{1-(r_{01})^2e^{2i\beta_1 d}}\,. \tag{3.22}$$

Again, the mode structure of the Green's function function agrees with the one of the respective reflection coefficient, Eq. (2.12). We proceed as before and separate

real and imaginary part of the Green's function in the non-absorptive case for angles above the critical one,

$$\begin{aligned} G =& \frac{2\pi}{\beta} \frac{1}{1-2r^2\cos(2\beta d)+r^4} \\ & \times \Big\{ 2r\left[(1+r^2)\sin(\beta d)\cos(\beta(d-2z)) - r\sin(2\beta d)\right] \\ & \quad + i(1-r^2)\left[1+r^2-2r\cos(\beta d)\cos(\beta(d-2z))\right] \Big\}, \end{aligned} \tag{3.23}$$

again having simplified the notation of r and β.

Superradiance – imaginary part

For the discussion we start out with the analysis of extrema of the imaginary part, i.e. of the SR. The critical points as a function of z are determined by

$$\frac{\mathrm{d}\,\mathrm{Im}(G)}{\mathrm{d}z} = 0 \Leftrightarrow r\left(r^2-1\right)\cos(\beta d)\sin(\beta(d-2z)) = 0, \tag{3.24}$$

with the solutions

$$z_m = \frac{d}{2} + \frac{\pi m}{2\beta}. \tag{3.25}$$

Evaluating the imaginary part on these extremal curves, we arrive at

$$\mathrm{Im}\left[G(z_m(d),d)\right] = \frac{2\pi(1-r^2)}{\beta}\,\frac{1+r^2-2r\cos(\beta d)(-1)^m}{(1+r^2)^2-4r^2\cos^2(\beta d)}. \tag{3.26}$$

For odd (even) m we get maxima (minima) for $\beta d = 2m\pi$ and minima (maxima) for $\beta d = (2m+1)\pi$.

For an exemplary angle, we again show the SR as a function of d and z in Fig. 3.4. As before, the overall structure found in the non-absorbing approximation is preserved in the absorbing one. Additionally, the SR also reflects the symmetry of the cavity around $z = d/2$. Unlike for the system with mirror substrate, the SR does not reach zero for the present system.

From Eq. (3.24) we see that besides the critical points there are parameters $\beta d = (2m+1)\pi/2$ where the derivative vanishes irrespective of the value of z, i.e. throughout the layer the SR is constant for the non-absorptive medium. Fig. 3.4(d) relates this behavior to the absorptive system. One can see that for the lowest m, i.e. a thin sample, the feature of constant SR is well reproduced whereas for higher ones the effect is lost as the influence of absorption dominates.

Finally, we evaluate the imaginary part at the maxima for the non-absorbing approximation,

$$\mathrm{Im}(G) = \frac{2\pi}{\beta_1}\frac{1+r_{01}}{1-r_{01}} = \frac{2\pi}{k_0}\frac{\sin\theta}{\cos^2\theta_\mathrm{c}-\cos^2\theta}, \tag{3.27}$$

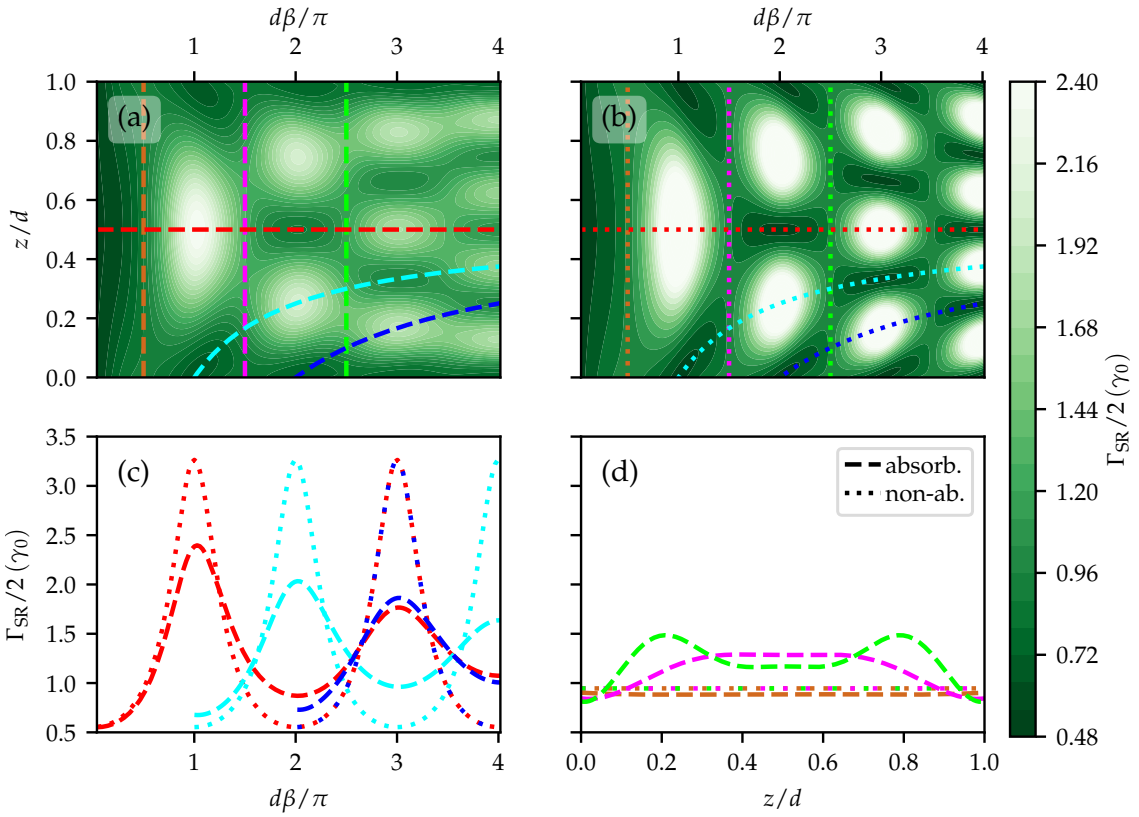

Fig. 3.4: Γ_{SR} for the vacuum/^{56}Fe/^{57}Fe(0.57 nm)/^{56}Fe/vacuum-system in terms of non-dimensionalized thickness $d\beta/\pi$ and relative ^{57}Fe position z/d at fixed incident angle of $\theta = 4.2$ mrad. Panel (a) shows the SR taking into account absorption whereas absorption is neglected in panel (b). The horizontal and bent colored plots in (a) and (b) correspond to the critical points in z in the non-absorptive case for different m according to Eq. (3.25) and are the same for both panels. Panel (c) shows Γ_{SR} corresponding to these curves. Vertical curves in (a) and (b) indicate constant Γ_{SR} for the non-absorptive case. The respective evaluations of Γ_{SR} in the absorptive and non-absorptive systems is given in panel (d) as a function of z/d. The colors link the graphs in (a), (b), (c) and (d) and dashed lines correspond to the absorptive description whereas dotted lines indicate the non-absorptive approximation.

again using the full notation. Analogously to the previous section, all maxima have the same height and diverge for the angle approaching the critical one. As compared to the maximal height in Eq. (3.27), the value is reduced by a factor of two for the system with vacuum on both sides. This can be understood upon noting that for the latter system the transmission provides an additional loss channel out of the cavity, telling us that a good substrate reflectivity is of significance for high SR.

Collective Lamb shift – real part

We now analyze the properties of the real part of the Green's function. The critical points in z are determined by the equation

$$\left[r_{01} + (r_{01})^3\right] \sin(\beta d) \sin(\beta(d - 2z)) = 0, \tag{3.28}$$

where the solutions as a function of z are the same as for the imaginary part. The factor $\sin(\beta d)$ enforces constant CLS irrespective of the position of the nuclei if the product βd is chosen suitably. This means that the CLS has the same extrema as the SR in terms of z, however, while the SR is constant for $\beta d = m\pi + \pi/2$, the CLS is constant for $\beta d = m\pi$. Finding the maxima on the curves of critical points in z as done for the SR is in principle possible, however, cumbersome. Since quantitative results for the CLS in the non-absorbing approximation are of little relevance, we omit the explicit calculation at this point.

Unlike the SR the CLS can have zeros which for the non-absorptive system are given by

$$z_m^{(0)} = \frac{d}{2} \pm \frac{1}{2\beta} \arccos\left(\frac{4r^2}{1+r^2} \cos(\beta d)\right) + \frac{\pi m}{\beta}, \tag{3.29}$$

in simplified notation for β and r. Furthermore one finds zeros at $\beta d = \pi m$ irrespective of z where we previously saw that the CLS is constant.

Analogously to the previous discussions, in Fig. 3.5, we finally show the CLS in the (z, d) plane for a fixed, exemplary angle. As before, we find a close correspondence between the non-absorptive approximation and the full description that becomes less pronounced for higher order modes. Unlike the SR, the CLS can take positive as well as negative values. A characteristic feature, that can already be seen in the comparison of Fig. 3.4(c) and 3.5(c) is the intertwined occurrence of maxima in the SR with zeros in the CLS. We will link this to the pole structure of the Green's function in a slightly different context in Chapter 4.

This brief discussion shall suffice to give us a first qualitative impression of the dependencies of the frequency shift and decay enhancement on different parameters. In particular, we saw the correspondence of thin-film cavity settings with standing waves in simple one-dimensional resonators.

Next, we want to turn to the description, and design, of archetype thin-film cavity systems. For a quantitative description of these, we only occasionally can resort to analytical methods but mostly employ numerical means in the following.

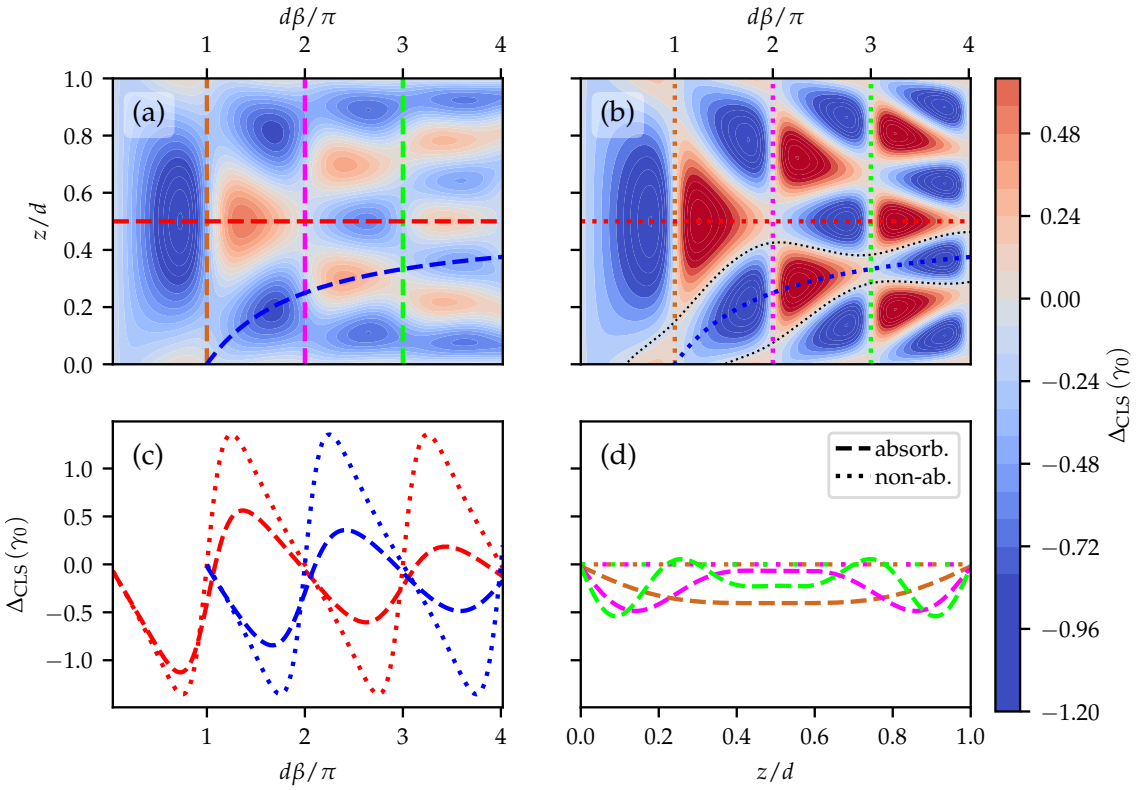

Fig. 3.5: Δ_{CLS} for the vacuum/^{56}Fe/^{57}Fe(0.57 nm)/^{56}Fe/vacuum-system in terms of non-dimensionalized thickness $d\beta/\pi$ and relative ^{57}Fe position z/d at fixed incident angle of $\theta = 4.2$ mrad. The panels are analogous to Fig. 3.4. Panel (b) additionally includes zeros of the CLS in the non-absorptive case according to Eq. (3.29) as black dotted lines which are, however, not shown in (a) and (c) for readability.

4 Inverse design of two-level schemes

In this chapter, we introduce the inverse design of artificial two-level systems from Mössbauer nuclei in thin-film cavities.

For the discussion, we employ the archetype Pt/C/^{57}Fe/C/Pt/Si cavity of Fig. 1.1, similar to cavities commonly used in experiments. The resonant layer is chosen to be about two atomic layers of ^{57}Fe which corresponds to a layer thickness of 0.574 nm, as has been utilized in [50]. At such low layer thicknesses, long-range magnetic order and magnetic hyperfine splittings are suppressed, such that the iron nuclei can indeed be approximated as unsplit two-level systems. The other layer thicknesses as well as the angle of incidence remain as tuning parameters.

A successful implementation of the inverse design requires that one can specify the cavity geometry that realizes a desired level scheme. Naturally, not all imaginable level schemes will be realizable, such that a major objective of the subsequent analysis is to find the accessible parameters of the two-level scheme resulting from the archetype setup described above. Of course, for cavity geometries beyond the one under study, different parameters may be accessible. Partly, we will tackle this fact by considering different materials and resonant isotopes. In general, however, the methods developed and insights acquired hereafter readily generalize to systems beyond the archetype one such that focusing on the experimentally relevant archetype setup is no in-principle restriction. This will become evident in the treatment of more complex systems in Sec. 5.

We will start the analysis by exploring the combinations of CLS and SR that are accessible in the archetype cavity and subsequently add further relevant properties of the level scheme. The CLS and SR are determined by Eq. (3.3) and (3.4) where the Green's function is known analytically, see Appendix A.1.1. The task is thus to explore how far the Green's function can be tuned as a function of the layer thicknesses d_1, d_2, d_4, d_5 and the angle of incidence θ (see Fig. 1.1 for the declaration of the parameters). This task is solved when the surface of the space spanned by CLS and SR as a function of the above parameters is known. In the course of the implementation of the inverse design, a versatile method was developed to determine this surface numerically. The method essentially relies on the construction of suitable scalar cost functions from linear and nonlinear combinations of two-level scheme properties such as the CLS and SR. Maximizing the scalar cost function is then equivalent to determining surface points. To keep this chapter's focus on the physical results, however, the in-detail explanation of the numerical approach has been moved to the self-contained Chapter 6, where we illustrate the basic concept of the method

with an example and give a comprehensive overview of the workflow of our numerical computations.

In the course of the present chapter, various properties of the two-level scheme will be considered. To keep the naming of different quantities concise, from now on the set of all possible values of a given combination of properties of the level scheme will be denoted as the *observables space* (OS) and we frequently refer to the properties themselves as *observables*. The OS could for example be spanned by the accessible combinations of CLS and SR. As opposed to that, we will denote the set of variables over which we perform optimizations as the *cavity parameter space*. For the present case, this would be the space of all sensible values for d_1, d_2, d_4, d_5 and for the angle of incidence θ. Note that throughout the analysis, we will consider different OSs, depending on the respective desired design goals.

4.1 Frequency shift and decay enhancement

As a start, we consider the frequency shift and decay enhancement of the two-level scheme as the design goals. Results for the OS of CLS and SR in the archetype cavity of Fig. 1.1 are shown in Fig. 4.1(a). The blue-shaded area indicates the combinations of Δ_{CLS} and Γ_{SR} that can be realized. Interestingly, we find this set to be circular. Enhanced spontaneous emission is found everywhere, except at the lowest point of the circle, whereas the CLS can take positive, zero, as well as negative values. The whole circle is slightly shifted to negative CLS.

In order to explain the highly symmetric set of CLS and SR, we can consider a cavity at the boundary of the blue circle in Fig. 4.1(a), e.g., the cavity featuring highest SR. Fixing this cavity structure and tuning the angle of incidence around the first cavity resonance, the outermost black dash-dotted trajectory (i), indicated in Fig. 4.1(a), is traversed clockwise with increasing incidence angle. Raising the angle further towards the next-higher relevant cavity resonance, the second-largest circle (iii) indicated in the figure is gone through, and so on. The explicit parametrization of this trajectory with the angle of incidence is shown in Fig. 4.1(b). For each resonance structure, indicated by a peak in the SR and a zero in the CLS, a circle of different radius is traversed. Since the circle with largest diameter constitutes the boundary of the accessible CLSs and SRs, we find that the highest possible CLSs and SRs can be achieved within a single cavity geometry. This is consistent with previous predictions [88].

Fig. 4.1(c) shows the pole structure of the Green's function as a function of the angle of incidence. Noting that the resonant layer is placed precisely in the center of the guiding (carbon) layer for the cavity considered in Fig. 4.1, the thick, absorptive cladding (platinum) layers on both sides of the guiding layer effectively ensure a mirror-symmetry around the resonant layer. Therefore, the odd parity modes in the guiding layer feature nodes at the nuclear layer while the even parity modes can

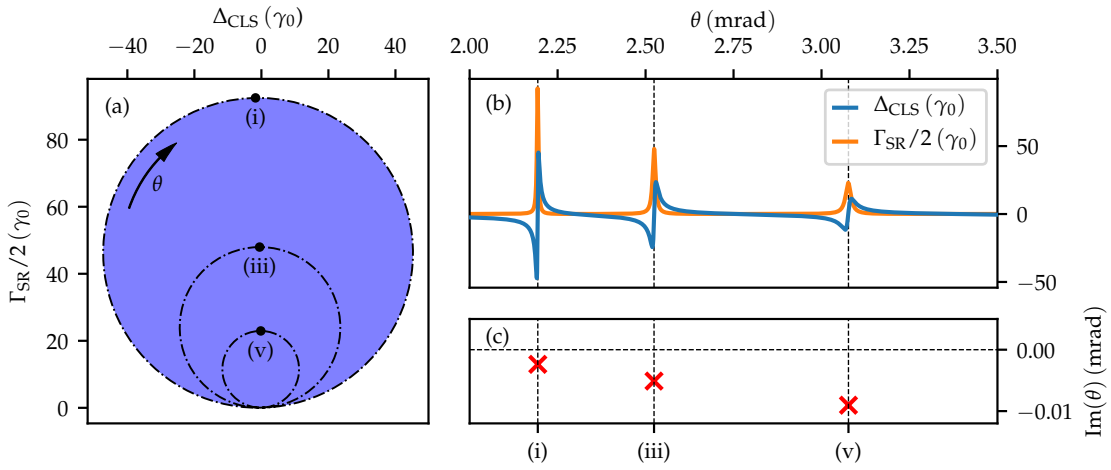

Fig. 4.1: Accessible OS for the resonance frequency shift Δ_{CLS} and the linewidth broadening Γ_{SR} of the artificial x-ray two-level system. The figure shows the archetype cavity with Pt/C/^{57}Fe/C/Pt/Si structure, as illustrated in Fig. 1.1(left). (a) The blue shaded area indicates the accessible combinations of Δ_{CLS} and Γ_{SR}. Starting from the topmost point with highest SR, the outermost, black dash-dotted circle is traversed upon tuning the angle of incidence around the first cavity resonance. The circles with smaller radii are accessed by tuning the incidence angles around the higher cavity modes. (b) Explicit parametrization of the trajectory in (a) in terms of Δ_{CLS} and Γ_{SR} via the angle of incidence. (c) shows the poles of the Green's function against the angle of incidence, which can be associated with the individual cavity modes. The dots on the curve in (a), labeled with lower-case roman numerals, relate the structures in (a) to the poles in (c). The cavity structure corresponding to the circles in (a) and the results in (b, c) is Pt(80.4 nm)/C(46.0 nm)/^{57}Fe(0.57 nm)/C(46.1 nm)/Pt(17.8 nm)/Si, where the notation gives the layer thicknesses in parenthesis after the layer material and Si is the substrate and therefore semi-infinitely extended to the bottom.

couple to the nuclei and, thus, are visible in Fig. 4.1(b) and (c). For this reason we leave out every second roman numeral for the labeling of the poles in Fig. 4.1. In Sec. 4.2 we will discuss cases for which also the modes (ii) and (iv) have visible contributions.

Notably, we find that each circle in Fig. 4.1(a) is associated to a respective pole in panel (c). The circles are traversed in a continuous way upon passing by the corresponding poles. To understand this behavior, we can express the Green's function by a Mittag-Leffler pole expansion [2, 66–68] (see also Sec. 2.1.1) in the angle of incidence θ at constant frequency, i.e. we write it as

$$G(\theta) = G(\theta = 0) + \sum_{\theta_0} \mathrm{Res}(G, \theta_0) \left(\frac{1}{\theta_0} + \frac{1}{\theta - \theta_0} \right) , \tag{4.1}$$

where θ_0 are the poles of the Green's function and $\mathrm{Res}(G, \theta_0)$ the respective residua. Each pole can be associated to a cavity mode coupling to the resonant layer [2]. The imaginary part of the pole then sets the width of the respective mode. For the cavity

at hand, Fig. 4.1(c) indicates that the imaginary parts of the poles are very small as compared to their real part separation. Being close to one pole thus allows to accurately describe the Green's function by a single-mode approximation,

$$G_{\mathrm{SM}}(\theta) = \mathcal{C} + \frac{\mathrm{Res}(G, \theta_0)}{\theta - \theta_0}\,, \tag{4.2}$$

where $\mathcal{C}$ accounts for the relevant terms constant in θ. Upon tuning θ, the expression maps to a circle in the complex plane spanning CLS and SR[1]. Explicitly, it can be shown that the circle has radius $r = |\mathrm{Res}(G, \theta_0)|/2\,\mathrm{Im}(\theta_0)$ and is centered at $\mathcal{C} + i\mathrm{Res}(G, \theta_0)/2\,\mathrm{Im}(\theta_0)$ in the complex plane. For the present case, we find that $\mathrm{Res}(G, \theta_0)$ and $\mathcal{C}$ are essentially always real. The Green's function then fulfills the simpler circle equation for all real θ,

$$\left[\mathrm{Re}\left(G_{\mathrm{SM}}(\theta) - \mathcal{C}\right)\right]^2 + \left[\mathrm{Im}\left(G_{\mathrm{SM}}(\theta) - i\frac{\mathrm{Res}(G, \theta_0)}{2\,\mathrm{Im}(\theta_0)}\right)\right]^2 = \left[\frac{\mathrm{Res}(G, \theta_0)}{2\,\mathrm{Im}(\theta_0)}\right]^2\,, \tag{4.3}$$

which is in accordance with the position of the circles in Fig. 4.1(a).

The residues and imaginary parts may vary among the different poles, which explains the distinct radii for the first three modes, visible in the trajectory in Fig. 4.1(a).

The small imaginary part of the poles is understood when realizing that the cavity design chosen for this discussion (i.e. the one at the boundary of the circle) features very thick cladding layers. This is not surprising since the latter raise the intra-cavity reflectivity and hence form the basis for stronger inter-nuclear couplings, thus accounting for larger collective effects. Likewise, larger intra-cavity reflectivity allows for more narrow modes which explains the poles' behavior.

4.2 Visibility as additional design goal

In the preceding Section 4.1, we found that the highest possible CLSs and SRs at the circle's boundary in Fig. 4.1(a) are realized in a cavity with thick cladding layers. However, while this increases the cavity-mediated couplings between the nuclei and thereby enhances the collective effects, it at the same time suppresses the coupling of light into and out of the cavity mode. Practically, this means that the associated artificial two-level schemes cannot be observed via the reflectance with high visibility in experiments. In order to quantify this practical restriction, we add the visibility, defined in Sec. 3.1.2, as a third observable characterizing the cavity performance.

To arrive at a comprehensive description of the relation between visibility and quantum optical parameters of the two-level scheme, we numerically determine the

[1] Actually, this behavior is not surprising, as the single mode approximated Green's function is a Möbius transformation. Those map the set of lines and circles in the complex plane to itself [89].

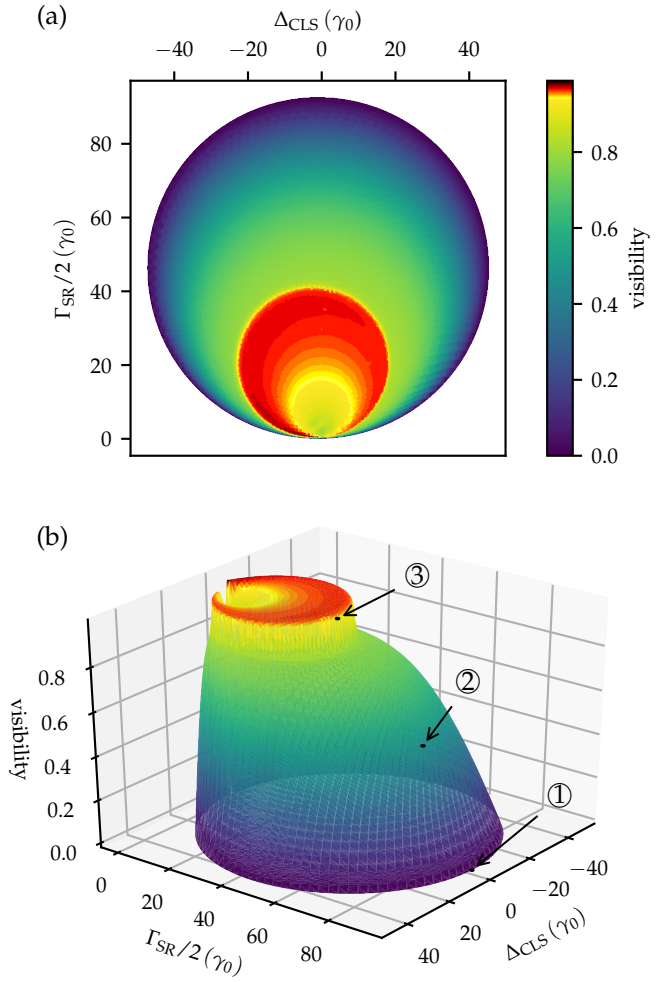

Fig. 4.2: Accessible OS for the artificial x-ray two-level system with the three design goals Γ_{SR}, Δ_{CLS} and visibility as obtained upon varying all layer thicknesses and the angle of incidence. Results are shown for Pt/C/^{57}Fe/C/Pt/Si cavity structures. (a) Projection of the OS into the Δ_{CLS}-Γ_{SR}-plane with the visibility color-coded. (b) Three dimensional representation of the OS in (a), which shows a plateau of high visibility as a distinct parameter region. Note that the accessible parameter combinations are not restricted to the surface only, but also encompass combinations inside the shown structure[2]. The cavities used for Figs. 4.1, 4.3 and 4.4 are marked in the figure by the symbols ①, ② and ③, respectively. Details on the numerical approach to generate the shown data are provided in Chapter 6.

surface of the OS for the visibility, the CLS and the SR. The result of this optimization is shown in Fig. 4.2. Note that the ring-like structures visible in Fig. 4.2(a) do not correspond to the seemingly similar structures in Fig. 4.1(a). While the former are obtained with different cavity structures, the latter are drawn for a single one. Likewise, Fig. 4.2(b) shows a three-dimensional representation of the overall possible

[2]By calculating the surface of panel (b), we indeed certify that the circular OS of CLS and SR is densely filled, that is for all observables within the circle a cavity can be found. Whether also the volume inside the 3D-surface of panel (b) is densely filled is not studied rigorously. However, many cavities' observables are found beneath the surface which indeed suggests a filled OS. Under this assumption, the numerical inverse design of the corresponding cavities is straightforward. Further, from an experimental point of view, the CLS and SR are proportional to the abundance of ^{57}Fe in the resonant layer. Reducing the abundance of ^{57}Fe in the resonant layer leaves the electromagnetic environment unchanged while – within the limits of discrete atoms – allowing to "shrink" the surface towards zero and thus obtain any combination of CLS and SR within the surface. In view of these points, the knowledge of the OS surface is sufficient for the inverse design in most cases.

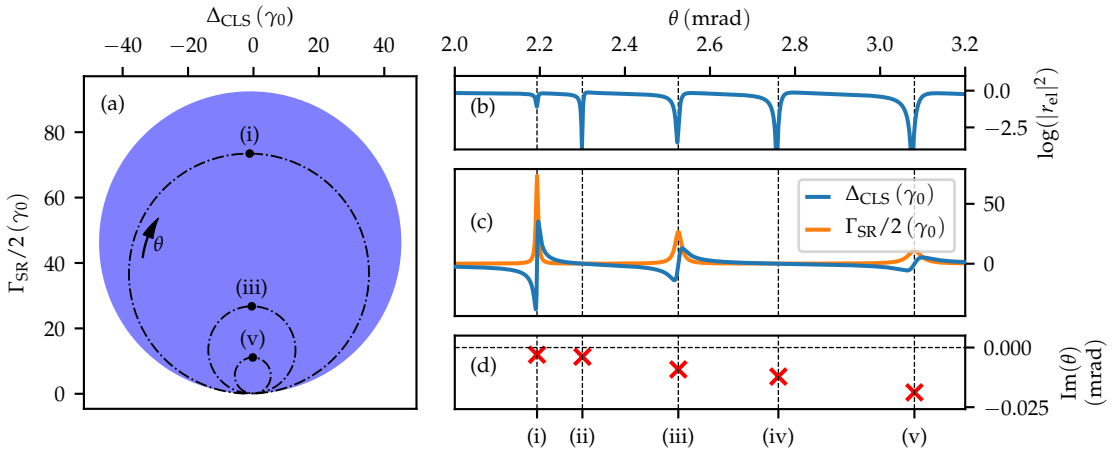

Fig. 4.3: Characterization of a cavity setup with the additional constraint of a 50%-visibility of the nuclear Fano line signature in the reflection spectrum. Panels (a), (c) and (d) are analogous to the corresponding panels in Fig. 4.1. Panel (b) further shows the reflected intensity ("rocking curve") as function of the angle of incidence θ. The cavity structure corresponding to the circles in (a) and the results in (b-d) is Pt(2.7 nm)/C(45.7 nm)/^{57}Fe(0.57 nm)/C(46.1 nm)/Pt(307.3 nm)/Si. The cavity is marked in the OS shown in Fig. 4.2(b). Note, that the visibility of about 50% is only achieved around (i) as also the visibility depends on the angle of incidence.

combinations of CLS, SR and visibility. Clearly, as discussed above, the maximum SRs and CLSs result in near-zero signatures in the reflectance. As we move away from the extremal values of CLS and SR, the accessible visibilities become larger, and eventually and indeed quite abruptly, a saturation to values very close to one (color-coded red in Fig. 4.2) is observed, while still allowing for comparatively high SR and CLS.

As a first example of practically relevant settings, we consider a cavity with a visibility of about 50%, i.e. the reflection spectrum is modulated by half the intensity impinging on the cavity. Within this constraint, we again search for the cavity realizing highest SR. The observables of the resulting cavity are indicated by the symbol ② in Fig. 4.2(b). Again fixing the different layer thicknesses and varying the angle of incidence, Fig. 4.3 shows the characteristics of the cavity, in a representation analogous to Fig. 4.1. Owing to the considerably reduced top cladding layer thickness (2.7 nm), that is necessary for the enlarged visibility, the SR accessible in this cavity is clearly lower, however, still significant. In addition to the previous panels, we also consider the intensity as reflected on the cavity in Fig. 4.3(b) which has not been a meaningful observable in Fig. 4.1 because of the high top-layer thickness leading to a vanishing signature of the cavity modes in the reflected intensity. Comparing Fig. 4.3(b) and (c), we see that only every second mode couples to the resonant layer. Although the poles in the Green's function are in principle present for modes (ii) and (iv), their numerical effect in Fig. 4.3(c) is negligible due to their odd parity

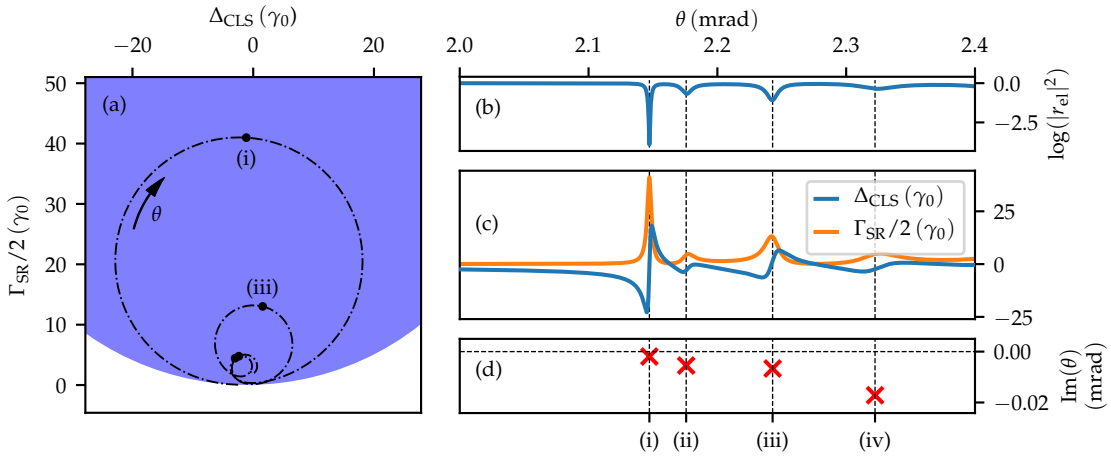

Fig. 4.4: Characterization of a C(80.1 nm)/^{57}Fe(0.57 nm)/C(102.6 nm)/Pt(17.6 nm)/Si cavity-setup, corresponding to a two-level system with high visibility of about 94%. This cavity is marked in the OS shown in Fig. 4.2(b). The panels are analogous to those in Fig. 4.3.

resulting in nodes at the resonant layer. While for higher order modes the minima of the reflected intensity in Fig. 4.3(b) do not coincide with the poles' real parts due to overlapping modes, these multi-mode effects [2] are suppressed in the Green's function since relevant modes have roughly twice the distance. Thus, the Green's function can still be treated by the single mode expression Eq. (4.2) and we find circles in Fig. 4.3(a).

Regarding the abrupt saturation to high visibilities in Fig. 4.2, we can explain this peculiar behavior by a qualitative change in the optimum geometries of the cavities. Counter-intuitively, the optimum cavities giving rise to this plateau of highest visibilities do not have any upper cladding layer. This is unexpected, as such structures are more similar to single-mirror settings, rather than cavities. Within the grazing incidence illumination, however, the reflection at the carbon-air interface can be of significant magnitude.

We illustrate the performance of such a cavity without top cladding in Fig. 4.4 (cf. indication ③ in Fig. 4.2). For the specific setting, the SR takes values up to about $40\,\gamma_0$ while maintaining a large visibility. In contrast to the previous examples Figs. 4.1 and 4.3, the cavity is not symmetric anymore and the coupling of different modes to the nuclei in the resonant layer in Fig. 4.4(c) does not follow a simple pattern as before. Prominently, the in-coupling into the first mode and the coupling of the first mode to the resonant layer are most pronounced. Since neighboring modes are not well-separated on the scale of their widths, the single-mode approximation of Eq. (4.2) is not applicable. In particular for higher order modes, the trajectories in Fig. 4.4 thus lose their circular appearance and become spiral-like as also nearby poles contribute.

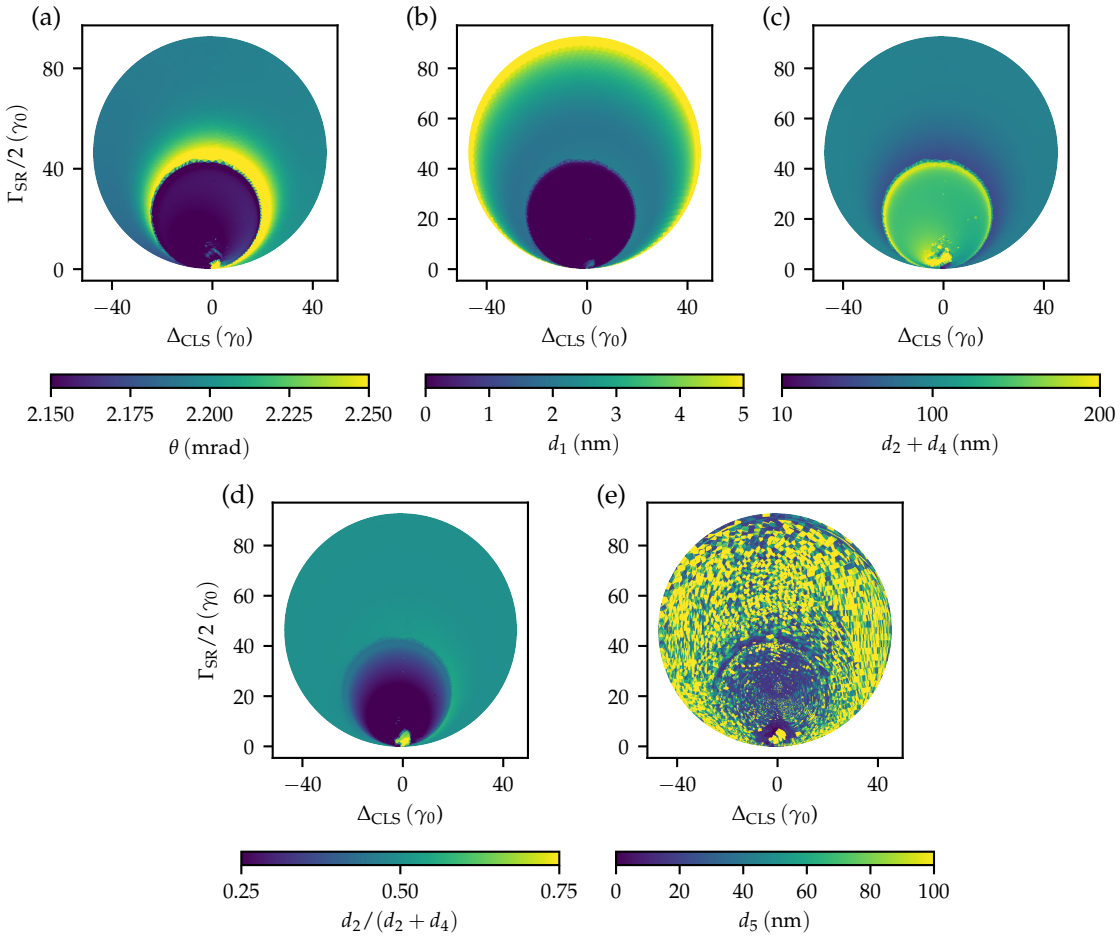

Fig. 4.5: Inverse design of the artificial two-level system. Results are shown for Pt/C/^{57}Fe/C/Pt/Si cavity systems. The panels show cavity parameters that allow for the design of the two-level systems of optimal visibility, see Fig. 4.2. These include (a) the angle of incidence, (b) the top cladding layer thickness, (c) the guiding layer thickness, (d) the relative position of the resonant layer in the guiding layer and (e) the bottom cladding layer thickness. See Fig. 1.1 for the illustration of the cavity parameters. From this figure, cavity parameters for all accessible two-level schemes can in principle be read off.

For future experiments, the plateau in Fig. 4.2 points to a new, possibly preferential approach since cavities without upper cladding provide very clear spectral signatures while still showing significant collective effects.

With the foregoing discussion we are not only able to give precise cavity structures for the realization of a desired quantum optical two-level scheme, but can also quantify to what extent it will be visible in the reflectance. To showcase the successful inverse design, Fig. 4.5 presents the cavity parameters that constitute the surface of optimal visibility at fixed CLS and SR in Fig. 4.2. The cavities are characterized by five parameters which are shown in Fig. 4.5(a)-(e). For each desired parameter set of the

artificial two-level system, the corresponding cavity design can in principle directly be read off.

From Fig. 4.5(e) we clearly see that the bottom cladding layer thickness is not described by a function continuous in the CLS and SR. This can be understood by the fact that from a certain thickness on, the system for all practical purposes is indifferent to a further increase in this thickness as the transmission through the bottom cladding is suppressed exponentially. Figure 4.5 also suggests that for most applications the usage of a thick bottom cladding is preferential. For the remaining parameters we find mostly continuous dependencies on the CLS and SR, which is somewhat unexpected as only three external constraints (CLS, SR and visibility) were imposed and our numerical procedure was not biased towards this continuous dependency. Overall, this completes the inverse design of artificial two-level schemes under the constraint of the nuclear response visibility in the reflection spectrum.

4.3 Intra-cavity field enhancement

In the previous sections, we found that the highest SRs and CLSs are realized in cavity structures with thick cladding layers, which do not allow for efficient in- and out-coupling of light, and therefore lack good visibility in the reflectance. In this section, we further explore this aspect by contrasting the CLS and SR with the intra-cavity enhancement of an external driving field at the resonant layer. The driving field strength is an important quantity as it enters the artificial two-level scheme via the effective Rabi-frequency Ω. We take this field enhancement as an additional design goal.

We illustrate the field enhancement by considering the field intensity distribution for an exemplary cavity in Fig. 4.6. When a plane-wave impinges on the cavity, part of it is directly reflected, leading to an intensity pattern outside the cavity. Inside the cavity, the light is "trapped" and therefore an enhanced intensity is found. The

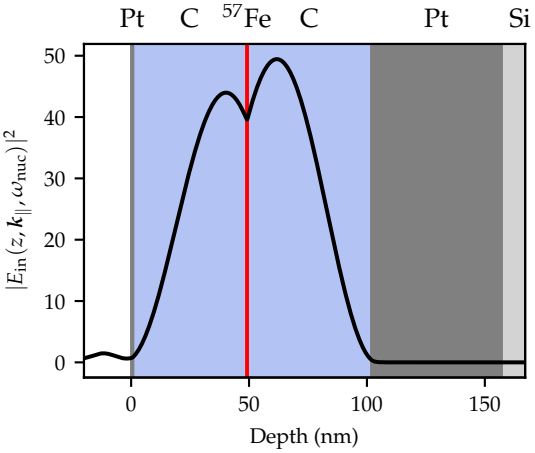

Fig. 4.6: Electric field intensity distribution in a Pt(0.89 nm)/C(50.0 nm)/^{57}Fe(0.57 nm)/C(52.4 nm)/Pt(55.3 nm)/Si cavity illuminated at 2.18 mrad with a plane-wave. Note that the intensity plotted is normalized to the incoming intensity, such that the enhancement at the nuclear layer can be directly read off to be about 40. The field distribution can be calculated, e.g., with Parratt's formalism [64] or using the PYNUSS [90] software package. Note that we show the off-resonant field, i.e. the ^{57}Fe contributes to the calculation only with its electronic refractive index, as is necessary within the used formalism.

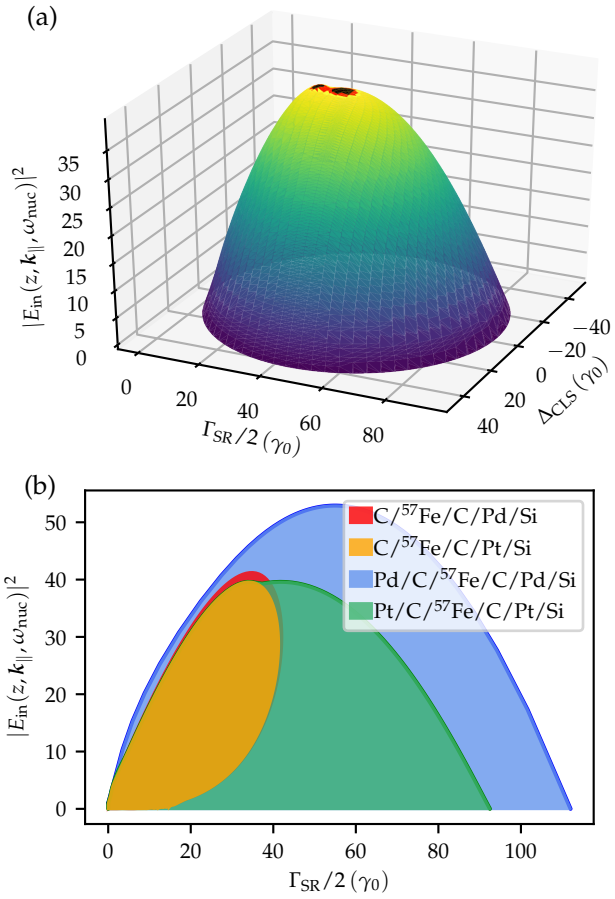

Fig. 4.7: Accessible OS for the artificial x-ray two-level system with the cavity-induced field enhancement at the position of the nuclei as an additional design goal. (a) The surface of all accessible combinations of the three observables CLS, SR and field enhancement is obtained, and shown as a 3d plot with color coding. Combinations on and beneath the surface are accessible. The coloring highlights the double tip structure of the OS close to the highest possible field enhancements. This panel shows results for Pt/C/^{57}Fe/C/Pt/Si cavity structures. (b) Section through panel (a) along the SR axis. The graph further compares the results for cavities with and without top cladding, as well as Pd and Pt as cladding materials, to explain the origin of the double-tip structure visible in (a).

archetypal standing wave structure is however disturbed by the impedance mismatch between the guiding layer and the isotope material. The height of the intensity at the nuclear layer (red) is what we refer to as field enhancement inside the cavity.

In comparison to CLS and SR, different optimal cavity designs may occur for the field enhancement. While the optimization of the latter relies on a compromise between coupling of external fields into the cavity mode and enhancement of the intensity inside the cavity by multiple reflections, CLS and SR are maximized in the absence of coupling into- and out of the cavity mode, as was discussed in Sec. 4.2.

In a first step, we analyze the accessible OS for CLS, SR and field enhancement in the archetype cavity of Fig. 1.1 and comment on the peculiarities of this very setting. Subsequently, we proceed to compare the results to the behavior expected for an optical Fabry-Pérot cavity and outline the conceptional differences.

4.3.1 Results for x-ray thin-film cavities

The accessible combinations of CLS, SR and field enhancement at the nuclear layer are shown in Fig. 4.7(a). As expected, we find minimal field enhancement for the case of maximum CLS and SR. In going towards higher field enhancement, the maximum possible CLS and SR decrease. Interestingly, the OS features a double tip near the maximum field enhancements, which is marked in black for clarity. To analyze its origin, we show a cut through panel (a) along the SR axis in Fig. 4.7(b) (green shaded area). This panel also shows corresponding results for a cavity without the topmost cladding layer (orange shaded area). One can clearly see that one of the two peaks can be attributed to cavities without the topmost layer. The second peak with similar maximal field enhancement is due to an entirely different cavity structure with a cladding layer. The respective cavity was tacitly shown in Fig. 4.6. As in Sec. 4.2, we again find that cavities without upper cladding layer may form an equally good, or even superior, approach to designing x-ray layer structures.

To contextualize these observations, we finally consider cavities in which the cladding material is changed from Pt to Pd. Results are shown with (blue) and without (red) top cladding in Fig. 4.7(b). For this material combination, no double-tip appears, and the non-cladded system is outperformed by the system with topmost Pd layer. This indicates that the Pt/C cavity system is peculiar, but also that the material choice is of great significance.

However, before elaborating on the topic of different materials in Sec. 4.4, there is yet another striking feature visible in Fig. 4.7(b). The decay enhancement for a quantum system is linked to the photonic density of states (DOS) at its position [86]. In Fig. 4.7, we see that the maximum in the field enhancement is reached at moderate SRs. This shows that the field enhancement is maximized in a different cavity geometry than the SR. In view of the standing wave-patterns shown in Sec. 3.2, one might have suspected that these are closely related to the field distribution inside the cavity which makes the difference in the maxima of SR and field enhancement somewhat counter-intuitive. Considering standard Fabry-Pérot cavities, we illustrate in the following section that one indeed can expect the coincidence of maximal field- and decay enhancement in optical cavities.

4.3.2 Comparison with optical Fabry-Pérot cavities

To illustrate this qualitative difference, we analyze a one-dimensional lossy Fabry-Pérot cavity as shown in Fig. 4.8(a). The mirror material is chosen as diamond for its comparatively large refractive index of $n = 2.4$, yet noting that variations of this refractive index only lead to quantitative, but not qualitative, changes. The cavity is illuminated at the resonance frequency of the two-level system (chosen around a wavelength of 700 nm) orthogonally to the mirror surface. For this setting, we seek the achievable combinations of frequency shift, decay enhancement and field

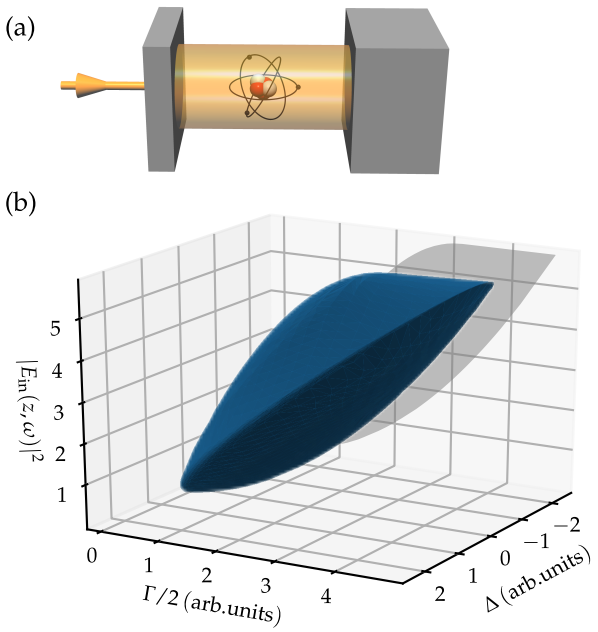

Fig. 4.8: Accessible OS for a two-level atom in a Fabry-Pérot cavity, as a reference for comparison with the x-ray thin-film cavity case in Fig. 4.7. (a) Schematic layout of the setup. The cavity is formed by diamond front and rear mirrors with rear thickness chosen large. A single two-level atom is coupled to the cavity field. The cavity is probed with light resonant to the atomic transition frequency. (b) OS of the accessible frequency shifts Δ and decay rate enhancements Γ in the Fabry-Pérot cavity. For each pair Δ, Γ, the possible field enhancements at the atom's position z are obtained, and shown as the third axis. The projection of the OS onto the $\Gamma - |E_{\mathrm{in}}(z,\omega)|^2$ plane is indicated. Unlike in the x-ray cavity case, the maxima of the line broadening Γ and the field enhancement $|E_{\mathrm{in}}(z,\omega)|^2$ coincide.

enhancement at the two-level system. It is readily described by the previously used formalism of Eqs. (2.15-2.17) in the limit of a single atom. The coupling constants can be obtained from the Green's function in Appendix A.1.1, which reduces to the one-dimensional real-space Green's function upon setting $\boldsymbol{k}_{\parallel} = 0$ [87].

To ensure comparability to the x-ray scenario, we not only vary the thicknesses of the layers and the position of the two-level atom therein, but also take its resonance frequency as a parameter. Varying the frequency in this setting is tantamount to changing the angle in the x-ray case, as the angle can be used to tune the thin-film cavity in and out of its resonances, which can be mapped to changing the frequency [49].

Fig. 4.8(b) shows the set of accessible combinations of field enhancement at the two-level system's position, level shift and decay enhancement. For clarity, we also show the projection of the set onto the SR-field enhancement-plane. Clearly, the maximal SR coincides with the largest possible field enhancement, as was suspected for this setting.

We can identify two major differences between the x-ray cavities and the Fabry-Pérot setting: Firstly, x-ray materials tend to have high absorption compared to dielectrics available in the optical regime, and, secondly, the grazing incidence setup allows for total reflection and thus provides a different mechanism of trapping light. Regarding the second point, it is important to note that x-ray cavities as in Fig. 1.1 are operated below the angle of total reflection of the cladding layer, such that the in- and out-coupling will take place evanescently. Therefore, the coupling of light

into and out of the cavity may be suppressed by thick cladding layers even in the absence of absorption in the mirror material. In contrast, in this case, the photonic DOS may still be high, since it is limited essentially only by the absorption of the guiding layer. Hence, we can attribute the counter-intuitive behavior of photonic DOS and field enhancement to the grazing incidence setup.

This illustrates that not all intuition from well-understood standard optical cavities can be directly translated to x-ray thin-film cavities, but systematic analysis is necessary. Striving for higher finesse cavities, as is done in the visible domain, would go in line with neither driving the nuclei nor observing the nuclear dynamics in the reflection spectrum. We note, however, that different in- and out-coupling schemes such as front-coupling [41, 91, 92] or intra-cavity generation of light [85] could allow one to enhance the intra-cavity field enhancement without reducing the SR and CLS.

Finally, for the x-ray thin-film case, we further note that although the SR and the field enhancement at the nuclear layer assume their respective maxima at different cavity parameters, the maxima may still coincide as a function of the angle of incidence only, for a single cavity structure.

Even though the qualitative behavior of the OS is not affected by absorption, we nevertheless find it to exert striking influence on the quantitative performance of cavities. Therefore, the influence of guiding and cladding material properties is discussed in the following section.

4.4 Influence of the material choice

At x-ray frequencies, materials are commonly found to have refractive indices close to and slightly below one, see Eq. (2.3). For the design of x-ray thin-film cavities, the guiding principle to choose materials commonly is taking *high-Z*, i.e. high atomic number and thus high electron density, materials for the cladding and *low-Z* materials for the guiding layer [19, 27, 50, 52, 54, 55, 93]. This guideline ensures high contrast in the real parts of the refractive indices and thus a comparatively large Fresnel reflectivity between adjacent layers. High electron densities, however, come along with high absorption, which affects the cavity performance. The interplay between absorption and reflectivity of the cladding is not immediately clear, which is why we devote this section to the systematic analysis of the performance of different material combinations for the archetype cavity of Fig. 1.1.

To derive trends for the material choice, we sample the cladding and guiding materials from a range of elements as well as few chemical compounds known to be suitable for the manufacturing process[3]. The ^{57}Fe-layer as well as the silicon substrate are left unchanged and the materials of the two cladding layers are taken

[3]The sampled materials are Ag, Al, Au, B_4C, Ba, Bi, B, Ca, Cd, Ce, Co, Cr, Cu, C, Dy, Er, Eu, Fe, Ga, Gd, Ge, Hf, Ho, In, Ir, J, La, Lu, MgO, Mg, Mn, Mo, Nb, Nd, Ni, Os, Pb, Pd, Pr, Pt, P, Re, Rh, Ru, Sb, Sc, Se, Si, Sm, Sn, Sr, S, Ta, Tb, Te, Ti, Tl, Tm, V, W, Yb, Y, Zn, Zr.

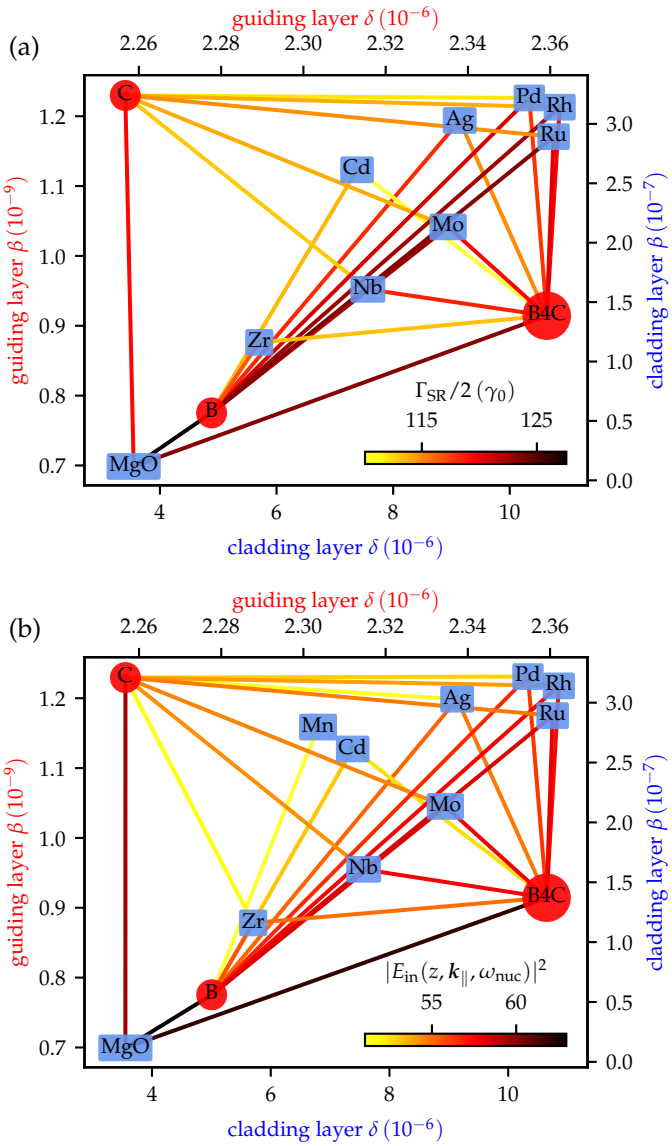

Fig. 4.9: Survey of the tunability of the artificial x-ray two-level system as a function of the chosen layer materials. Panel (a) shows the achievable SR, while panel (b) shows the field enhancement at the position of the nuclei. In each panel, the top [left] axes denote the real [imaginary] part of the refractive index $n = 1 - \delta + i\beta$ of the guiding layer material. Analogously, the bottom [right] axes characterize the refractive index of the cladding material. The different cladding [guiding] materials are shown as blue rectangular boxes [red circles] in the plot. Each line connecting a guiding-layer with a cladding-layer material defines a cavity structure. The optimum performance possible with this material combination is then color-coded in the line linking the two materials.

to be the same. We note that related material samplings have previously been reported in the context of bandpass filtering of broadband synchrotron radiation with grazing-incidence anti-reflection (GIAR) films [94].

For each material combination we seek the highest possible field enhancement at the nuclear layer as well as highest possible SR. From the circular structures in Fig. 4.1(a) and the pole expansion Eq. (4.2) it can be expected that the cavities optimizing the SR also optimize the CLS. The best extremization outcomes for the SR and the field enhancement are shown in Fig. 4.9(a) and (b), respectively.

We explain the plot at the example of the maximum SR for a cavity comprising Ag cladding layers and a B_4C guiding layer. From the top and left axes in Fig. 4.9(a)

we can read off that B_4C (red circle) has a refractive index of roughly $n = 1 - 2.36 \times 10^{-6} + 0.9 \times 10^{-9} i$. Similarly, we extract from the bottom and right axes that the refractive index of silver (blue rectangle) is about $n = 1 - 9 \times 10^{-6} + 3 \times 10^{-7} i$. Of course, the performance of the cavity is determined by both, cladding and guiding material. Therefore, the color of the line linking both materials (here: orange) indicates that $\Gamma_{\mathrm{SR}}/2 \approx 115\,\gamma_0$, as can be read off from the color bar. Analogously, all remaining pairs can be evaluated, also for Fig. 4.9(b).

As expected, we find that the best cavities feature low absorption in the guiding layers. For the cladding materials, however, common materials such as Pt are neither among the best cavities for SR nor for the field enhancement (and hence do not even appear in the sampling in Fig. 4.9 where only the best combinations were included). This is unexpected, since Pt is a high-Z-material with comparatively high δ which gives rise to a high Fresnel reflectivity at the cladding-guiding boundary. Overall, we find that Pt is not an exception, because the best cavities are not achieved via a high contrast in the refractive indices' real parts, but rather with the low absorption in the cladding as a selection criterion. Most strikingly, all metals are outperformed by the MgO compound as cladding material which shows the lowest β among the cladding materials present in Fig. 4.9. Nevertheless, it should be stressed that also for low-absorption cladding materials it remains important that $\delta_{\mathrm{cladding}} > \delta_{\mathrm{guiding}}$ to maintain the mirror-like function of the cladding while having low guiding layer absorption.

Summarizing, the results indicate that the paradigm of *high-Z*-cladding – *low-Z*-guiding material as a cavity design criterion has to be reconsidered. Instead, implementing *low-Z*-cladding – *lower-Z*-guiding layer materials shows a clear potential for improving the performance of state-of-the-art cavities and their applications.

Finally, we note that sampling the top and the bottom cladding layer materials independently still suggests that the best performance is achieved if both layers are of the same material and lowest sensible absorption.

4.5 Influence of the resonant isotope choice

Having discussed the accessible CLSs and SRs, the reflection spectrum visibility of the nuclear response, the field enhancement and relevant material aspects for thin-film cavities, it remains to address the influence of different resonant isotopes on the performance of archetype cavities. Taking a key role in the properties of the artificial quantum system to be designed, their influence is two-fold.

Firstly, each isotope comes with intrinsic properties. They determine the coupling of the nuclear transition to the electromagnetic environment and thus fix the scale of collective effects. Secondly, even ultra-thin layers of resonant isotopes modify the field configuration in the cavity by their electronic refractive index. Exchanging the resonant isotope thus strongly affects the cavity mode structure. Furthermore, the

	$\omega_{\mathrm{nuc}}\,(\mathrm{keV})$	$\delta_{\mathrm{iso}}+i\beta_{\mathrm{iso}}\,(10^{-6})$	$\delta_{\mathrm{C}}+i\beta_{\mathrm{C}}\,(10^{-6})$
^{57}Fe	14.4	$7.3+0.33i$	$2.3+1.2\times10^{-3}i$
^{119}Sn	23.9	$2.2+0.037i$	$0.82+2.8\times10^{-4}i$
^{45}Sc	12.4	$3.8+0.13i$	$3.1+2.2\times10^{-3}i$

Tab. 4.1: Properties of the Mössbauer isotopes ^{57}Fe, ^{119}Sn and ^{45}Sc and the Carbon guiding layer at the respective Mössbauer resonance frequencies. The electronic refractive index of the resonant isotope at its transition frequency is denoted as $n_{\mathrm{isotope}}=1-\delta_{\mathrm{iso}}+i\beta_{\mathrm{iso}}$ and the respective one of Carbon reads $n_{\mathrm{C}}=1-\delta_{\mathrm{C}}+i\beta_{\mathrm{C}}$. The isotope's transition frequency is given by ω_{nuc}. Parameters are taken from [46] or calculated with the PYNUSS [90] software package.

refractive indices of the cavity materials and the optimal geometries are subject to the light's wavelength and thus to the nuclear transition frequency, which thereby also influences the modal structure.

In the following, we disentangle the influence of both effects on the cavity performance and outline the consequences on the design of artificial few-level systems. To this end, we consider the OSs of the SR and the field enhancement at the resonant layer for the isotopes ^{57}Fe, ^{119}Sn and ^{45}Sc. These isotopes have transition frequencies accessible with state-of-the-art pulsed x-ray sources, but feature rather different properties. The transition frequencies and electronic refractive indices of these isotopes are given in Tab. 4.1. The isotopes are chosen to be embedded in a Pd/C/isotope/C/Pd/Si cavity. We note that for better comparability, we chose the thickness of the resonant layer as 0.574 nm in all cases, as was previously used for the ^{57}Fe cavities. The accessible parameter combinations are shown in Fig. 4.10. ^{45}Sc and ^{119}Sn stand out with very high field enhancements, but comparably low tuning capability in the SR. In comparison, ^{57}Fe exhibits comparatively high possible SR in combination with moderate field enhancement. This highlights that in optimizing x-ray cavity structures towards a given design goal, also the resonant isotope should be considered as an important design parameter.

4.5.1 Direct impact of the nuclear properties

To disentangle the effects of exchanging the nuclear isotope on the cavity performance, we first try to compare the results for the different isotopes via a naive scaling of their parameters.

Following Eqs. (3.3) and (3.4), the dependencies of CLS and SR on the nuclear properties are given by

$$\Delta_{\mathrm{CLS}},\Gamma_{\mathrm{SR}}\propto\omega_{\mathrm{nuc}}^2|d|^2G(\omega_{\mathrm{nuc}})\frac{N}{A}. \tag{4.4}$$

We can express the dipole moment in this relation as [48]

$$|d|^2=\frac{2\pi\gamma_0}{\omega_{\mathrm{nuc}}^3}\frac{1}{2(1+\alpha)}\frac{2I_{\mathrm{e}}+1}{2I_{\mathrm{g}}+1}, \tag{4.5}$$

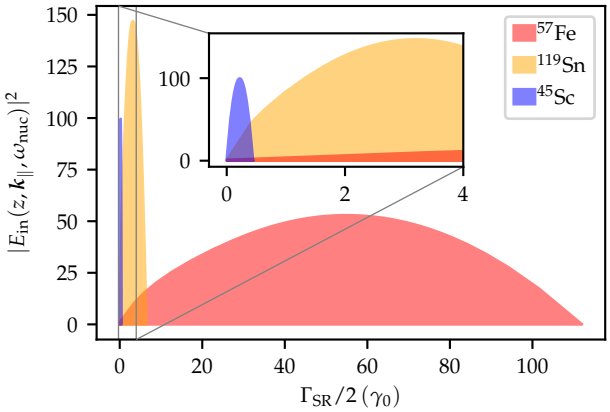

Fig. 4.10: Accessible OS for the SR of the artificial x-ray two-level system and the cavity-induced field enhancement at the position of the nuclei for several resonant isotopes. In all cases, the optimization was performed with a Pd/C/isotope/C/Pd/Si cavity structure. It can be seen that cavities with ^{119}Sn and ^{45}Sc feature superior field enhancements, while the use of ^{57}Fe offers comparably large SRs in units of the respective natural line width γ_0.

where α is the coefficient of internal conversion and I_e (I_g) is the nuclear spin of the excited (ground) state of the transition. Moreover, the effective in-plane nuclear number density can be written as

$$\frac{N}{A} = d_3 \rho_N a f_{LM}\,, \tag{4.6}$$

with the Lamb-Mössbauer factor f_{LM}, the number density per volume of the material ρ_N, the thickness of the resonant layer d_3 and the abundance a of the resonant isotopes therein.

Regarding the Green's function (A.1), we note that the Fresnel coefficients in Eq. (A.2) are unaffected by the frequency dependence, such that we find a scaling $G(\omega_{nuc}) \propto 1/\omega_{nuc}$ with the isotope's transition frequency, owing to $\beta_j \propto \omega_{nuc}$.

Taking into account all these scalings, we can estimate the CLS and SR of a specific isotope on the basis of the numerically calculated performance of ^{57}Fe. However, upon comparing these estimates to the results in Fig. 4.10, we find that the SRs actually calculated for ^{119}Sn and ^{45}Sc are significantly higher than those expected from the naive scaling. This is a clear indication that the nuclear transition's properties alone are not sufficient to characterize the performance of an isotope in a thin-film cavity. Instead, also the modification of the cavity environment due to the exchange of the isotope layer must be considered.

4.5.2 Impact of the nuclear isotope on the cavity environment

Next, we study the influence of the isotope choice on the electromagnetic environment provided by the cavity. Exchanging the resonant isotope alters the photonic DOS as, on the one hand, each resonant isotope comes with its specific electronic refractive index, and, on the other hand, its resonance frequency affects the refractive indices of the remaining layers. As can be seen from Tab. 4.1, the carbon guiding layer's refractive index approaches unity with increasing frequency of the isotopes, as common for x-ray materials [65]. For the refractive index of the resonant isotopes

themselves there is no such clear trend with respect to the transition frequency as it competes with their electron density.

To estimate the effect of the isotope choice on the photonic DOS, we consider the achievable field enhancement at the nuclear layer as shown in Fig. 4.10. Even though in Sec. 4.3 we noted that field enhancement and SR are realized in different geometries, this is a sensible choice as we do not compare geometries but the materials of the resonant layer. In that respect, the results in Sec. 4.4 suggest that within one setting of materials, the maximum achievable SR and field enhancement are correlated to each other. Finally, the field enhancement is particularly useful as it is irrespective of the nuclear properties.

Comparing the refractive indices in Tab. 4.1 to the results in Fig. 4.10, it is clear that low absorption in the cavity, and, in particular, in the resonant layer, is the driving factor for the photonic environment. The very high field enhancement for ^{119}Sn and significantly reduced enhancement for ^{57}Fe due to the electromagnetic environment complement very well the incompleteness of the description found in Sec. 4.5.1 upon considering the nuclear properties only.

This shows that considering the nuclear properties alone is not sufficient to estimate an isotope's potential. Rather, the effect of the isotope on the electromagnetic environment has to be taken into account for a comprehensive description.

5 Inverse design of three-level systems

Having discussed in detail archetypal cavity geometries with a single layer of resonant nuclei, this chapter illustrates that the inverse design approach can be extended to more complex systems. Specifically, in this chapter, we demonstrate the inverse design of three-level systems as they are realized in cavities comprising two resonant layers. Such level schemes are of great interest as they allow for the realization of advanced quantum optical effects.

We start by adapting the general theory of Sec. 2.2 to the two resonant layer case, which yields the effective three-level scheme description. We then consider the accessible properties of the three-level scheme and relate these to the cavity's mode structure. Subsequently, we turn towards the design of ratios of level scheme paramters as they are relevant for the realization of quantum optical effects. On that basis, we address the design of a nuclear EIT scheme and comment on open questions regarding its interpretation. Finally, we introduce an approach that describes the nuclear imprint on the reflection spectrum on the basis of excitonic normal modes. This method directly allows to understand and engineer the reflection spectrum.

5.1 Two resonant layers – three-level scheme

An archetypal cavity geometry with two resonant layers is shown in Fig. 5.1(a). Having two resonant layers placed in the cavity, a spin-wave can be excited in each of the layers, leaving us with the Hamiltonian of two coupled two-level systems according to Eq. (2.21),

$$\begin{aligned}\hat{H} =& \frac{\omega_{\mathrm{nuc}}}{2}\hat{\sigma}_1^z + \Delta_{\mathrm{CLS},1}\hat{\sigma}_1^+\hat{\sigma}_1^- + \frac{\omega_{\mathrm{nuc}}}{2}\hat{\sigma}_2^z + \Delta_{\mathrm{CLS},2}\hat{\sigma}_2^+\hat{\sigma}_2^- \\ & - \left(\Delta_{12}\hat{\sigma}_1^+\hat{\sigma}_2^- + \mathrm{h.c.}\right) - \left(\Omega_1\hat{\sigma}_1^+ + \mathrm{h.c.}\right) - \left(\Omega_2\hat{\sigma}_2^+ + \mathrm{h.c.}\right) , \end{aligned} \tag{5.1}$$

where we omitted the $\boldsymbol{k}_{\parallel}$ index for readability. Here, we introduced the frequency shifts

$$\Delta_{\mathrm{CLS},1} = -\Delta_{11} , \quad \Delta_{\mathrm{CLS},2} = -\Delta_{22} , \tag{5.2}$$

which are defined via Eq. (2.26).

In principle, this Hamiltonian describes the effective dynamics in a four dimensional space. For the dynamics in the low-excitation regime, however, we already noted in Sec. 2.2.2 that the doubly excited state is irrelevant for the dynamics, thus leaving

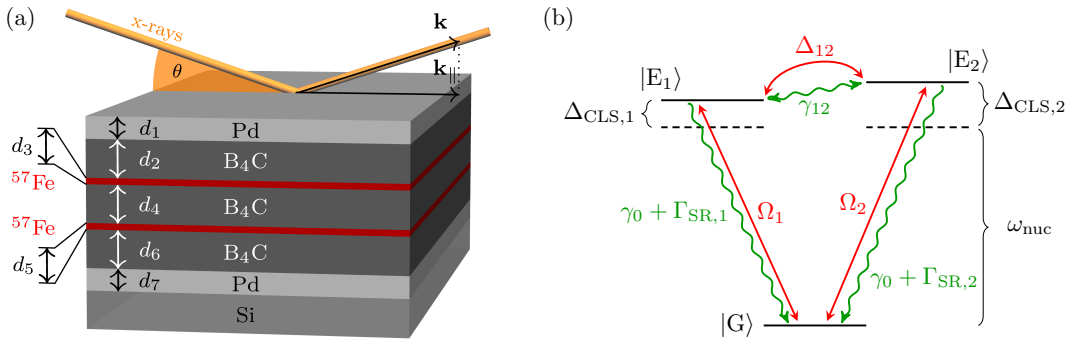

Fig. 5.1: Schematic setup of an exemplary thin-film cavity with two resonant layers (a) and illustration of the respective level scheme (b). Both resonant layers are embedded in a single guiding layer for the presented system. The layer thicknesses as well as exemplary materials are indicated in panel (a). The resulting level scheme shown in panel (b) comprises three levels. A ground state $|\mathrm{G}\rangle$ with no excitation in the resonant layers and excited states $|\mathrm{E}_1\rangle$ ($|\mathrm{E}_2\rangle$) whose energy is shifted by $\Delta_{\mathrm{CLS},1}$ ($\Delta_{\mathrm{CLS},2}$) as compared to the bare nuclear transition frequency and which decay with rates enhanced by $\Gamma_{\mathrm{SR},1}$ ($\Gamma_{\mathrm{SR},2}$). The field that impinges on the cavity leads to a driving of the transitions from $|\mathrm{G}\rangle$ to $|E_1\rangle$ ($|\mathrm{E}_2\rangle$) with Rabi frequency Ω_1 (Ω_2). Additionally, coherent Δ_{12} and incoherent γ_{12} couplings between the excited states are mediated by the cavity. Note that we often refer to the excited states as *nuclear excitons*.

us with a three-level description. Since the dipole moments in the first and second resonant layer are identical $d_1 = d_2$, the dipole-dipole coupling of strength Δ_{12} between the spin-waves is real and hence symmetric in the present case, $\Delta_{12} = \Delta_{21}$.

Additionally to the decay enhancements of the spin-waves [see Eq. (2.27)],

$$\Gamma_{\mathrm{SR},1} = \gamma_{11}\,, \quad \Gamma_{\mathrm{SR},2} = \gamma_{22}\,, \tag{5.3}$$

the Lindbladian comprises an incoherent coupling γ_{12} between the spin-wave excitations according to Eqs. (2.22) and (2.27). This coupling is also real and symmetric for the present case, $\gamma_{12} = \gamma_{21}$. Such cross-decay terms are typically not present for standard three-level systems. The resulting level scheme is shown in Fig. 5.1(b).

5.1.1 Reflection spectrum

According to Eq. (2.20), the two spin-wave operators' expectation values form a system of linear coupled differential equations,

$$\begin{aligned}\dot{\sigma}_1^-(t) = &-i(\omega_{\mathrm{nuc}} + \Delta_{\mathrm{CLS},1} - i\frac{\gamma_0 + \Gamma_{\mathrm{SR},1}}{2})\sigma_1^-(t) + i\left(\Delta_{12} + i\frac{\gamma_{12}}{2}\right)\sigma_2^-(t) \\ &+ i\frac{N}{A}d_1^* E_{\mathrm{in}}(z_1, \boldsymbol{k}_\parallel)\,,\end{aligned}$$

$$\dot{\sigma}_2^-(t) = -i(\omega_{\mathrm{nuc}} + \Delta_{\mathrm{CLS},2} - i\frac{\gamma_0 + \Gamma_{\mathrm{SR},2}}{2})\sigma_2^-(t) + i\left(\Delta_{12} + i\frac{\gamma_{12}}{2}\right)\sigma_1^-(t) + i\frac{N}{A}d_2^* E_{\mathrm{in}}(z_2, \boldsymbol{k}_\parallel)\,. \tag{5.4}$$

As before, we transform to frequency space, and approximate the driving fields as constant in frequency on the scale of the nuclear linewidth. In frequency space, we can conveniently rewrite the resulting expressions in matrix-vector notation,

$$\tilde{\boldsymbol{\Omega}} = -\boldsymbol{\mathcal{M}}(\omega)\cdot\boldsymbol{\sigma}^-(\omega)\,, \tag{5.5}$$

where we defined the vector comprising the expectation values of the spin-wave operators and the driving vector,

$$\boldsymbol{\sigma}^-(\omega) = \begin{pmatrix} \sigma_1^-(\omega) \\ \sigma_2^-(\omega) \end{pmatrix}, \quad \tilde{\boldsymbol{\Omega}} = i\frac{N}{A}\begin{pmatrix} d_1^* E_{\mathrm{in}}(z_1, \boldsymbol{k}_\parallel, \omega_{\mathrm{nuc}}) \\ d_2^* E_{\mathrm{in}}(z_2, \boldsymbol{k}_\parallel, \omega_{\mathrm{nuc}}) \end{pmatrix}, \tag{5.6}$$

respectively. We further introduced the matrices,

$$\boldsymbol{\mathcal{M}}(\omega) = i\left[(\omega - \omega_{\mathrm{nuc}} + i\frac{\gamma_0}{2})\mathbb{1} + \boldsymbol{C}\right], \tag{5.7}$$

$$\boldsymbol{C} = \begin{pmatrix} -\Delta_{\mathrm{CLS},1} + i\Gamma_{\mathrm{SR},1}/2 & \Delta_{12} + i\gamma_{12}/2 \\ \Delta_{12} + i\gamma_{12}/2 & -\Delta_{\mathrm{CLS},2} + i\Gamma_{\mathrm{SR},2}/2 \end{pmatrix}, \tag{5.8}$$

where the coupling matrix $\boldsymbol{C}$ is frequency independent and comprises all collective cavity-mediated couplings. We can readily obtain the frequency space solution of the dynamics, $\boldsymbol{\sigma}^-(\omega) = -\boldsymbol{\mathcal{M}}^{-1}(\omega)\cdot\tilde{\boldsymbol{\Omega}}$, which is subsequently inserted in Eq. (2.31) to yield the reflection spectrum. Keeping the matrix-vector notation it reads

$$r(\omega) = r_{\mathrm{el}} - \mu_0\omega_{\mathrm{nuc}}^2\tilde{\boldsymbol{G}}\cdot\boldsymbol{\mathcal{M}}^{-1}(\omega)\cdot\tilde{\boldsymbol{\Omega}}\,, \tag{5.9}$$

where the propagation to the surface is included in the expression

$$\tilde{\boldsymbol{G}} = \begin{pmatrix} G(0, z_1, \boldsymbol{k}_\parallel, \omega_{\mathrm{nuc}})d_1 \\ G(0, z_2, \boldsymbol{k}_\parallel, \omega_{\mathrm{nuc}})d_2 \end{pmatrix}. \tag{5.10}$$

This allows to determine the reflection spectrum of the system on the basis of the electromagnetic Green's function.

Hence, we now have the necessary tools to describe the artificial three-level scheme and calculate its experimentally observable reflection spectrum.

5.2 Designing three-level scheme properties

Having described the theoretical foundations of artificial three-level schemes, we turn towards the determination of the accessible properties of these systems.

As a cavity setup, we consider the thin-film cavity illustrated in Fig. 5.1(a). Basically, the cavity is analogous to the single resonant layer cavity analyzed in the previous chapter (see Fig. 1.1), however, with two resonant layers embedded in the guiding layer. We use Pd as the cladding material and B_4C as the guiding material. Qualitatively, different cavity setups comprising two resonant layers are possible and we will give another example in Sec. 5.5.3, see Fig. 5.15.

The level scheme resulting from two resonant layers in Fig. 5.1(b) is subject to the various layer thicknesses and the angle of incidence. As before, we fix the ^{57}Fe layer thicknesses to 0.574 nm for them to be ultrathin, such that the treatment of the nuclei as two-level systems is adequate. Within this setting, we determine the accessible quantum optical properties. We first consider the cavity-mediated coupling of the excited states to each other as well as the modification of their transition frequencies and decay enhancements. Subsequently, we also take into account the field enhancements at the resonant layers, similarly to Sec. 4.3.

5.2.1 Excitonic coupling and self-coupling

According to Eq. (5.8), the coupling matrix $\boldsymbol{C}$ depends on the frequency shifts of both excited states and their decay enhancements (i.e., their excitonic self-coupling) as well as the coherent and incoherent couplings of the excitons to each other. The accessible OSs for these observables are shown in Fig. 5.2. We first discuss the OSs accessible and then explain their appearance on the basis of the mode structure of the cavity.

From Fig. 5.2(b) and (c), we see that circular OSs are accessible for the frequency shifts and decay enhancements of both excited states. These observables concern a single resonant layer only and the OSs are reminiscent of the ones we have seen for the single resonant layer setup, see Fig. 4.1. Opposed to that, Fig. 5.2(a) shows the OS for the coherent and incoherent coupling between the excited states. The OS is found to essentially consist of two circles, one of which is oriented towards positive and another one oriented towards negative values for the incoherent coupling γ_{12}.

To understand the shapes of the OSs, we proceed similarly to Sec. 4.1. We consider the cavity of highest possible incoherent coupling in Fig. 5.2(a), fix the cavity geometry and tune the angle of incidence. This then leads to the black dashed trajectories visible in Fig. 5.2(a), (b) and (c).

To allow for a detailed analysis, we explicitly show the above observables' trajectories as a function of θ in Fig. 5.3(a), (c) and (e). Further, we plot their absolute values in the complex θ plane in Fig. 5.3(b), (d) and (f) to relate the observables of the three-level scheme to their poles as a function of θ. From the analyses in Chapter 3 and 4 we already saw that those poles can be related to the mode structure of the cavity. Since all observables considered in Figs. 5.2 and 5.3 are calculated from different evaluations of the same Green's function (see Appendix A.1.2 for the

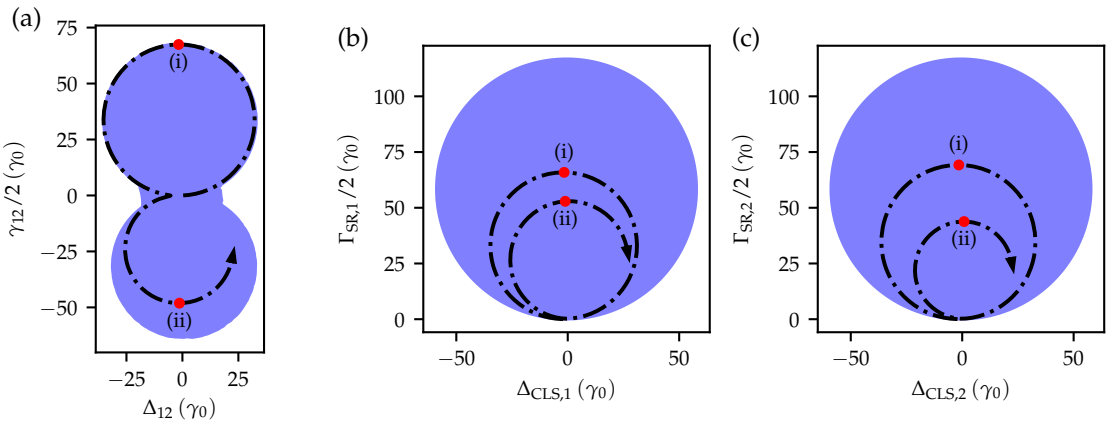

Fig. 5.2: OSs for relevant properties of the three-level system for a Pd/B_4C/^{57}Fe/B_4C/^{57}Fe/B_4C/Pd/Si cavity setup. The blue shaded areas indicate the accessible OSs. Panel (a) shows the coherent Δ_{12} and incoherent γ_{12} coupling between the excited states. Panels (b) and (c) show the OSs of CLS and SR of the first and second excited state, respectively. Note that the panels only resolve the accessible combinations within the pair of observables given in each panel. For example, the figure does not allow to read off, which combinations of Δ_{12} and $\Delta_{\mathrm{CLS},1}$ can be achieved. We will, however, consider further relevant combinations of observables in Sec. 5.3. The black dash-dotted lines represent trajectories that are obtained upon changing the angle of incidence for the specific cavity of highest incoherent coupling, described in Fig. 5.3. The arrow denotes the direction of increasing θ. Red dots on the curves, labeled with lower-case roman numerals, relate the structures in the panels to the poles in Fig. 5.3. Note, that the range of angles used for the trajectories is smaller than in Fig. 5.3, for readability. However, the angular range is the same for all panels of the present plot.

explicit formulae), they share the same poles as a function of θ which is confirmed by Fig. 5.3.

As before, upon passing the first pole [indicated by (i)] on the real θ-axis, an (approximate) circle is traversed for all three observables pairs in Fig. 5.2. This is expected when the single-mode approximation is applicable according to Eqs. (4.2) and (4.3). In contrast to the previous observations in the context of Fig. 4.1(a), however, the couplings traverse a downward oriented circle in Fig. 5.2(a) when passing the second pole (ii). Using the single mode approximation Eq. (4.2), this can be explained by a sign switch for the residues of neighboring poles for the couplings. Eventually, this also explains the why the OS of Fig. 5.2(a) comprises a circle towards positive as well as negative incoherent couplings. Note that in Fig. 5.2(a), one finds a small region of accessible observables in between the two circular structures. This region can be associated to very small angles of incidence.

A particular trait of the trajectory in Fig. 5.2(a) is that it partly runs on the surface of the OS. Therefore, some extremal coupling values are found in a single cavity geometry. This is reminiscent of the behavior of CLS and SR in Fig. 4.1.

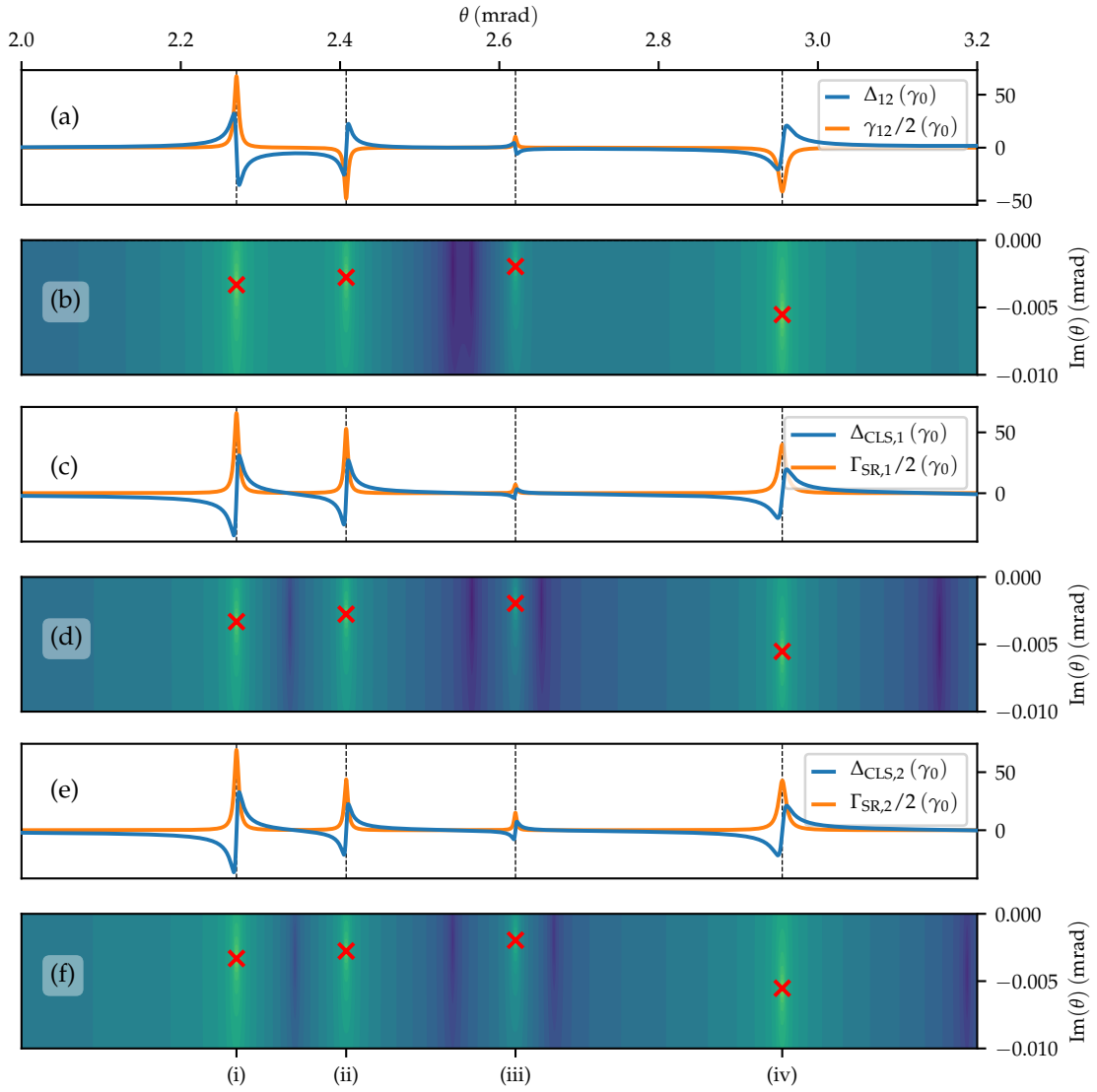

Fig. 5.3: Observables determining the coupling matrix $\boldsymbol{C}$ as a function of the angle of incidence θ for the Pd(105.1 nm)/B_4C(27.7 nm)/^{57}Fe (0.57 nm)/B_4C(23.8 nm)/^{57}Fe (0.57 nm)/B_4C(28.8 nm)/Pd(12.5 nm)/Si cavity setup of highest incoherent coupling in Fig. 5.2(a). Panel (a) shows the coherent Δ_{12} and incoherent γ_{12} coupling between the excited states. Panel (b) shows the absolute value of the couplings in the complex plane. The poles are indicated by red crosses and correspond to the resonant structures in (a). Panels (c, d) and (e, f) are analogous but for the CLS and SR of the respective layer one or two. The black dashed lines in the plots indicate the real parts of the respective poles. The latter are enumerated by roman numerals and relate the poles to the corresponding circular trajectories in Fig. 5.2. We see that all poles coincide which is expected as all shown observables result from different evaluations of the same Green's function.

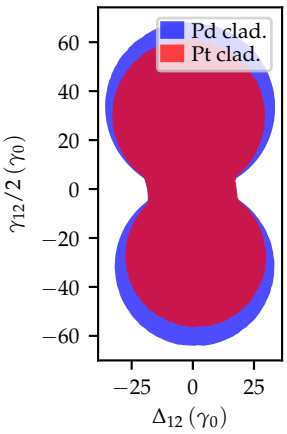

Fig. 5.4: Comparison of OSs for the accessible coherent and incoherent couplings for Pt and Pd as cladding materials in a cladding/B_4C/^{57}Fe/B_4C/^{57}Fe/B_4C/cladding/Si cavity setup. The less absorptive Pd allows for larger tunability than Pt cladding layers, as would be expected from Sec. 4.4.

Since all observables share the same poles, their resonant behavior close to the poles of the Green's function is locked to one another as a function of the angle of incidence. This emphasizes that the observables cannot be tuned independently from each other. To nevertheless exploit the full tuning capabilities, a systematic analysis of the accessible observables, as provided in this thesis, is highly beneficial.

To conclude the discussion of the observables determining the coupling matrix $\boldsymbol{C}$, we can ask whether the guidelines we derived in Sec. 4.4 for the materials choice generalize to more complex systems. To this end, we consider the coherent and incoherent couplings for the cavity of Fig. 5.1(a), but with the cladding layers being made of Pt instead of Pd. The resulting OS is shown in Fig. 5.4 and compared to the corresponding OS for Pd cladding. Here, it is obvious that Pd, which is the less absorptive, $\beta_{\mathrm{Pd}} < \beta_{Pt}$, but also less refractive, $\delta_{\mathrm{Pd}} < \delta_{\mathrm{Pt}}$, outperforms cladding layers made of Pt. This indicates that the significance of low absorption in the cladding layer indeed translates to more complex systems.

5.2.2 Intra-cavity field enhancements

Besides the elements of the coupling matrix $\boldsymbol{C}$, also the Rabi-frequencies Ω_1 and Ω_2 are important for the level scheme. For the cavity used in Fig. 5.3, these driving fields are negligible as the thick top cladding layer effectively prevents any outside field from entering the cavity. The Rabi-frequencies Ω_1 and Ω_2 enter the reflection spectrum in the form of their Fourier transforms with respect to time. In turn, the latter are proportional to the field strength at the respective layer, $E_{\mathrm{in}}(z_l, \boldsymbol{k}_{\parallel}, \omega_{\mathrm{nuc}})$. To arrive at a comprehensive description of the three-level scheme observables, we therefore subsequently determine the OSs of accessible field strengths, $E_{\mathrm{in}}(z_1, \boldsymbol{k}_{\parallel}, \omega_{\mathrm{nuc}})$ and $E_{\mathrm{in}}(z_2, \boldsymbol{k}_{\parallel}, \omega_{\mathrm{nuc}})$, at the resonant layers. In contrast to Sec. 4.3, we do not consider the intensity of the driving fields, but show their accessible real and imaginary parts. This helps to illustrate similarities of the field enhancements' behaviors to the

remaining level scheme properties. First, we consider the accessible OSs for the field enhancements. Subsequently, we again specialize to one cavity geometry and tune the angle of incidence to explain the structure of the OSs found on the basis of the poles of the field enhancements.

The resulting OSs for the field enhancements are shown in Fig. 5.5(a) and (b). The OS for the real and imaginary field enhancement in the first resonant layer is found similar, but not identical, to the one in the second resonant layer. Overall, both OSs have some reminiscence of the OS for the coherent and incoherent couplings in Fig. 5.2(a).

For the cavity of highest real field enhancement at the first nuclear layer, we again fix the geometry and tune the angle of incidence. The resulting trajectories are plotted in Fig. 5.5(a) and (b) as black lines. The right hand side of Fig. 5.5 further shows the resulting field enhancements as a function of the angle of incidence. Since the field strengths have not been analyzed in Fig. 5.3, we also show their pole structures in Fig. 5.5(d) and (f).

Clearly, the poles, and thus the resonant behavior, coincide for both driving field enhancements. In fact, it can also be shown that for a specific cavity structure, the poles of the field enhancements are the same as for the observables considered in Figs. 5.2 and 5.3 (not shown explicitly here). This is a result of the common underlying mode structure of the cavity and can in principle also be understood from the explicit formulae, see Appendix A.1.2.

From Fig. 5.5(a) and (b) it is apparent that also the field strengths traverse circular trajectories when θ passes by a respective pole, indicated by (i) or (ii). However, as compared to Fig. 5.2, the circles are found to be more freely rotated in the complex plane. This can be attributed to the fact that the residues of the field enhancement can be complex-valued, thus allowing for different orientations of the single-mode circles, cf. Sec. 4.1. As a consequence, this explains that the accessible OSs obey different symmetries as compared to those found for the remaining observables of the level scheme.

This comprises the fundamental discussion of OSs for relevant properties of the three-level scheme. The determination is achieved much in the same way as it was for the two-level schemes, such that the inverse design is applied successfully also for systems with two resonant layers. Due to the higher number of level-scheme properties involved, not all relations between relevant observables were explicitly given. Using the formalism of Chapter 6, however, the OSs of arbitrary observable combinations can be readily calculated.

In the following, we extend the discussion to ratios of three-level scheme observables, e.g. $\Delta_{12}/(\Gamma_{\mathrm{SR},1} + \gamma_0)$. Such ratios are of relevance as the timescale of the dynamics in the three-level system is set by the decay rates of the excited states. We thus need to know the relative size of the observables to assess which quantum optical effects can be realized.

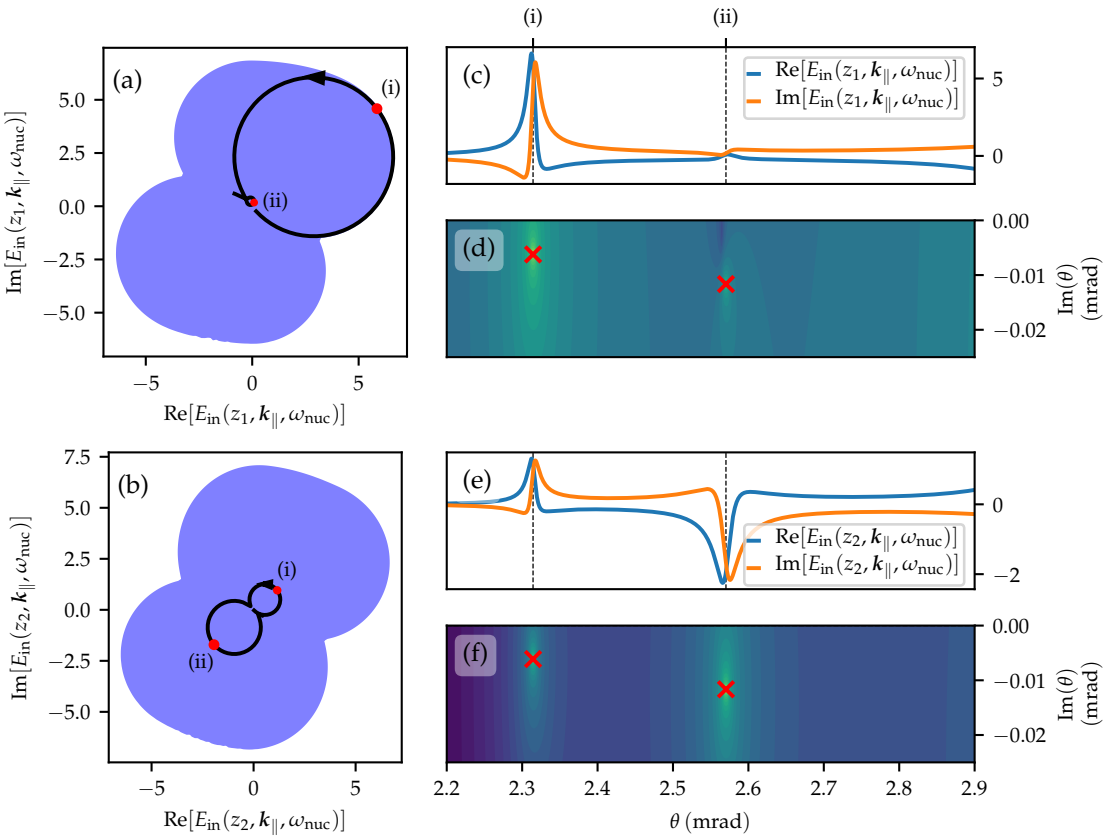

Fig. 5.5: OSs for the field enhancements at the resonant layers. The blue shaded areas in (a) and (b) show the accessible real and imaginary parts of the field strength at the first and second nuclear layer for Pd/B_4C/^{57}Fe/B_4C/^{57}Fe/B_4C/Pd/Si cavity setups, respectively. The black lines in (a) and (b) correspond to the trajectories traversed upon tuning the angle of incidence θ for the Pd(3.7 nm)/B_4C(27.6 nm)/^{57}Fe (0.57 nm)/B_4C(28.0 nm)/^{57}Fe (0.57 nm)/B_4C(0 nm)/Pd(19.9 nm)/Si cavity of highest real part field enhancement in the first resonant layer. Here, the arrows indicate increasing θ. For this cavity, the explicit dependency of the field enhancement in the first resonant layer on θ is shown in panel (c) and its absolute value in the complex θ plane plotted in panel (d). Here, the poles are indicated in red. Likewise, panel (e) and (f) show the analogous plots for the second resonant layer. The black dashed lines in the right hand side plots indicate the real part of the poles which are common for all quantities shown. Lastly, the red dots with annotated roman numerals link the circular structures in (a) and (b) to the poles on the right hand side of the figure. The trajectories with the angle of incidence are reminiscent of the ones in Fig. 5.2. Together with the common pole structure of all observables, this emphasizes the intertwined dependencies of the observables on some cavity parameters.

5.3 Designing three-level scheme parameter ratios

In the previous section, we discussed the relevant properties of the three-level system. In this context, we have seen that the different observables determining the effective level scheme cannot be chosen independently from one another. From a quantum optical perspective, however, the qualitative nature of the dynamics is not governed by the properties of the level scheme only, but also their relative size is of importance. Particularly, the decay times set the relevant timescales of the dynamics. In order to design quantum optical setups, it is therefore useful to consider the three-level scheme's properties scaled by the decay times in the system. In this section, we illustrate that the inverse design is applicable to such ratios of three-level scheme properties. In the introduction, we motivated that the cavity-mediated coupling between the excited states can take the role of a coherent driving field and thus compensate for the unavailability of suitable lasers at x-ray energies. The couplings are thus of great significance to the design of advanced quantum optical schemes and will be in the focus of this section.

Since the effective level scheme comprises two excited states $|\mathrm{E}_{1,2}\rangle$, which can set the relevant timescale, we will in the following start the discussion by considering the coherent and incoherent couplings scaled by the first, $\Gamma_{\mathrm{SR},1} + \gamma_0$, and second, $\Gamma_{\mathrm{SR},2} + \gamma_0$, excited state decay rate. Subsequently we will complement the results by adding the remaining decay rate as a third observable.

5.3.1 Scaled coherent and incoherent couplings

For the coherent and incoherent couplings scaled by the first and second decay rate, we show the OSs as blue shaded areas in Fig. 5.6(a) and (b), respectively.

Allowing for arbitrarily thick top cladding layers, we find the OSs to exhibit a roughly circular shape. Moreover, the two OSs are found to be very similar. In principle, the two resonant layers are embedded in different photonic environments as the upper layer is closer to the top surface, i.e., vacuum, while the lower layer is closer to the Si-substrate, see Fig. 5.1(a). Generally, the OSs for the scaled couplings should therefore be expected to be different depending on which decay rate is used for scaling. Since many of the outermost observables are, however, realized for very thick cladding layers, the absorption within these claddings suppresses the asymmetry such that both OSs are similar nevertheless.

In the context of the visibility in Sec. 4.2, we already noted that for thick cladding layers, the in- and out-coupling vanishes. In order to ensure non-zero in- and out-coupling of the fields, we subsequently restrict the top cladding layer to thicknesses of 3 nm, 2 nm, 1 nm as well as no cladding layer at all, and compute the OSs under these constraints. The results are shown by the differently colored areas in Fig. 5.6. Generally, introducing stronger constraints reduces the tunability of the achievable

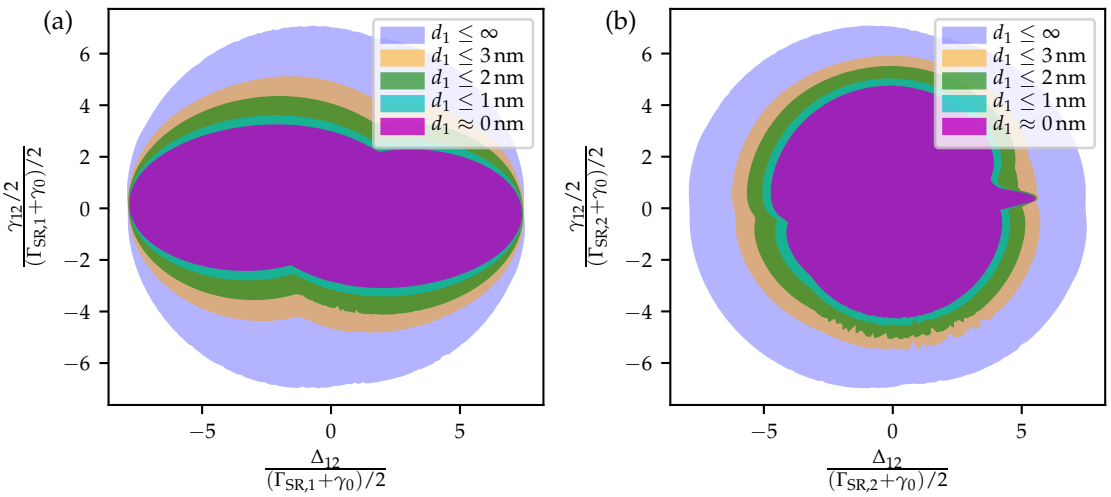

Fig. 5.6: Accessible OSs for the excited states' coherent and incoherent couplings scaled by decay rate of the first (a) and second (b) excited state. To ensure the in-coupling of the driving field and the out-coupling of the nuclear signal, different maximal thicknesses for the top cladding layer d_1 (see Fig. 5.1(a)) were allowed for. Observables were calculated in a Pd/B_4C/^{57}Fe/B_4C/^{57}Fe/B_4C/Pd/Si cavity setup.

scaled coupling strength. As these constraints restrict the cladding layer thickness, the changes to the OSs in Fig. 5.6(a) and (b) are further asymmetric.

Interestingly, in Fig. 5.6(a) we find that large absolute values of the scaled coherent coupling Δ_{12} can be realized with cavities without upper cladding layer. Similarly, on the right hand side of the OSs in Fig. 5.6(b), one can see that a peculiar tip is visible. The tip emerges when the top cladding layer is restricted to thicknesses below 2 nm, but doesn't change upon further restriction of this thickness (the green and cyan areas vanish behind the purple one). Consequently, also for this OS comparatively large scaled coherent couplings are obtained for non-cladded cavities. The insight that such cavities can form relevant and interesting settings can therefore be translated from the single resonant layer systems in Chapter 4 to encompass more complex thin-film cavities.

5.3.2 Scaled couplings and decay rate ratios

So far, we considered the coupling between both excited states scaled by each of the decay rates independently. Yet, also the interplay between both decay rates together with the coupling strength is of importance to the design of quantum optical effects (e.g., see the following section). Hence, we add the remaining excited state decay rate as a third observable. We scale this remaining decay rate with the decay rate that also scales the coherent and incoherent coupling and calculate the respective OSs for the three scaled observables, see Fig. 5.7.

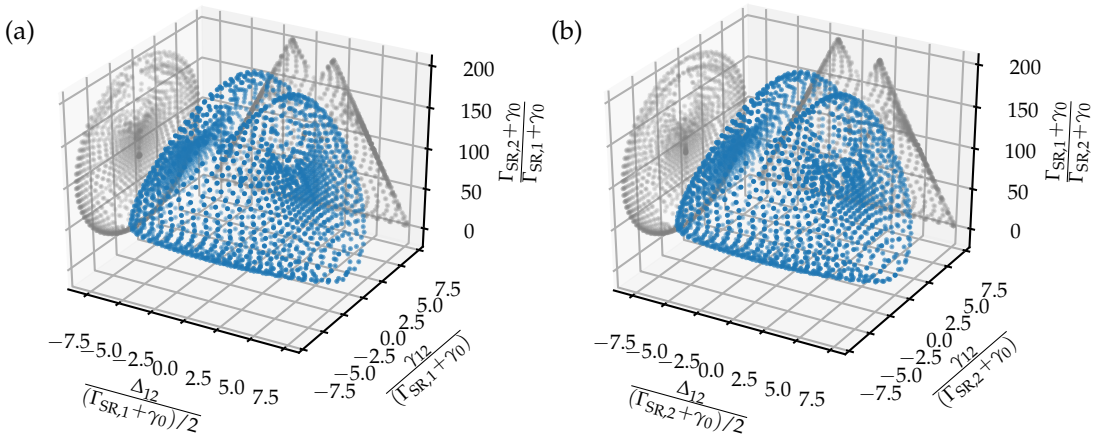

Fig. 5.7: Accessible OSs for the scaled excited state coherent and incoherent couplings combined with a scaled excited state decay rate. All quantities are scaled by the decay rate of the first (a) and second (b) excited state. The third axis represents the decay rate that is not used for scaling. The OSs were calculated for a Pd/B_4C/^{57}Fe/B_4C/^{57}Fe/B_4C/Pd/Si cavity setup. As the topology of the surfaces of the OSs (a) and (b) is complex, we only give the surface points calculated with the methods of Chapter 6, rather than trying to plot an explicit surface. We support the readability by projecting the points to the axes planes.

Fig. 5.7(a) shows the surface of the OS for the coherent and incoherent coupling scaled by the first excited state decay rate as well as the ratio of the second and first excited state decay rates. Likewise, Fig. 5.7(b) shows the same OS, but for the roles of first and second excited state exchanged.

Since each observable chosen for the calculation is a ratio of three-level scheme observables, the respective OSs turn out not to be smooth surfaces, but show more complex topology in certain regions. We therefore restrict ourselves to plotting the surface points calculated and omit the interpolation by a smooth surface. For clarity, the projections to the axes planes are indicated. For the projection to the bottom see Fig. 5.6.

Overall, Fig. 5.7(a) and (b) show that a large set of observables combinations is accessible for the design. As previously, the two surfaces are found to be very similar for the reason that we did not restrict the top cladding layer thickness. However, this again has to be considered a problem for the driving and the observation of the artificial three-level scheme.

Considering the same observables as in Fig. 5.7, we thus restrict the top cladding layer thickness to 3 nm and consider the OS surfaces accessible under this constraint in Fig. 5.8. As was already noticed for the two-dimensional version of the plots, see Fig. 5.6, the restriction of the top cladding layer thickness leads to different OSs upon exchanging the roles of the excited states. Analogously to Fig. 5.7, we only plot surface points and their projections to the axes planes.

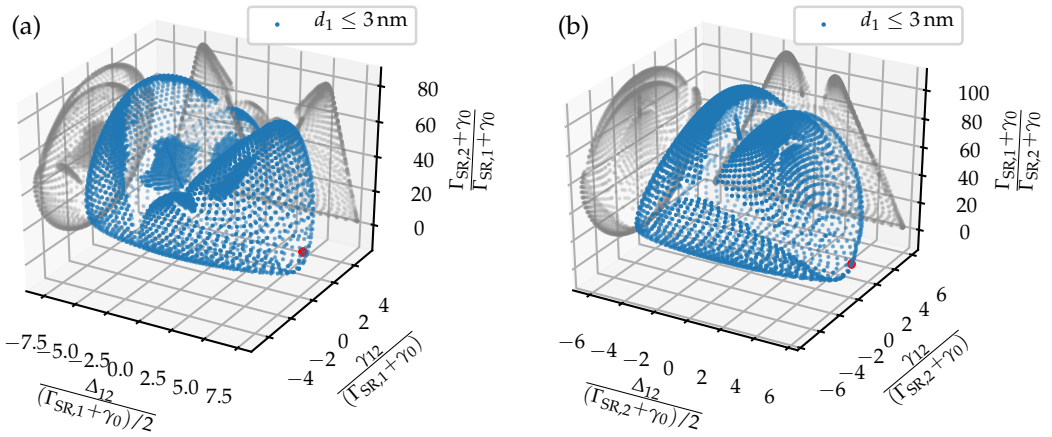

Fig. 5.8: Accessible OSs analogous to Fig. 5.7 but for the top cladding layer bounded by $d_1 \leq 3\,\mathrm{nm}$. In panel (a) and (b), the cavities used for Fig. 5.10(a) and (b) are indicated by red dots, respectively. We only plot surface points analogously to Fig. 5.7.

OSs as considered in Fig. 5.8 provide the basis of the design of nuclear quantum optical effects that rely on the coherent and incoherent coupling between the excited states of the three-level scheme. This section showed, that we can determine such OSs for ratios of three-level scheme parameters. With the example of an EIT scheme, the following section will illustrate how we can use the OSs of Fig. 5.8 to design nuclear quantum optical schemes.

5.4 Electromagnetically induced transparency

In this section, we illustrate the inverse design of quantum optical effects using the example of EIT. An EIT-like effect has been observed in [51] in the context of nuclear quantum optics. However, we will focus on the design of EIT dynamics in the level scheme in Fig. 5.1(b) and only at the end of this section comment on the relation to [51].

In the following, we first briefly revisit the basic concept of EIT, as would be realized, e.g., with atomic systems, to provide a guideline for the design of EIT. We subsequently engineer nuclear EIT schemes using the artificial three-level system described at the beginning of this chapter. Finally, we comment on open questions concerning the interpretation of the EIT effect as well as the role of the incoherent coupling between the excited states.

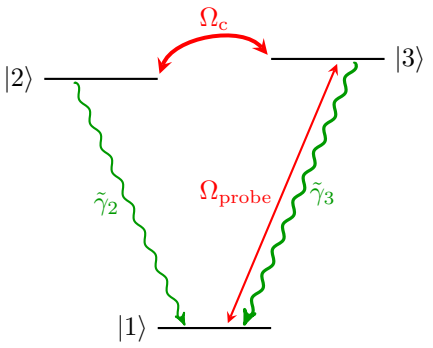

Fig. 5.9: Schematic representation of a setup suitable to the observation of EIT [51]. The two upper levels are coupled by a strong laser control field Ω_c. While the state $|2\rangle$ is metastable and decays with comparatively small rate $\tilde{\gamma}_2$, excited state $|3\rangle$ exhibits a larger decay rate $\tilde{\gamma}_3$ to the ground state $|1\rangle$. Upon weakly probing the $|1\rangle \leftrightarrow |3\rangle$ transition with laser field Ω_{probe}, the EIT effect can be expected subject to the condition Eq. (5.11).

5.4.1 EIT in atomic systems

As an archetypal quantum optical scheme, EIT was first realized with transitions in Sr atoms [63]. For the implementation of EIT, a three-level system of the type considered in Fig. 5.9 can be used [51]. Following general arguments in [51], we briefly revisit requirements for such a scheme as operated with standard lasers, e.g., at visible frequencies. To observe the EIT-effect in this level scheme, it is necessary that one of the excited states, say $|2\rangle$, is (meta)stable, i.e. $\tilde{\gamma}_2$ is small. At the same time, a strong control laser field Ω_c couples the two excited states $|2\rangle$ and $|3\rangle$. Upon weakly probing the transition from $|1\rangle$ to $|3\rangle$ with a probe laser Ω_{probe} of detuning Δ from the transition frequency, the systems shows transparency around $\Delta \approx 0$, that is Ω_{probe} is barely absorbed. However, for the effect to be prominent in the presence of non-zero decay $\tilde{\gamma}_2$, the inequality

$$\tilde{\gamma}_3^2 > |\Omega_c|^2 > \tilde{\gamma}_3\tilde{\gamma}_2 \tag{5.11}$$

has to be fulfilled [51]. While we described the operation of EIT in terms of lasers, the level scheme in Fig. 5.9 can in fact be realized by the artificial nuclear three-level scheme in Fig. 5.1(b) if one of the driving fields, Ω_1 or Ω_2, as well as the incoherent coupling γ_{12} are small. For that case, the coherent coupling Δ_{12} between the excited states takes the role of the laser, $\Omega_c = \Delta_{12}$. In the following section, we want to tune the artificial level scheme to fulfill these conditions. To that end, we rewrite the EIT condition, Eq. (5.11), as

$$\frac{\tilde{\gamma}_3^2}{\tilde{\gamma}_2^2} > \frac{|\Omega_c|^2}{\tilde{\gamma}_2^2} > \frac{\tilde{\gamma}_3}{\tilde{\gamma}_2}\,. \tag{5.12}$$

Using this form, the observables we considered in Fig. 5.8 directly correspond to the quantities in the inequality. At the same time, Fig. 5.8 provides the means to ensure small incoherent coupling. Note that we will additionally consider the magnitude of the driving fields when selecting suitable cavities from Fig. 5.8. Thus, on the basis of the level scheme parameter ratios of Sec. 5.3, we will in the following choose cavities in accordance with the above conditions to design EIT dynamics in the nuclear setup.

$\frac{\Gamma_{\mathrm{SR},1}}{2}\,(\gamma_0)$	$\frac{\Gamma_{\mathrm{SR},2}}{2}\,(\gamma_0)$	$\Delta_{12}+i\frac{\gamma_{12}}{2}\,(\gamma_0)$	$\left\lvert\frac{\Omega_2(\omega_{\mathrm{nuc}})}{\Omega_1(\omega_{\mathrm{nuc}})}\right\rvert^2$	$\frac{\tilde{\gamma}_3^2}{\tilde{\gamma}_2^2}$	$\frac{\lvert\Omega_{\mathrm{c}}\rvert^2}{\tilde{\gamma}_2^2}$	$\frac{\tilde{\gamma}_3}{\tilde{\gamma}_2}$
0.38	6.2	$6.4+0.52i$	279	58	13	7.6

Tab. 5.1: Level scheme properties corresponding to the Pd(1.5 nm)/B_4C(49.8 nm)/^{57}Fe (0.57 nm)/B_4C(97.1 nm)/^{57}Fe (0.57 nm)/B_4C(35.4 nm)/Pd(43.7 nm)/Si cavity illuminated at 2.28 mrad. The corresponding cavity is indicated in red in Fig. 5.8(a) and the reflection spectrum plotted in Fig. 5.10(a). The left part of the table shows the quantities determining the effective three-level scheme. $|\Omega_2(\omega_{\mathrm{nuc}})/\Omega_1(\omega_{\mathrm{nuc}})|^2$ is the ratio of frequency-space Rabi-frequencies probing the second and first excited state, i.e., here, only the second excited state is probed. The right part of the table contains the relevant ratios according to Eq. (5.13) that allow one to verify that Eq. (5.12) is indeed fulfilled. We further set $\Omega_c = \Delta_{12}$, however, noting that also the inclusion of the incoherent coupling does not lead to a violation of the EIT inequality due to its comparatively small size.

5.4.2 Designing EIT in a nuclear three-level scheme

In order to design EIT dynamics, we have to tune the artificial three-level system to comply with the EIT condition, Eq. (5.12). Since in principle both excited states in the artificial scheme Fig. 5.1(b) can take equivalent roles, we have to decide which of the excited states $|\mathrm{E}_{1,2}\rangle$ should take the role of the metastable state $|2\rangle$ in Fig. 5.9. In the following, we first consider the first excited state, $|\mathrm{E}_1\rangle$, and, subsequently, the second excited state, $|\mathrm{E}_2\rangle$, as the metastable state $|2\rangle$.

Deciding to design $|E_1\rangle$ metastable, we adopt the convention

$$\tilde{\gamma}_2 \equiv \Gamma_{\mathrm{SR},1} + \gamma_0\,, \quad \text{and} \quad \tilde{\gamma}_3 \equiv \Gamma_{\mathrm{SR},2} + \gamma_0\,, \tag{5.13}$$

according to the general treatment of the previous Sec. 5.4.1. To fulfill the EIT requirement of Eq. (5.12), it is sensible to consider the surface points of Fig. 5.8(a). On the basis of this OS, we can firstly restrict to the part of the surface where the scaled incoherent coupling $\gamma_{12}/(\Gamma_{\mathrm{SR},1}+\gamma_0)$ is small. Secondly, within the range of small incoherent coupling, we can select a cavity with a decay rate ratio, $\tilde{\gamma}_3/\tilde{\gamma}_2 = (\Gamma_{\mathrm{SR},2}+\gamma_0)/(\Gamma_{\mathrm{SR},1}+\gamma_0)$, and a coherent scaled coupling strength, $\Omega_{\mathrm{c}}/\tilde{\gamma}_2 = \Delta_{12}/(\Gamma_{\mathrm{SR},1}+\gamma_0)$, such that it complies with the EIT condition, Eq. (5.12). This is possible because we can essentially change the ratio of these two quantities continuously when moving on the surface of the OS in Fig. 5.8(a).

In Fig. 5.8(a), the cavity that is selected this way is indicated by a red dot. Tab. 5.1 gives the properties of the corresponding level scheme (left part). Further, relevant ratios (right part) of the properties in the convention for $\tilde{\gamma}_2$ and $\tilde{\gamma}_3$ adopted in Eq. (5.13) are given. Using these ratios, it is apparent that the EIT condition, Eq. (5.12), is fulfilled. Furthermore, the field probing the first excited state is suppressed by a factor of more than 200. Thus, the generic level scheme of Fig. 5.9 is indeed realized within the nuclear platform in good approximation.

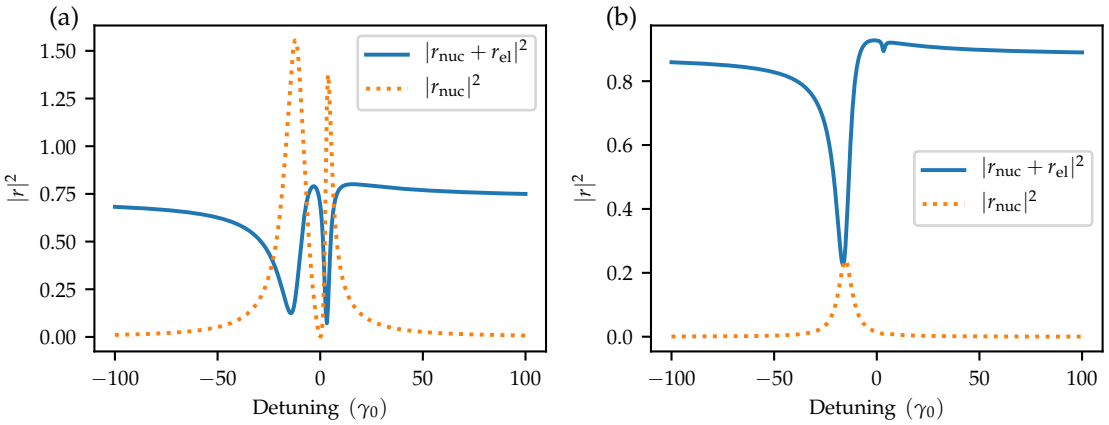

Fig. 5.10: Reflection spectrum for two cavities with nuclear EIT dynamics. In (a) the reflection spectrum $|r|^2 = |r_{\mathrm{nuc}} + r_{\mathrm{el}}|^2$ and its nuclear contribution $|r_{\mathrm{nuc}}|^2$ are shown as a function of the detuning from the bare nuclear transition frequency ω_{nuc} for the cavity of Tab. 5.1. The corresponding cavity is indicated in red in Fig. 5.8(a). Panel (b) shows the spectrum for the role of the excited state decay rates exchanged. The corresponding cavity structure is given in Tab. 5.2 and marked in Fig. 5.8(b). Although an EIT dynamics was designed in (a) and (b), only panel (a) shows the characteristic dip. This discrepancy will be explained in Sec. 5.5.1.

Fig. 5.10(a) shows the resulting spectrum for this cavity as a function of the detuning from the bare nuclear transition frequency ω_{nuc}. Since the cavity is not critically coupled to the impinging x-rays, the spectrum additionally comprises a contribution by the electronic background. Subtracting this contribution, a typical double-peak structure reminiscent of the EIT spectrum is visible. This shows that we can indeed design three-level schemes to exhibit relevant quantum optical effects.

Likewise, we can exchange the roles of the states $|\mathrm{E}_1\rangle$ and $|\mathrm{E}_2\rangle$, that is we consider $|\mathrm{E}_2\rangle$ the metastable state in the level scheme in Fig. 5.9. Consequently, we adopt the convention

$$\tilde{\gamma}_2 \equiv \Gamma_{\mathrm{SR},2} + \gamma_0\,, \quad \text{and} \quad \tilde{\gamma}_3 \equiv \Gamma_{\mathrm{SR},1} + \gamma_0\,. \tag{5.14}$$

With the role of the excited states exchanged, we must now consider the OS in Fig. 5.8(b). On that basis, we proceed analogously to the previous part and eventually select the cavity marked by a red dot in Fig. 5.8(b). The corresponding level scheme properties are given in Tab. 5.2, and again represented according to the convention of Eq. (5.14) on the right hand side of the table. Even though less pronounced than for the previous cavity, this setting also satisfies the EIT condition, Eq. (5.12). Together with the suppression of the electric field probing the second excited state by a factor of about four, the resulting artificial level scheme can be considered an acceptable approximation of the level scheme in Fig. 5.9.

The reflection spectrum for this setup is shown in Fig. 5.10(b). For the present cavity, however, the reflection spectrum is found to be only a Fano-lineshape with a

$\frac{\Gamma_{\mathrm{SR},1}}{2}\,(\gamma_0)$	$\frac{\Gamma_{\mathrm{SR},2}}{2}\,(\gamma_0)$	$\Delta_{12}+i\frac{\gamma_{12}}{2}\,(\gamma_0)$	$\left\lvert\frac{\Omega_1(\omega_{\mathrm{nuc}})}{\Omega_2(\omega_{\mathrm{nuc}})}\right\rvert^2$	$\frac{\tilde{\gamma}_3^2}{\tilde{\gamma}_2^2}$	$\frac{\lvert\Omega_{\mathrm{c}}\rvert^2}{\tilde{\gamma}_2^2}$	$\frac{\tilde{\gamma}_3}{\tilde{\gamma}_2}$
3.2	0.63	$6.2+1.1i$	4.4	10	7.6	3.2

Tab. 5.2: The table is analogous to Tab. 5.1, but for the Pd(3.0 nm)/B_4C(42.5 nm)/^{57}Fe (0.57 nm)/B_4C(143.4 nm)/^{57}Fe (0.57 nm)/B_4C(72.9 nm)/Pd(43.4 nm)/Si cavity illuminated at an angle of 2.23 mrad, that is indicated in red in Fig. 5.8(b). The resulting reflection spectrum is shown in Fig. 5.10(b). For this setup, mainly the first excited state is probed. The conventions for the right part of the table are according to Eq. (5.14). We see that Eq. (5.12) is indeed fulfilled, even though not as pronounced as for Tab. 5.1.

small variation. In particular, the nuclear contribution (orange dashed line) essentially shows no EIT signature even though we designed the level scheme according to the criterion Eq. (5.12). Considering that an EIT feature was visible in Fig. 5.10(a), this seems surprising.

However, comparing our implementation of the EIT dynamics to generic setups, e.g. using clouds of atoms, different observables are accessible experimentally. While the latter can be characterized by a transmission measurement, the standard observable for the artificial level schemes is the reflection spectrum. Since both observables are fundamentally different, the observability of the EIT signature can in general not be expected.

This feature thus shows some analogy to the design of artificial two-level schemes in Chapter 4, where the additional visibility criterion was needed to ensure observability. In Sec. 5.5.1, we will give a clear explanation for the vanishing EIT-dip in Fig. 5.10(b) on the basis of out-coupling effects.

Finally, we note that similar observations regarding the observability of an EIT-like spectrum were made in the experiment [51]. However, different conclusions were drawn based on a different interpretation of the nuclear quantum optical effects. In the following, we therefore briefly comment on these differences and also shortly touch on a related question regarding the incoherent coupling term in the level scheme in Fig. 5.1(b).

5.4.3 Some open questions in nuclear EIT

Interpretation of nuclear EIT

The fact that additional constraints are present for the observability of EIT-signatures was already noticed by Röhlsberger et al. when performing the experiment in [51]. Here, the EIT effect was designed on the basis of the field distribution in the cavity resulting from the incident x-rays. It was seen that only when the upper resonant layer is placed in a field node and the lower one in an anti-node, an EIT-like dip becomes visible in the reflection spectrum. Upon exchanging the role of the resonant layers, the EIT-like dip vanishes which is consistent with our observations in Fig. 5.10 (see

also the driving field ratios in Tabs. 5.1 and 5.2). Röhlsberger et al. interpreted the EIT effect phenomenologically on the basis of the semiclassical layer formalism [46]. They showed that the amplitude reflected from the thin-film cavity essentially has the same form as the linear EIT susceptibility. The parameters of the level scheme can then be read off by equating coefficients. In this interpretation, the reason for the vanishing EIT-dip is that the coupling between the excited states vanishes.

Opposed to this, in the present framework of the ab initio theory [48], the description of the internal dynamics of the nuclei as an artificial three-level scheme is the focus. From this perspective, the two setups of Fig. 5.10(a) and (b) are analogous in the interpretation of their internal dynamics, i.e. the coupling between the excited states is non-zero also for the case of Fig. 5.10(b). The lack of the EIT-dip must then be associated to the out-coupling step as will be explained in detail in Sec. 5.5.1.

The difference in the interpretations further becomes apparent when considering that for the case of Fig. 5.10(a), the EIT-like feature was only apparent in the nuclear contribution to the spectrum. For the full reflection spectrum, the nuclear response additionally interferes with the electronic background and eventually does not directly show the archetypal EIT structure as a result. For the internal nuclear dynamics, however, the electronic background is of little relevance. Conversely, the EIT-like spectra in [51] show small electronic background and thus indeed exhibit the archetypal EIT-dip.

In view of the different interpretations, we note that both approaches essentially provide interpretations of the linear reflection spectrum of nuclei in the cavity, and it is not immediately clear under which conditions the interpretation as EIT is applicable, as was already discussed in different contexts [95]. While the interpretation based on the layer formalism is, however, purely phenomenological, the description as quantum few-level scheme, used in the present thesis, is on an ab initio basis [48] and therefore on a more fundamental level. To translate EIT-based applications (see [62] and references therein) to the x-ray regime, a fundamental understanding of the effect will be necessary in the future.

Incoherent coupling in the ab initio theory

Related to the interpretation of nuclear EIT, also the role of the incoherent coupling on EIT-like signatures remains to be understood in the framework of the ab initio theory [48]. Designing the EIT scheme, we explicitly kept this contribution small to comply with the level scheme of Fig. 5.9. Nevertheless, it enters the description as an additional tunable parameter. In that respect, Fig. 5.11 shows an example of a reflection spectrum for another cavity on the surface of the OS in Fig. 5.8(a). As indicated in Tab. 5.3, this cavity comes with incoherent and coherent coupling strength on the same scale and does not obey the EIT criterion Eq. (5.12). At the same time, however, it shows a pronounced EIT-like dip, both in the nuclear contribution to the reflection spectrum as well as in the overall reflection spectrum.

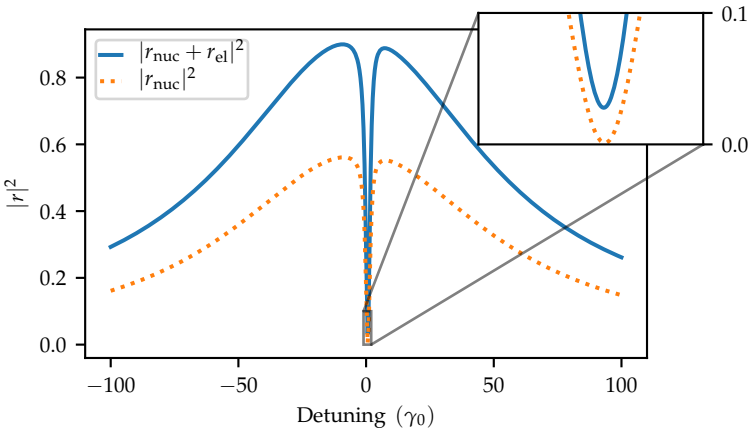

Fig. 5.11: Reflection spectrum as a function of the detuning from the bare nuclear transition frequency ω_{nuc} for a Pd(3.0 nm)/B_4C(72.9 nm)/^{57}Fe (0.57 nm)/B_4C(46.9 nm)/^{57}Fe (0.57 nm)/B_4C(47.9 nm)/Pd(87.7 nm)/Si cavity illuminated at 2.24 mrad. The level scheme parameters are given in Tab. 5.3. Both, the full spectrum (blue) as well as the nuclear contribution (orange) show a pronounced EIT-like dip. At the same time, the ab initio theory [48] associates a comparatively large incoherent coupling to the underlying three-level scheme. The role of this incoherent coupling and its effect on EIT signatures remains to be understood in detail in future works.

$\frac{\Gamma_{\mathrm{SR},1}}{2}\,(\gamma_0)$	$\frac{\Gamma_{\mathrm{SR},2}}{2}\,(\gamma_0)$	$\Delta_{12} + i\frac{\gamma_{12}}{2}\,(\gamma_0)$	$\left\lvert\frac{\Omega_2(\omega_{\mathrm{nuc}})}{\Omega_1(\omega_{\mathrm{nuc}})}\right\rvert^2$	$\frac{\tilde{\gamma}_3^2}{\tilde{\gamma}_2^2}$	$\frac{\lvert\Delta_{12}\rvert^2}{\tilde{\gamma}_2^2}$	$\frac{\lvert\gamma_{12}\rvert^2}{\tilde{\gamma}_2^2}$	$\frac{\tilde{\gamma}_3}{\tilde{\gamma}_2}$
0.67	60	$-4.2 - 4.8i$	92	2641	3.3	4.3	51

Tab. 5.3: Level scheme parameters for the cavity used in Fig. 5.11. Quantities shown are analogous to Tab. 5.1 but both, the coherent as well as the incoherent coupling are given as scaled by the decay rate $\tilde{\gamma}_2$. Note, that the convention relating to the three-level scheme of Fig. 5.9 is $\tilde{\gamma}_2 = \Gamma_{\mathrm{SR},1} + \gamma_0$ and $\tilde{\gamma}_3 = \Gamma_{\mathrm{SR},2} + \gamma_0$.

It particularly resembles the EIT-like setups shown in [51] for the nuclear setting, but also generic EIT-signatures [62]. This emphasizes that it is not clear which spectral signatures can be considered as witnesses for EIT in the nuclear platform.

In the following, we put aside the open questions regarding EIT and consider a different approach to, first, understand the suppression of the nuclear response in certain cases, and, second, overcome the accompanying restrictions by granting direct access to the nuclear imprint on the reflection spectrum. The approach is based on the reflection spectrum calculated from the ab initio theory [48] and can be used to directly design this observable. Hence, to some extent it also overcomes the uncertainties regarding the interpretation of the spectrum.

5.5 Nuclear excitonic normal modes

Due to the off-diagonal elements occurring in Eq. (5.8), and, hence, in Eq. (5.9), the excitons in the two resonant layers are coupled to each other. From the linear reflection spectrum according to Eq. (5.9), the influence of the quantum optical properties is unintuitive, since the different terms in the matrix contractions feature a complex interplay to produce the final dependence on frequency. To get a better handle, we can diagonalize the matrix $\mathcal{M}^{-1}(\omega)$, i.e. we can determine the normal frequencies and modes of the two coupled nuclear excitons. In order to bring $\mathcal{M}^{-1}(\omega)$ to diagonal form, we first diagonalize the coupling matrix $\boldsymbol{C}$, i.e. we find the matrix $\boldsymbol{S}$ such that $\boldsymbol{S}^{-1}\boldsymbol{C}\boldsymbol{S}$ is of diagonal form. Then it directly follows that

$$\begin{aligned}\boldsymbol{S}^{-1}\mathcal{M}^{-1}(\omega)\boldsymbol{S} &= -i\boldsymbol{S}^{-1}\left[(\omega-\omega_{\mathrm{nuc}}+i\frac{\gamma_0}{2})\mathbb{1}+\boldsymbol{C}\right]^{-1}\boldsymbol{S} = \\ &= -i\left[(\omega-\omega_{\mathrm{nuc}}+i\frac{\gamma_0}{2})\mathbb{1}+\boldsymbol{S}^{-1}\boldsymbol{C}\boldsymbol{S}\right]^{-1}, \end{aligned} \tag{5.15}$$

that is also the matrix $\boldsymbol{S}^{-1}\mathcal{M}^{-1}(\omega)\boldsymbol{S}$ is diagonal. Note that since $\boldsymbol{C}$ does not depend on the frequency, the transformation matrix $\boldsymbol{S}$ is independent of frequency as well. Hence, we can rewrite Eq. (5.9) with the in- and out-coupling vectors transformed to the diagonal basis,

$$\begin{aligned} r(\omega) &= r_{\mathrm{el}} - \mu_0\omega_{\mathrm{nuc}}^2\left(\tilde{\boldsymbol{G}}\boldsymbol{S}\right)\left(\boldsymbol{S}^{-1}\boldsymbol{\mathcal{M}}^{-1}(\omega)\boldsymbol{S}\right)\left(\boldsymbol{S}^{-1}\tilde{\boldsymbol{\Omega}}\right) = \\ &= r_{\mathrm{el}} + \sum_{n=1,2}\frac{ig_n}{\omega-\omega_{\mathrm{nuc}}+i\frac{\gamma_0}{2}+\lambda_n}, \end{aligned} \tag{5.16}$$

where $g_n = \mu_0\omega_{\mathrm{nuc}}^2(\tilde{\boldsymbol{G}}\boldsymbol{S})_n(\boldsymbol{S}^{-1}\tilde{\boldsymbol{\Omega}})_n$ denotes the product of the nth entries of the transformed in- and out-coupling vectors. In this expression, $\lambda_{1,2}$ are the two eigenvalues of the coupling matrix $\boldsymbol{C}$. The frequency dependency is fully encoded in the denominator which is why the nuclear contribution is given by two Lorentzians of modified linewidth and position. The frequency shift and decay enhancement of the excitonic normal modes is then directly accessible by the (negative) real and (positive) imaginary part of the eigenvalues, respectively. The eigenvalues of the coupling matrix are in turn calculated to be

$$\begin{aligned}\lambda_{1,2} =& \frac{-(\Delta_{\mathrm{CLS},1}+\Delta_{\mathrm{CLS},2})}{2}+i\frac{\Gamma_{\mathrm{SR},1}+\Gamma_{\mathrm{SR},2}}{4} \\ &\mp\frac{1}{2}\sqrt{\left(\Delta_{\mathrm{CLS},2}-\Delta_{\mathrm{CLS},1}+i\frac{\Gamma_{\mathrm{SR},1}-\Gamma_{\mathrm{SR},2}}{2}\right)^2+4\left(\Delta_{12}+i\frac{\Gamma_{12}}{2}\right)^2}. \end{aligned} \tag{5.17}$$

Note, that the naming of $\lambda_{1,2}$ corresponding to the respective $\mp$ term in the above equation is meaningful for each single cavity, but arbitrary when relating similar cavities to each other. In the coupling matrix $\boldsymbol{C}$, the various decay enhancements,

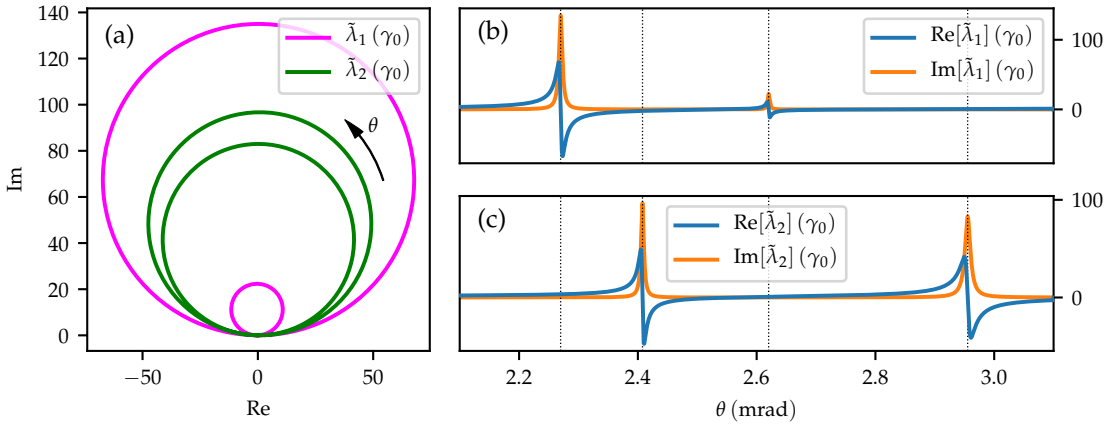

Fig. 5.12: Trajectories of the eigenvalues corresponding to the two excitonic normal modes upon tuning the angle of incidence for the cavity of Fig. 5.3. Panel (a) shows the eigenvalues in the complex plane where the arrow indicates the direction of increasing angle. Panel (b) and (c) show the explicit dependency of the eigenvalues on the angle of incidence. Note that starting from Eq. (5.17), we have to exchange λ_1 and λ_2 at each of the angles indicated by dashed lines to ensure continuity of the eigenvalues. The discontinuity is introduced by the branch cut of the square root.

frequency shifts and coupling constants are continuous functions of the cavity parameters. Whenever the argument of the square root in the above expression crosses the branch cut of the square root, however, it introduces an artificial discontinuity.

We illustrate this, and the general behavior of the normal modes, in Fig. 5.12. Here, we consider the eigenvalues $\lambda_{1,2}$ as a function of the angle of incidence for the cavity of Fig. 5.3. Note that we do not directly plot λ_1 and λ_2, but enforce continuity on the eigenvalues, that is we define new quantities $\tilde{\lambda}_1(\theta), \tilde{\lambda}_2(\theta) \in \{\lambda_1(\theta), \lambda_2(\theta)\}$ such that $\tilde{\lambda}_1$ and $\tilde{\lambda}_2$ are continuous functions of the angle of incidence. In practice, this means that we have to exchange the definition, $\tilde{\lambda}_{1,2} = \lambda_{1,2} \leftrightarrow \tilde{\lambda}_{1,2} = \lambda_{2,1}$, whenever the argument of the square root in Eq. (5.17) crosses the square root's branch cut in the complex plane. For the cavity in Fig. 5.12, this happens upon reaching any of the dotted lines in Fig. 5.12(b) and (c). Hence, we have to keep in mind that in general $\lambda_{1,2}$ cannot be associated to the properties of a unique first and second normal mode.

Note, however, that this is merely a technical detail that leaves a straightforward interpretation of the resulting eigenvalue trajectories in Fig. 5.12 intact. Here, we see that the trajectories of the normal frequencies behave analogous to the CLS and SR of a single resonant layer, see. Fig. 4.1. Interestingly, one of the normal modes is only coupled to the odd modes of the cavity while the second normal mode is solely coupled to even cavity modes. Additionally to the thick cladding, this renders the single mode approximation of Eq. (4.2) highly applicable, thus explaining the circular appearance of the trajectories in Fig. 5.12(a).

	$\lambda_1\,(\gamma_0)$	$\lambda_2\,(\gamma_0)$	$g_1\,(\gamma_0)$	$g_2\,(\gamma_0)$
Fig. 5.10(a)	$-3.1+1.2i$	$11+5.4i$	$0.92-1.9i$	$7.8-1.4i$
Fig. 5.10(b)	$-3.3+0.23i$	$15+3.6i$	$(-3.7-12i)\times 10^{-3}$	$0.61-1.9i$

Tab. 5.4: Eigenvalues and spectral weights for the excitonic normal modes determining the spectral response according to Eq. (5.16). The parameters shown are for the two cavities considered in Fig. 5.10.

In the context of the diagonalization, it should be noted that the matrix $\boldsymbol{C}$ is not hermitian such that we cannot generally expect it to be diagonalizable. If we find $\boldsymbol{C}$ to be non-diagonalizable, this would correspond to the occurrence of an exceptional point [96, 97]. For most parameter choices, however, $\boldsymbol{C}$ will have two different eigenvectors, and therefore a diagonal form can be calculated.

5.5.1 Suppressed spectral response in EIT systems

With the tool of nuclear excitonic normal modes, we can now take a second look at the cavities considered in Fig. 5.10 and calculate the parameters governing the normal modes' imprint on the spectrum. We show the eigenvalue together with the corresponding weight in Tab. 5.4. Both configurations show moderate values for the eigenvalues. However, while for Fig. 5.10(a), both normal modes have weights on the same order of magnitude, it is obvious that for Fig. 5.10(b) the narrow normal mode is highly suppressed.

Although the properties of the three-level scheme in-principle comply with the EIT condition Eq. (5.12) for the case of Fig. 5.10(b) (cf. Tab. 5.2), the final composition of the spectrum, involving the in- and out-coupling, counteracts the visibility of the nuclear dynamics. We can thus attribute the missing EIT signature as a feature of extracting information about the nuclear dynamics via the reflection spectrum.

Finally, it should be noted that, compared to Fig. 5.10(b), the level scheme properties associated with the cavity of Fig. 5.10(a) seem more suitable to the observation of EIT as, firstly, the field probing the metastable state is smaller and, secondly, also the EIT condition Eq. (5.12) is fulfilled more clearly. However, this must not be mistaken for the reason for the vanishing EIT signature. Indeed, idealized cavities can be constructed such that the resulting level scheme properties are almost identical for the conventions Eqs. (5.13) and (5.14). Nevertheless, also for such settings an EIT-dip is visible only for the case of Eq. (5.13), which shows that this is a generic feature of the platform [98].

In turn, a design approach to directly incorporate the spectral weight g_n for each eigenvalue elegantly avoids this problem. Using a specific example, we illustrate the inverse design of the reflection spectrum in the following.

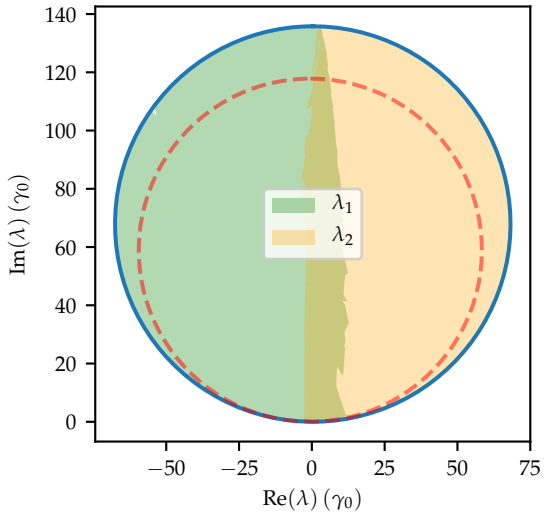

Fig. 5.13: Accessible OS for the eigenvalues within the normal mode approach for a Pd/B_4C/^{57}Fe/B_4C/^{57}Fe/B_4C/Pd/Si cavity setup. For the determination of the overall OS, we selected the eigenvalue of largest imaginary part, thus taking into account the resonances of both normal modes at the same time, see Eq. (5.18). The surface of the respective OS is indicated in blue. The green and orange shaded areas show the accessible spaces for the eigenvalues $\lambda_{1,2}$ according to Eq. (5.17). Note that the separation into λ_1 and λ_2 is not unique. The red dashed line corresponds to the extremal Δ_{CLS} and $\Gamma_{\mathrm{SR}}/2$ that are accessible by a single resonant layer within an archetype Pd/B_4C/^{57}Fe/B_4C/Pd/Si cavity setup. We see that values outside this single layer circle can be realized, showing that multiple layers can unlock new parameter regimes of effective single resonances.

5.5.2 Design of spectral response – operation as two-level system

Having introduced the tool of nuclear excitonic normal modes, we illustrate in the following that we can use this approach to design the spectral response of the cavity.

As a first step, we consider the eigenvalues $\lambda_{1,2}$ accessible with the cavity of Fig. 5.1(a). At the beginning of this section, we already saw that λ_1 or λ_2 are not associated uniquely to the first and second normal mode, but the assignment switches for different cavity parameters (e.g., with the angle of incidence, see Fig. 5.12). From the trajectories in Fig. 5.12(b) and (c) however, we see that, when being close to one resonance, the major tuning capabilities come from one normal mode only while the second one stays approximately constant. Here, the normal mode dominating the tuning capabilities around the resonance mostly has the larger imaginary part. To capture the full tuning capability of the eigenvalues, we therefore consider the eigenvalue with the largest imaginary part,

$$\lambda := \begin{cases} \lambda_1\,, & \text{if} \quad \mathrm{Im}(\lambda_1) \geq \mathrm{Im}(\lambda_2)\,, \\ \lambda_2\,, & \text{else}\,, \end{cases} \tag{5.18}$$

and determine the accessible OS surface for this quantity. The blue curve in Fig. 5.13 shows this surface, that is it represents the extremal values accessible for the real and imaginary part of λ. To make sure that the approach found all accessible eigenvalues, we further consider the OSs for each eigenvalue $\lambda_{1,2}$ according to Eq. (5.17). These are represented by the green and orange shaded areas for λ_1 and λ_2, respectively. Since the union of both areas coincides with the set found for λ, we can be sure to have sampled all accessible eigenvalues. Note, however, that the division of the set into λ_1 and λ_2, and also their overlap in the center, has no physical relevance.

Considering the trajectories in Fig. 5.12, is is not surprising that the OS in Fig. 5.13 is found to be circular.

Interestingly, the eigenvalues can have imaginary part up to about $135\,\gamma_0$. This is beyond the linewidths accessible with an archetype system with single resonant layer of the type of Fig. 1.1(left). Using the same material combination, the accessible linewidth for such systems is found to be $< 118\,\gamma_0$, see the Pd-B_4C combination in Fig. 4.9. To illustrate this, we plot the boundary of accessible Δ_{CLS} and $\Gamma_{\mathrm{SR}}/2$ for the single resonant layer system as red dashed line in Fig. 5.13.

From the analysis of the supposed EIT spectrum, we learned that under suitable conditions, the spectral imprint of one of the normal modes can be highly suppressed. As an intriguing application, this allows to envision the realization of a two-level system with enhanced tuning capabilities when one normal mode is completely suppressed while the other one shows properties beyond the single resonant layer capabilities. Indeed, in the following, we show that an artificial two-level system with decay beyond the archetype systems considered in Chapter 4 is possible.

To that end, we consider the weights g_n of both modes. In fact, the absolute value of g_n is not decisive for the spectral imprint of a normal mode, but we additionally have to scale the weight by the normal mode's linewidth, $g_n/\mathrm{Im}(\lambda_n)$. In order to suppress one mode while having maximum weight for the other one, we consider the difference of both modes' weight, $|g_1|/\,\mathrm{Im}(\lambda_1) - |g_2|/\,\mathrm{Im}(\lambda_2)$, as an observable. When this quantity is positive and large, mainly λ_1 contributes to the spectrum. Likewise, the influence of λ_1 is suppressed in comparison to λ_2 for large and negative values. We complement this observable with the imaginary parts of both eigenvalues. This allows us to estimate the imprint of the eigenmodes simultaneously with the corresponding linewidths.

Note that even though the assignment of normal modes to eigenvalues $\lambda_{1,2}$ is not unique, our sampling is complete as long as we consider both eigenvalues in a single OS.

The surface of the accessible OS for the above observables is shown in Fig. 5.14(a). As for some plots before, we directly show the calculated surface points in the figure. From the projection of the set onto the plane of the imaginary parts, it is clear that when the linewidth of one normal mode is large, the other one necessarily tends to be small. The surface shows a bimodal structure where either λ_1 or λ_2 takes the role as the eigenvalue of larger imaginary part. Due to the apparent symmetry we can choose λ_2 to take the role of the dominant eigenvalue and try to suppress the influence of the remaining normal mode. As the imaginary part of the suppressed eigenvalue is of no significance in the following, we project the OS onto the plane normal to $\mathrm{Im}(\lambda_1)$, see Fig. 5.14(b). When approaching very large linewidths, the tuning capabilities for the weight difference rapidly drop.

We mark two selected cavities in Fig. 5.14(b) and consider their reflection spectrum in the following. Fig. 5.14(c) shows a spectrum with a linewidth of about $131\,\gamma_0$. The influence of the other normal mode is still visible as a small dip, but largely

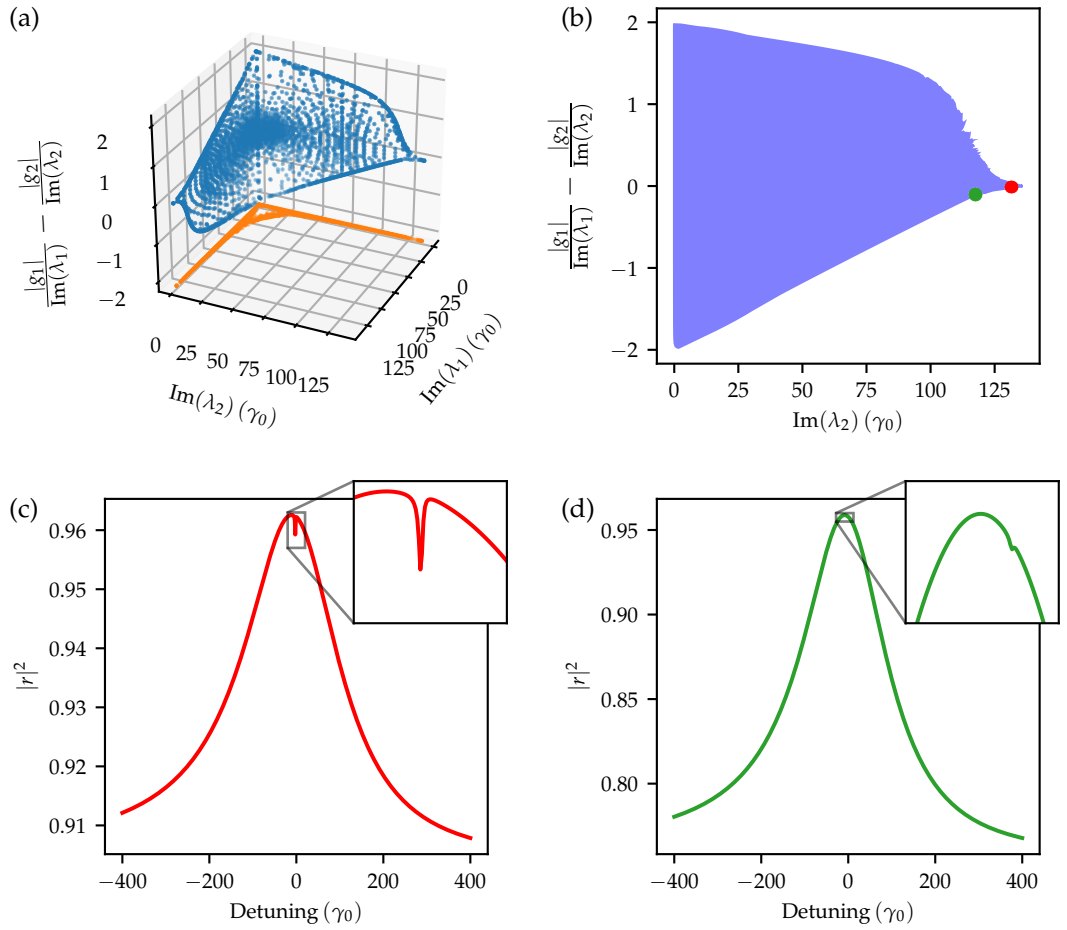

Fig. 5.14: (a) Accessible OS for the linewidth enhancements for both normal modes together with the difference of their scaled spectral weights. The blue dots indicate the computed surface points of the set of accessible combinations. Orange dots indicate the projection of the points onto the plane spanned by the imaginary parts of the eigenvalues. (b) Projection of the surface of (a) onto the plane normal to the $\mathrm{Im}(\lambda_1)$ direction. The red and green dots indicate the cavities used for panel (c) and (d), respectively. (c) Reflected intensity as a function of the detuning from the bare nuclear transition frequency for a Pd(9.9 nm)/B_4C(29.0 nm)/^{57}Fe (0.57 nm)/B_4C(16.9 nm)/^{57}Fe (0.57 nm)/B_4C(19.6 nm)/Pd(10.8 nm)/Si cavity setup probed at an angle of 2.30 mrad. The dominant eigenvalue $\lambda_2 = (2.5 + 131.4i)\gamma_0$ shows a linewidth enhancement larger than what is achievable with only one resonant layer in an analogous setting. (d) Analogous to panel (c), but for an Pd(7.9 nm)/B_4C(27.7 nm)/^{57}Fe (0.57 nm)/B_4C(50.6 nm)/^{57}Fe (0.57 nm)/B_4C(27.0 nm)/Pd(16.6 nm)/Si cavity probed at an angle of 2.34 mrad, where the relevant eigenvalue is $\lambda_2 = (1.6 + 117.6i)\gamma_0$. The linewidth enhancement is very close to the ones achievable with a single resonant layer in an analogous setting, but the visibility is greatly enhanced.

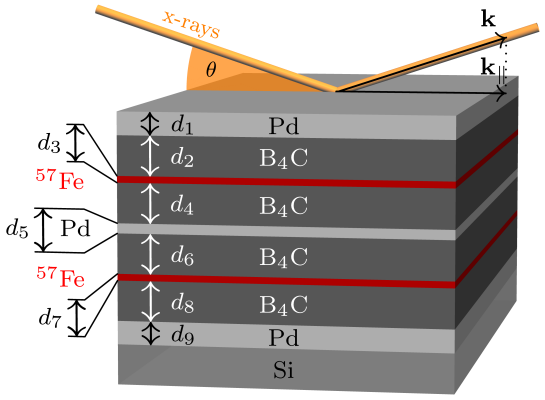

Fig. 5.15: Schematic setup of a thin-film double-cavity with two resonant layers and a separating cladding layer in between. Both resonant layers are embedded in a single guiding layer for this system. The layer thicknesses as well as exemplary materials are indicated.

suppressed as compared to the spectral imprint of the broad normal mode. Therefore, this indeed admits the interpretation as a two-level system with SR beyond what is possible within the archetype setups of Chapter 4. We note that the higher SR is only possible due to the coupling between the two bare excitons.

Likewise, Fig. 5.14(d) shows a cavity that is chosen to have linewidth enhancement of $118\,\gamma_0$ which is very close to the maximally achievable value for archetype systems with a single resonant layer. Due to the enhanced tuning capabilities in the weight difference for this smaller linewidth, the remaining normal mode can be suppressed by orders of magnitude. In principle, a similar SR would be accessible with the archetypal systems of Chapter 4. However, for single resonant layer systems with a SR close to the maximally achievable one, the visibility would be close to zero. Opposed to that, the system in Fig. 5.14(d) shows a much higher visibility. This highlights a way to realize two-level systems with high SR and high visibility at the same time.

The systematic analysis of the accessible normal mode properties and the subsequent inverse design allowed for the determination of cavity structures exhibiting these desirable properties. This shows that the inverse design of systems beyond a single resonant layer is meaningful and promises the exploration of new effects in the realm of x-ray quantum optics.

5.5.3 Double cavity geometry

Finally, a thin-film cavity layout beyond the one of Fig. 5.1(a) is the setup shown in Fig. 5.15. This setup has already been applied in nuclear quantum optics [54]. The system comprises an additional cladding layer inserted in the guiding layer, thus rendering the system a double-cavity-like setup. For its higher complexity, enhanced tuning capabilities can be expected also for the inverse design, particularly also for the design on the basis of excitonic normal modes.

Fig. 5.16 gives some glimpses into what can be expected in this setting. For the achievable eigenvalues according to Eq. (5.18), one finds that the tuning capabilities

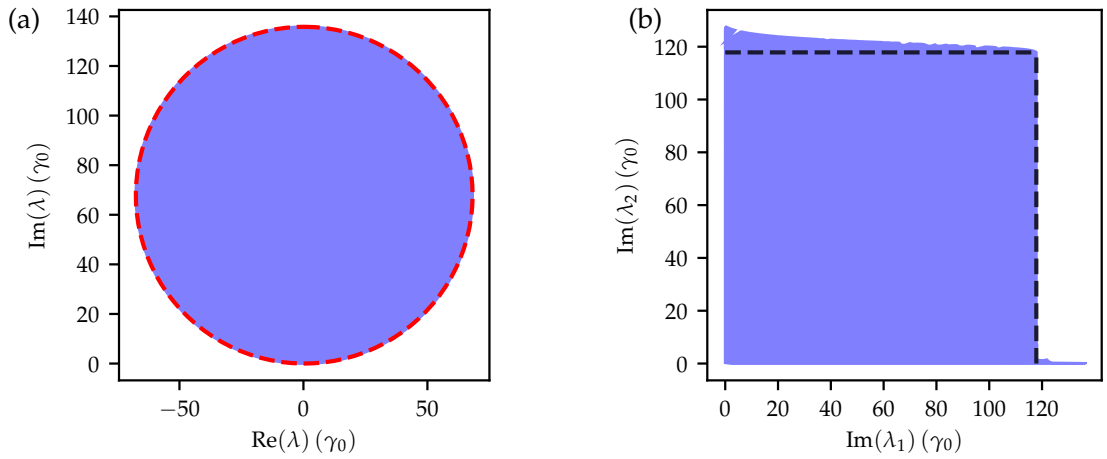

Fig. 5.16: Accessible OS for the eigenvalues for the excitonic normal modes in the Pd/B_4C/^{57}Fe B_4C/Pd/B_4C/^{57}Fe/B_4C/Pd/Si cavity of Fig. 5.15. (a) The blue shaded area shows the accessible eigenvalues for the normal modes according to Eq. (5.18). The red dashed line indicates the surface of the accessible eigenvalues for the cavity of Fig. 5.1(a), see Fig. 5.13. Obviously, the range of accessible eigenvalues is the same for both setups. Panel (b) shows the accessible combinations of linewidth enhancements as calculated from Eq. (5.17). Here, the black dashed lines indicate the maximum SR achievable in an archetype Pd/B_4C/^{57}Fe/B_4C/Pd/Si setup. For a very big central cladding layer, essentially one of these setups is realized for each normal mode.

in Fig. 5.16(a) are identical to the ones in Fig. 5.13, which result for the simpler system in Fig. 5.1(a). Opposed to that, comparing Fig. 5.16(b) to the orange dots in Fig. 5.14(b), the cavity of Fig. 5.15 allows for a considerably larger OS of the linewidth enhancements.

In principle, this is easily understood when considering that for a very thick central cladding layer, the excitons in the resonant layers are uncoupled and the above diagonalization is hence trivial. For that case, the two nuclear excitons can essentially be tuned independently from one another. For each of the resonant layers, this yields tuning capabilities on the linewidth enhancement as large as for an archetypal setup with single resonant layer and the same material combination. The range, up to which this is possible is indicated by black dashed lines in Fig. 5.16(b). However, the OS also shows regions were $\mathrm{Im}(\lambda_2)$ is beyond these limits while $\mathrm{Im}(\lambda_1)$ is quite large. Here, the coupling between the excitons plays a crucial role. Furthermore, the calculated OS is asymmetric in the accessible ranges of λ_1 and λ_2.

Whether these observations for the more complex setup in Fig. 5.15 provide the basis for the design of novel intriguing nuclear dynamics and reflection spectra remains to be explored but is beyond the scope of the present thesis. The methods described in the subsequent chapter, however, can be applied in very much the same way.

Summarizing, the description of the spectral response in terms of excitonic normal modes provides a clear interpretation of this observable. Further, using the inverse design approach in combination with excitonic normal modes is a powerful method to design the reflection spectrum and promises to unlock new phenomena and applications in x-ray quantum optics.

6 Numerical methods

In this chapter, we introduce and explain the numerical methods used throughout this thesis. The chapter shall serve as a guide to understand, and potentially reproduce, the various analyses of accessible level scheme property combinations in the thesis.

We remind the reader that we often refer to such level scheme properties as *observables* and call the set of accessible combinations of some observables the *observables space* (OS). In contrast, the observables are functions of the *cavity parameters* which usually comprise the layer thicknesses and the angle of incidence in the thesis. This distinction is to be kept in mind as we will also introduce *cost functions* as functions of the observables in the following.

Throughout the thesis, we identify how far the properties of the artificial level schemes can be jointly tuned as functions of the cavity parameters. That is, we determine the surfaces of the respective multidimensional OSs. In principle, this can be achieved by enforcing a fixed value for all but one of the observables and maximizing the remaining one. However, this turns out to be numerically expensive. Here, we employ a different approach that works without setting such constraints, but relies on constructing suitable scalar cost functions f from the observables which can then be passed to the maximization algorithm. Maximizing the functions f over the cavity parameters will then be equivalent to determining surface points of the desired OS. In the following, we explain the conceptual basis and challenges of our approach, using the example shown in Fig. 6.1. A comprehensive overview of an exemplary workflow of the approach is given in Fig. 6.2.

6.1 Linear cost functions

We illustrate the approach by the determination of the surface of the exemplary two-dimensional OS in Fig. 6.1(a). The OS comprises all possible combinations of two observables x and y of a model system, e.g., a cavity structure. Its surface therefore allows one to asses the maximum tunability of the two observables. The most straightforward way of constructing a joint cost function of several observables is taking linear combinations. Maximizing a single observable, e.g, $f = x$ or $f = -y$, as a function of the cavity parameters would correspond to determining a boundary point of the OS in a specific direction. Likewise, using a cost function

$$f_\varphi(x, y) = x \sin\varphi + y \cos\varphi \tag{6.1}$$

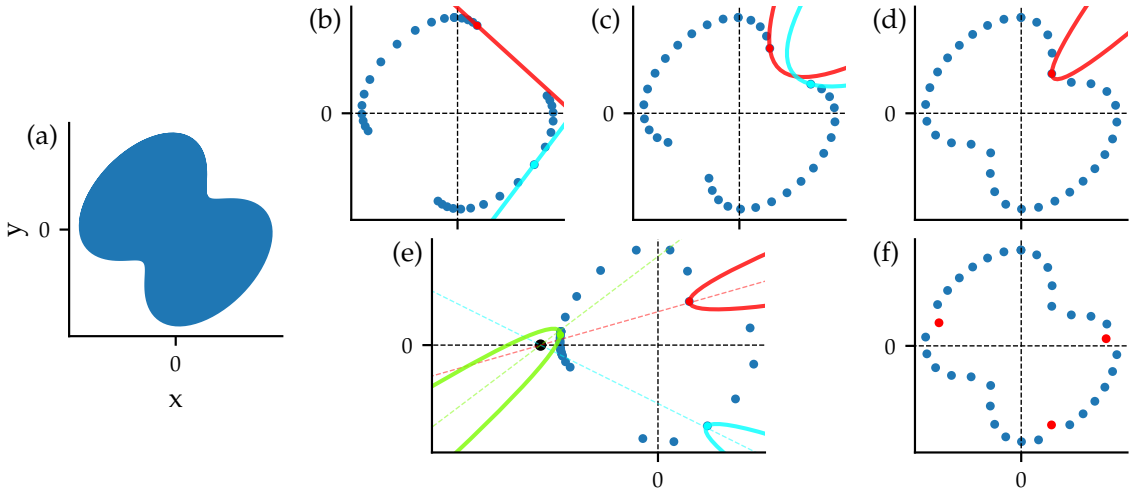

Fig. 6.1: Numerical methods for the determination of the surface of an OS, applied to a two-dimensional, non-convex example. Panel (a) shows the 2D set whose boundary shall be determined numerically. The set is the image of the observables x, y over all cavity parameters. Panels (a-e) illustrate different trials to determine the boundary of the set in (a). In (b), linear combinations of the observables x and y according to Eq. (6.1) are taken as cost functions. The cost function is parametrized by an angle which is sampled equidistantly in the $[0, 2\pi)$ interval. The blue dots indicate the outcomes of the optimization for each angle. For two of these samples (red and cyan) the line of constant cost function as converged to a boundary point is shown. Clearly, this sampling mode can only determine the convex hull of the set in (a). Panel (c) is analogous to panel (b) but for nonlinear combinations of x and y corresponding to comparatively broad parabolae as curves of constant cost functions, see Eqs. (6.4, 6.5). The boundary of the set in (a) is sampled beyond the convex hull, however, the parabola is not narrow enough to successfully determine the whole surface. This is improved in panel (d) where a more narrow parabola is used to construct the cost functions. This allows for the determination of the entire surface. For panels (b-d), the curves of constant cost function were rotated around the origin. In panel (e), the effect of choosing a different center of rotation, indicated as a black dot, is shown. Three different parabolae of constant cost function are shown and their orientation to the point of rotation is illustrated by colored dashed lines. The homogeneity of the boundary points found by this class of cost functions is significantly reduced as compared to the case in (d). Finally, panel (f) shows a typical result where the cost function was chosen suitably [identically to (d)], but the optimizations are only partly converged. Expecting a smooth surface, one can, however, identify potentially non-converged points (indicated in red) and refine the optimization towards convergence.

allows us to change this direction of maximization by a rotation angle φ. We equidistantly sample the angle φ in this function between 0 and 2π and maximize the respective cost functions. Each value φ yields a blue dot in Fig. 6.1(b) by evaluating x and y at the cavity parameters that maximize f_φ. It can be seen, however, that we only determined points on the convex hull of the surface. This is understood when considering that the curves where the cost functions f_φ are constant in the x-y-plane are simply straight lines. The red line in Fig. 6.1(b) exemplifies this for one specific angle. The red dot corresponds to the resulting surface point which is the outermost point to which the red line can be shifted such that it still touches the surface – it thus maximizes f_φ. Obviously, this is not sufficient as we are not capable of determining the whole OS surface by this approach.

The geometrical picture developed above suggests that by constructing a cost function which is constant on a suitable curve, the entire surface can be sampled. To that end, we first consider the curve where the linear cost function Eq. (6.1) is constant,

$$\begin{aligned}\left\{(x,y)\in\mathbb{R}^2|x\sin\varphi+y\cos\varphi=\mathcal{C}\right\}&=\left\{(x,y)\in\mathbb{R}^2|y'=\mathcal{C},\boldsymbol{r'}=\boldsymbol{R}^{-1}(\varphi)\boldsymbol{r}\right\}=\\&=\boldsymbol{R}(\varphi)\left\{(x,y)\in\mathbb{R}^2|y=\mathcal{C},\right\}\,.\end{aligned}\tag{6.2}$$

Here, $\boldsymbol{r}=(x,y)^{\mathrm{T}}$, $\boldsymbol{r'}=(x',y')^{\mathrm{T}}$, $\mathcal{C}$ is a constant, and

$$\boldsymbol{R}(\varphi)=\begin{pmatrix}\cos\varphi & \sin\varphi\\ -\sin\varphi & \cos\varphi\end{pmatrix}\tag{6.3}$$

is a standard two-dimensional rotation matrix. Eq. (6.2) manifests the relation between the cost function on one hand and the curve where it is constant on the other one. For the present cost function this curve is a horizontal line rotated by an angle φ around the origin.

6.2 Nonlinear cost functions

Bearing the geometrical picture in mind, a simple generalization of the rotated line is a rotated parabola, given by

$$\boldsymbol{R}(\varphi)\left\{(x,y)\in\mathbb{R}^2|y-\alpha x^2=\mathcal{C}\right\}=\left\{(x,y)\in\mathbb{R}^2|y'-\alpha x'^2=\mathcal{C},\boldsymbol{r'}=\boldsymbol{R}^{-1}(\varphi)\boldsymbol{r}\right\}\,,\tag{6.4}$$

where α characterizes the parabola's width. With the curvature of the parabola, we can hope to be able to resolve the surface also in the parts that could not be obtained previously.

By analogy to Eq. (6.2), we deduce the corresponding cost functions f_φ to be

$$f_\varphi(x,y)=y'-\alpha x'^2\,,\quad\text{where}\quad\boldsymbol{r'}=\boldsymbol{R}^{-1}(\varphi)\boldsymbol{r}\,.\tag{6.5}$$

Fig. 6.1(c) shows sampling points as obtained by using a comparatively broad parabola. Clearly, the surface is sampled better than with the linear cost functions, but not yet fully covered by the sampling points. Similar to the linear cost function, shown in red in Fig. 6.1(b), the parabola is too broad to resolve the full boundary. However, upon reducing the width of the parabola we finally retrieve the full surface of the two-dimensional OS, see Fig. 6.1(c).

It is clear that only the surfaces of certain sets can be fully sampled using parabolae, and in principle, more complex cost functions could be considered. However, it is important to note that the surface points obtained using a particular class of cost functions are valid solutions to the problem, even if the cost functions are not capable of sampling the entire surface. Hence, it is possible to certify the applicability of a particular class of cost functions by assessing whether it samples the whole surface of the given set. This is not the case in Fig. 6.1(b) and (c), but a sampling of the entire surface is achieved in (d).

It may be computationally demanding to sample the entire surface with a class of complex cost functions. It is therefore favorable to start any determination of a surface by a simple linear combination of observables. Only in the next steps, increasingly more sophisticated cost functions are used to refine the procedure in undetermined surface regions until full coverage of the surface is reached. The surface points obtained with all considered classes of cost functions are then combined for a comprehensive determination of the surface. This approach was used, e.g., in the determination of Fig. 4.2.

The entire iterative procedure of our numerical approach is summarized in Fig. 6.2. For the optimizations considered in the present work, parabolae proved sufficient.

For the Figs. 6.1(b-d) we only considered parabolae rotated around the origin, which conveniently coincided with the center of the two-dimensional OS. However, more general transformations of the considered class of cost functions are possible, e.g., rotations around different centers of rotation or translations along some path. For the example in Fig. 6.1(a), we find that the homogeneity of the obtained surface points is largely reduced by changing the center of rotation, see Fig. 6.1(e). This suggests that more general transformations of a given class of cost functions may be useful to cover larger surface parts in other systems. Starting out with a linear cost function once again is highly advisable as for this kind of cost function the sampling is irrespective of the rotation center and thus no sensible guess is needed – changing the rotation center essentially only alters the value f reaches at its maximum but not for which cavity parameters the maximum is reached.

The results given for the exemplary two-dimensional setting readily generalize to three dimensions, e.g., when considering SR, CLS, and the visibility as the OS. The respective cost function can then be given as

$$f(x, y, z) = z' - \alpha(x'^2 + y'^2)\,, \quad \text{where} \quad \boldsymbol{r}' = \boldsymbol{R}^{-1}(\theta, \varphi)\boldsymbol{r}\,, \tag{6.6}$$

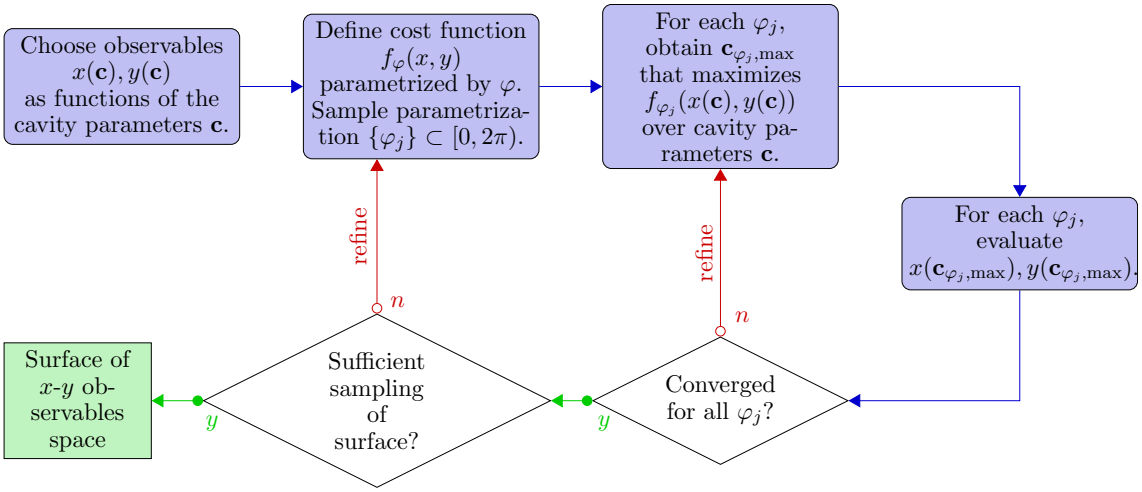

Fig. 6.2: Schematic workflow for the numerical determination of OS surfaces, using the example of Fig. 6.1. Initially, the observables x and y for which the OS surface shall be determined are chosen. Next, a suitable cost function $f_\varphi(x, y)$ is defined as a function of these observables. The cost function is parametrized by φ to probe the surface in different directions. An adequate number of samples φ_j has to be selected from the domain of the parametrization. As a start, choosing a linear cost function according to Eq. (6.1) and a number of homogeneously spaced samples φ_j is reasonable. In the next step, the cost function is maximized over the cavity parameters $\boldsymbol{c}$ (i.e. the angle of incidence and the layer thicknesses in the main text). The maximization is carried out independently for each value of the parametrization φ_j which yields the respective maximal cavity parameters $\boldsymbol{c}_{\varphi_j,\max}$. The observables x and y are evaluated at these cavity parameters to yield the samples of the OS in the x-y-plane. Subsequently it has to be verified that for each φ_j the numerical maximization is converged. An indication for bad convergence can be discontinuities in the surface samples, as illustrated in Fig. 6.1(f). If not all points are fully converged, the maximization should be refined, e.g., by carrying out the maximization for more, or better, initial guesses for the cavity parameters $\boldsymbol{c}$. If convergence is achieved, the subsequent step is to verify that the whole surface of the OS is sampled sufficiently. If this is not the case, refining the cost function and/or increasing the number of samples of the parametrization is necessary. This could include the use of nonlinear cost functions, such as in Eq. (6.4), or of a different set of transformations applied to the cost function. When the cost functions and the sampling of the parametrization are chosen suitably, the surface of the OS is finally obtained.

with $\boldsymbol{r} = (x, y, z)^{\mathrm{T}}$, $\boldsymbol{r}' = (x', y', z')^{\mathrm{T}}$, and a three-dimensional rotation matrix $\boldsymbol{R}(\theta, \varphi)$, parametrized by polar and azimuthal angle. The linear sampling is achieved for $\alpha = 0$. Note that while we considered two- and three-dimensional OSs only, no in-principle restrictions apply as to finding the surfaces of higher dimensional spaces, e.g. using four-dimensional rotation matrices. Due to the limits of human imagination and two-dimensional paper, however, the presentation and interpretation of such higher dimensional sets is difficult.

6.3 Convergence

Finally, the previous discussion focused only on the construction of suitable cost functions. However, for each optimization of a cost function, we further have to ensure that the maximization as a function of the cavity parameters converges to its global optimum and not a local one. To this end, we use the `scipy.optimize` [99] package for the maximization. To support the convergence, we repeat the same maximization for many different initial conditions which we Monte-Carlo sample from a meaningful range in the cavity parameters. Furthermore, non-converged points are typically visible as discontinuities in otherwise smooth surfaces, see Fig. 6.1(f). In case of non-converged points, the number of maximizations starting from different initial conditions can be increased until all cost functions converge to the boundary of the OS. It sometimes also proves necessary to enlarge the – large, but of course finite – range of cavity parameters which the initial guesses are Monte-Carlo sampled from. This is in particular necessary when the potentially non-converged points are found to come with cavity parameters very different from the neighboring points. Lastly, it should be noted that less complicated, and in particular linear cost functions, are heuristically found to show the best convergence properties.

7 Conclusions & Outlook

The main result of the present thesis is the successful introduction of an inverse approach to the design of artificial x-ray few-level schemes on the basis of Mössbauer nuclei in thin-film cavities. We developed the inverse design at the example of artificial two-level schemes and subsequently demonstrated its applicability to more complex systems by engineering x-ray quantum optical effects involving three-level systems. Using the approach, striking new insights were revealed in terms of both, x-ray quantum optical setups and the cavities they are realized in.

For artificial two-level schemes based on a single resonant layer in an archetype cavity, we provided a systematic determination of the frequency shifts, decay enhancements and driving field strengths, also taking into account the experimental observability. The resulting properties of the quantum systems could be understood when considering the underlying mode structure of the cavity.

For all accessible properties of the two-level scheme, we were able to give explicit cavity geometries. This certifies the successful implementation of the *inverse design*. Using the inverse approach gives immediate and comprehensive access to all realizable level schemes, and thus renders a trial-and-error approach to the design of quantum optical effects unnecessary.

Determining the accessible properties of the two-level scheme, we found that cavities without top cladding layer can outperform archetype ones regarding the in- and out-coupling of x-rays. This unexpected result opens up a novel and potentially preferable type of thin-film cavity that has not been recognized so far.

We further showed that geometries maximizing the field enhancement inside the thin-film cavity are different from those that generate large decay enhancement. This is counter-intuitive, as the comparison to a two-level system in an optical Fabry-Pérot cavity revealed that both maxima coincide for the latter case. The insight advances the intuitive understanding of thin-film environments which is crucial for envisioning new ideas and applications.

Strikingly, our analysis of different material combinations raised doubts about the commonly applied paradigm of *high-Z cladding – low Z guiding* materials, but demonstrated that low absorption in the cladding layer is significant for large collective effects. As a result, we found that establishing a *low-Z cladding – lower-Z guiding* paradigm promises to enhance the performance and versatility of future cavities. Further, our results may spark interest in materials which were disregarded so far for the construction of x-ray photonic structures.

Moreover, studying different resonant isotopes showed that upon choosing one Mössbauer isotope, also its impact on the photonic environment has to be taken into account. Using our comprehensive approach to analyze the performance of a specific resonant isotope in the cavity can give guidance to match the appropriate isotope to the right application.

At the example of systems with two resonant layers, we demonstrated that the inverse design approach is readily extended to more complex systems. For the resulting three-level schemes, we again gave a comprehensive determination of the realizable properties. As before, considerations about the mode structure of the cavities shed light on the scope of the accessible combinations of the level scheme parameters.

Subsequently, we could not only successfully implement the inverse design of three-level systems, but also relevant ratios of level scheme parameters were readily engineered. In that context, we used the electromagnetically induced transparency effect to illustrate the design of relevant quantum optical setups otherwise inaccessible at x-ray energies. This proves that the inverse design constitutes a viable tool to the implementation of further quantum optical schemes at x-ray energies.

While implementing electromagnetically induced transparency, we found that the signatures resulting from the artificial level schemes are different from those in standard quantum optics. This is because for the x-ray thin-film case, the experimentally relevant observable is the reflection spectrum that comprises in- and out-coupling effects. Representing the nuclear imprint on this reflection spectrum in a diagonal form, we developed a method that gives immediate access to the observable signatures and facilitates the interpretation of the spectrum. For the case of two resonant layers, not the two coupled excitons in the layers are described within this approach but their uncoupled excitonic normal modes. Since the magnitude and properties of these eigenmodes are readily accessed, we can not only explain signatures in the spectrum, but also apply the inverse approach to efficiently design the spectral response. This provides a powerful method to shape the reflection spectrum towards particular goals.

As an intriguing application, we showed that – owing to the interlayer coupling – one of the eigenmodes can show superradiance beyond what is accessible by a single resonant layer within an analogous setting. Notably, at the same time, the spectral imprint of the second eigenmode can be almost completely suppressed, thus realizing a more versatile x-ray two-level scheme within a setup of two resonant layers.

Summarizing, the inverse design introduced in the thesis provides a way to efficiently engineer artificial x-ray quantum systems and their spectral response. It further brings along general insights that are likely to impact future implementations not only within the present platform, but also for x-ray photonic environments in general.

Outlook

With the methods and insights provided in this thesis, the first steps in inverse design of nuclear quantum optical systems are taken and a plethora of yet unexplored directions has opened up for future research. We outline some of these in the following.

Chapter 5 already hinted at the capabilities of multiple resonant layer systems. However, their full potential remains to be exploited. The inclusion of more than two resonant layers promises the design of intriguing quantum optical setups that bring us closer to the merits of quantum optics at lower frequencies. Using many resonant layers, a systematic tool for the design is indispensable to cover the full design capabilities in the presence of increasingly complex interrelations between various parameters of the level schemes.

Within the framework of nuclear excitonic normal modes in Sec. 5.5, the novel two-level scheme in a platform of two resonant layers promises to not only enlarge the accessible superradiance, but also enhance the collective Lamb shift beyond what is possible with a single layer of nuclei. Further, it remains to be uncovered whether the inclusion of more resonant layers still allows for the description in terms of a two-level scheme. In that case, the resulting two-level system might show even larger tunability of its properties.

Beyond two-level schemes, the description by excitonic normal modes provides straightforward access to the reflection spectrum, also in the presence of complex spectral signatures resulting from a high number of such modes. In combination with the inverse design approach, the normal mode method allows to shape the spectral imprints of advanced level schemes, ranging from electromagnetically induced transparency-like dips [51] to signatures of strong coupling in stacks of resonant layers [53] and beyond that. Eventually, the spectral tuning capabilities provided by the approach could be applied, e.g., to the design of bandpass filters for synchrotron radiation [94] or an enhancement of the non-linear nuclear susceptibility [62] as well as the engineering of intriguing nuclear dynamics in general.

As a yet unexplored direction in the inverse design, one further finds the inclusion of magnetic fields as additional degree of freedom. This thesis has been focused on unmagnetized resonant layers where individual Mössbauer nuclei could be described as two-level systems. In the presence of a magnetic field, however, the hyperfine interactions in ^{57}Fe give rise to six possible transitions with different polarization dependencies. With the resulting enlarged Hilbert space, versatile level schemes have been realized [52] or proposed [49, 56]. Applying the inverse design approach to magnetized layers of Mössbauer isotopes can be expected to open up further design capabilities for x-ray quantum optics towards polarization sensitive tunable x-ray few-level schemes.

Leaving the number and type of resonant layers aside, also the use of more cladding or guiding cavity layers can be thought of. In the optical regime, multi-

layered dielectric mirrors have found numerous applications [100]. Preliminary results suggest, that the inclusion of more non-resonant layers can also boost the performance of thin-film cavities.

Regarding the use of thin-film cavities as photonic environments, different geometries can be thought of. The use of thin-film cavities, as described in this thesis, essentially sacrifices the design capabilities parallel to the layer surfaces for the merit of having an enlarged effective wavelength in the orthogonal direction. In principle, the same enhancement of the effective wavelength would be possible upon restricting the waveguide-like behavior to one dimension only. For that case, two dimensions would be left for photonic design. A corresponding geometry could be provided by cylindrical, and possibly multi-layered, nanofibers with a fiber core of Mössbauer nuclei or also further in-plane structuring of the resonant layers in thin-film cavities, potentially using lithographic tools [101, 102]. For a number of such highly symmetric geometries, the Green's functions are available analytically [70, 103]. This promises an efficient implementation of our design approach.

Beyond that, crystal environments or wave guides could be used to tailor the nuclear dynamics. For unrestricted design approaches, e.g., see [60], however, it must be noted that the practical design on the scale of the x-ray wavelength might be hard. Further, the description of the systems as artificial few-level schemes might be inadequate as different many-body quantum states could be relevant for the dynamics.

A different application for thin-film cavities founds on the large field enhancement they offer, as was illustrated in Chapter 4. This might help to reach the full inversion of nuclear ensembles [28, 104], as was also proposed for other photonic environments [41], and thus could provide access to the full quantum many-body regime.

Finally, our results could be of interest beyond the framework of nuclear quantum optics, e.g., in the development of novel x-ray source concepts [85] or for the application to electronic resonances [18, 105].

Overall, the results of this thesis provide a solid foundation for such endeavors and hopefully will spark research in the directions mentioned above and beyond that.

Acknowledgments

I would like to thank Jörg Evers for his excellent supervision and the cordial support he provided regarding the work on the thesis, but also beyond. Let me further thank Dominik Lentrodt for numerous as well as immediate answers via email and the productive collaboration in general. In that context, I also would like to thank Miriam Gerharz, Lukas Wolff and Pim van den Heuvel for the kind atmosphere they provided in Jörg's group. Besides, I thank the Max Planck Institute for Nuclear Physics for the opportunity to work with their resources. Furthermore, I want to thank Antonino Di Piazza for serving as the second corrector of my thesis. In addition, I gratefully acknowledge the support by the *Cusanuswerk* and the *Studienstiftung des deutschen Volkes* throughout my studies. Moreover, I would like to thank Dominik Lentrodt, Miriam Gerharz, Julia Liebert, Hedwig Oschwald and Tobias Schmale for proofreading parts of this thesis. Special thanks go to my friends and, in particular, my family for their constant support. Finally, I acknowledge "Life, the Universe and Everything" [42].

A Appendix

A.1 Green's functions and field configurations

Here, we summarize relevant formulae for the Green's function and the field configuration as used for the calculations in the main text. For the archetype system with a single resonant layer, see Fig. 1.1, we give the explicit formulae for all relevant quantities to simplify the reproduction of the results. For cavity structures beyond that, e.g., for the cavities of Figs. 5.1(a) and 5.15, we summarize the general form of the formulae as given by [58].

A.1.1 Single resonant layer archetype cavity

For the archetypal thin-film cavity with single resonant layer, see Fig. 1.1, the formulae are given in the following. In accordance with the discussion in the main text, we restrict to the case of s-polarization. The case of p-polarization is included in the general treatment in the subsequent section.

Green's function

The in-plane Fourier transformed Green's function at equal $z = z'$ in the third (resonant) layer is given by

$$\begin{aligned} G(z, z, \boldsymbol{k}_\parallel, \omega) = \frac{i}{2\beta_3} \frac{e^{i\beta_3 d_3}}{1 - r_{3/0} r_{3/6} e^{2i\beta_3 d_3}} \\ \times (e^{i\beta_3(z-d_3)} + r_{3/6} e^{-i\beta_3(z-d_3)})(e^{-i\beta_3 z} + r_{3/0} e^{i\beta_3 z}) \,, \end{aligned} \tag{A.1}$$

where

$$\begin{aligned} r_{3/0} &= \frac{-r_{23} + r_{2/0} e^{2i\beta_2 d_2}}{1 - r_{23} r_{2/0} e^{2i\beta_2 d_2}} \,, \quad & r_{2/0} &= -\frac{r_{12} + r_{01} e^{2i\beta_1 d_1}}{1 + r_{12} r_{01} e^{2i\beta_1 d_1}} \,, \\ r_{3/6} &= \frac{r_{34} + r_{4/6} e^{2i\beta_4 d_4}}{1 + r_{34} r_{4/6} e^{2i\beta_4 d_4}} \,, \quad & r_{4/6} &= \frac{r_{45} + r_{56} e^{2i\beta_5 d_5}}{1 + r_{45} r_{56} e^{2i\beta_5 d_5}} \,. \end{aligned} \tag{A.2}$$

In this formula, r_{ij} denotes the Fresnel coefficient of light in layer i reflected at adjacent layer j. Furthermore, $\beta_j = \sqrt{k_j^2 - \boldsymbol{k}_\parallel^2}$, where $k_j = n_j k_0$ is the wave number in layer j obtained from the refractive index n_j of the layer. The parallel wave vector, in turn, changes with the angle of incidence, $|\boldsymbol{k}_\parallel| = k_0 \cos(\theta)$, where k_0 is the

free-space wave number. The thicknesses d_j are enumerated according to Fig. 1.1 and z denotes the distance to the third layer top surface which we will generally set to the center of the ultrathin resonant layer $z = d_3/2$. It is noted, that simpler cavity structures, e.g., without top cladding layer, can be obtained by setting the respective thicknesses to zero. Note that there is an additional δ-contribution in the Green's function, see Appendix A.1.2. It can be interpreted to renormalize the transition frequency and decay constant in free-space. Therefore, we take it to be already included in the respective parameters [48].

The Green's function propagating the nuclear response to the surface is further given by

$$G(0, z, \boldsymbol{k}_\parallel, \omega) = \frac{i}{2\beta_0} \frac{t_{0/3} e^{i\beta_3 d_3}}{1 - r_{3/0} r_{3/6} e^{2i\beta_3 d_3}} \left(e^{-i\beta_3 (d_3 - z)} + r_{3/6} e^{i\beta_3 (d_3 - z)} \right) . \tag{A.3}$$

The additional coefficients are defined as

$$t_{0/3} = \frac{t_{0/2} t_{23} e^{i\beta_2 d_2}}{1 - r_{2/0} r_{23} e^{2i\beta_2 d_2}} , \quad t_{0/2} = \frac{t_{01} t_{12} e^{i\beta_1 d_1}}{1 + r_{01} r_{12} e^{2i\beta_1 d_1}} , \tag{A.4}$$

for t_{ij} being the Fresnel coefficients of light in layer i being transmitted to adjacent layer j.

Field configuration

The electric field strength at the third, resonant layer is given by [58]

$$E_{\mathrm{in}}(z, \boldsymbol{k}_\parallel, \omega) = \frac{t_{0/3} e^{i\beta_3 d_3}}{1 - r_{3/0} r_{3/6} e^{2i\beta_3 d_3}} \left(e^{i\beta_3 (z - d_3)} + r_{3/6} e^{-i\beta_3 (z - d_3)} \right) , \tag{A.5}$$

where as before we evaluate the field at the center of the ultrathin layer, $z = d_3/2$. Note that this quantity differs from Eq. (A.3) only by a prefactor.

For the calculation of the electronic cavity reflection the field strength at the surface is used,

$$\begin{aligned} E_{\mathrm{in}}(0, \boldsymbol{k}_\parallel, \omega) = 1 + r_{\mathrm{el}} = 1 + \frac{1}{1 - r_{3/0} r_{3/6} e^{2i\beta_3 d_3}} \\ \times \left[r_{0/3} + (t_{0/3} t_{3/0} - r_{0/3} r_{3/0}) r_{3/6} e^{2i\beta_3 d_3} \right] , \end{aligned} \tag{A.6}$$

where the additional coefficients are

$$\begin{aligned} r_{0/3} &= \frac{r_{01} + r_{1/3} e^{2i\beta_1 d_1}}{1 + r_{01} r_{1/3} e^{2i\beta_1 d_1}} , \quad r_{1/3} = \frac{r_{12} + r_{23} e^{2i\beta_2 d_2}}{1 + r_{12} r_{23} e^{2i\beta_2 d_2}} , \\ t_{3/0} &= \frac{t_{3/1} t_{10} e^{i\beta_1 d_1}}{1 + r_{1/3} r_{01} e^{2i\beta_1 d_1}} , \quad t_{3/1} = \frac{t_{32} t_{21} e^{i\beta_2 d_2}}{1 + r_{23} r_{12} e^{2i\beta_2 d_2}} . \end{aligned} \tag{A.7}$$

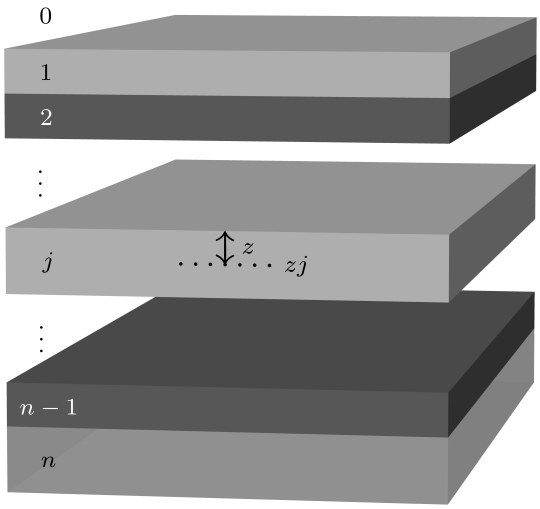

Fig. A.1: Schematic illustration of the enumeration of different layers and the coordinate convention. The coordinate zj lies in the jth layer at a distance of z to the upper surface of the layer. Note that the layers 0 and n are semi-infinitely extended to the top and bottom, respectively.

A.1.2 Generic thin-film cavities

For the remaining cavity structures we summarize the general form of the in-plane Fourier transformed Green's function and the remaining formulae needed for the calculation of the results in the main text. For completeness, we give the expressions for s- and p-polarization in this section and maintain the tensorial character of the Green's function. The notation is kept similar to [58], however, some conventions are changed to reduce ambiguity. The in-plane Fourier-transformed Green's function reads

$$\begin{aligned}\boldsymbol{G}(zj, z'j', \boldsymbol{k}_\parallel, \omega) = &-\frac{1}{k_j^2}\hat{\boldsymbol{z}}\hat{\boldsymbol{z}}\delta(zj - z'j') + \frac{i}{2\beta_n}\sum_{q=\mathrm{p,s}}\frac{\xi_q}{t^q_{0/n}}\times \\ &\times\Big[\boldsymbol{\mathcal{E}}^0_q(zj, \boldsymbol{k}_\parallel, \omega)\boldsymbol{\mathcal{E}}^n_q(z'j', -\boldsymbol{k}_\parallel, \omega)\Theta(zj - z'j') \\ &\quad+\boldsymbol{\mathcal{E}}^n_q(zj, \boldsymbol{k}_\parallel, \omega)\boldsymbol{\mathcal{E}}^0_q(z'j', -\boldsymbol{k}_\parallel, \omega)\Theta(z'j' - zj)\Big]\,, \end{aligned} \tag{A.8}$$

where the vector products correspond to dyadic products and $\xi_{\mathrm{p(s)}} = (-)1$ depends on the polarization $q \in \{\mathrm{s}, \mathrm{p}\}$. Further, $\hat{\boldsymbol{z}}$ is the unit vector in z-direction, i.e., normal to the layer surfaces. The notation zj for the spacial argument is meant to denote the evaluation in the jth layer at a distance z from the jth layer upper surface, see Fig. A.1. For the Heaviside step function this means that

$$\Theta(zj - z'j') = \begin{cases} 1\,, & \text{if} \quad j > j'\,, \\ 1\,, & \text{if} \quad j = j' \text{ and } z > z'\,, \\ \frac{1}{2} & \text{if} \quad j = j' \text{ and } z = z'\,, \\ 0\,, & \text{else}\,. \end{cases} \tag{A.9}$$

Furthermore, we have

$$\boldsymbol{\mathcal{E}}_{\mathrm{p}}^{n(0)}(zj,\boldsymbol{k}_{\parallel},\omega)=\frac{t_{n(0)/j}^{\mathrm{p}}e^{i\beta_j d_j}}{D_{\mathrm{p}j}}\left[\pm\frac{\beta_j}{k_j}\left(e^{-i\beta_j z^{\mp}}-r_{j/0(n)}^{\mathrm{p}}e^{i\beta_j z^{\mp}}\right)\hat{\boldsymbol{k}}_{\parallel}+\right.$$
$$\left.+\frac{k_{\parallel}}{k_j}\left(e^{-i\beta_j z^{\mp}}+r_{j/0(n)}^{\mathrm{p}}e^{i\beta_j z^{\mp}}\right)\hat{\boldsymbol{z}}\right], \tag{A.10}$$

$$\boldsymbol{\mathcal{E}}_{\mathrm{s}}^{n(0)}(zj,\boldsymbol{k}_{\parallel},\omega)=\frac{t_{n(0)/j}^{\mathrm{s}}e^{i\beta_j d_j}}{D_{\mathrm{s}j}}\left[\left(e^{-i\beta_j z^{\mp}}+r_{j/0(n)}^{\mathrm{s}}e^{i\beta_j z^{\mp}}\right)\hat{\boldsymbol{k}}_{\parallel}\times\hat{\boldsymbol{z}}\right], \tag{A.11}$$

$$D_{qj}=1-r_{j/0}^{q}r_{j/n}^{q}e^{2i\beta_j d_j}, \tag{A.12}$$

$$z^{+}=d_j-z,\qquad z^{-}=z, \tag{A.13}$$

where $\hat{\boldsymbol{k}}_{\parallel}=\boldsymbol{k}_{\parallel}/k_{\parallel}$ is the unit vector corresponding to the direction of the in-plane wave vector for $k_{\parallel}=|\boldsymbol{k}_{\parallel}|$. Upon inserting $\boldsymbol{k}_{\parallel}\to-\boldsymbol{k}_{\parallel}$ the unit vector acquires a minus sign. We emphasize that z is the relative coordinate to the layer's upper surface in this notation.

The multilayer Fresnel coefficients read

$$r_{i/k}^{q}=r_{i/j/k}^{q}=\frac{r_{i/j}^{q}+(t_{i/j}^{q}t_{j/i}^{q}-r_{i/j}^{q}r_{j/i}^{q})r_{j/k}^{q}e^{2i\beta_j d_j}}{\mathcal{D}_{qj}^{(ik)}}, \tag{A.14}$$

$$t_{i/k}^{q}=t_{i/j/k}^{q}=\frac{t_{i/j}^{q}t_{j/k}^{q}e^{i\beta_j d_j}}{\mathcal{D}_{qj}^{(ik)}}, \tag{A.15}$$

$$\mathcal{D}_{qj}^{(ik)}=1-r_{j/i}^{q}r_{j/k}^{q}e^{2i\beta_j d_j}, \tag{A.16}$$

where $r_{i/k}^{q}=r_{i/j/k}^{q}$ denotes the reflection coefficient from medium i at the surface of medium k where the contribution of intermediate (possibly several) layers is taken care of. The layer j denotes an intermediate layer, $i<j<k$ or $k<j<i$, such that recursively the multilayer Fresnel coefficients are defined. Analogously, the multilayer transmission coefficients $t_{i/k}^{q}$ are obtained. For adjacent layers – that means there is no such intermediate index j – the multilayer coefficients reduce to the usual Fresnel coefficients for the respective polarization q.

The (off-resonant) field strength in the cavity resulting from an incident plane-wave of unit amplitude (from the top) is further given by $\boldsymbol{E}_{\mathrm{in}}(zj,\boldsymbol{k}_{\parallel},\omega)=\boldsymbol{\mathcal{E}}_{\mathrm{q}}^{0}(zj,\boldsymbol{k}_{\parallel},\omega)$, or the respective superpositions of the different polarizations.

A.2 Mittag-Leffler expansion theorem

Here, we will shortly revisit the Mittag-Leffler expansion theorem as stated in [68].

> Let f be a meromorphic function with simple poles z_k only and continuous, or with removable singularity, at 0. Let $\mathcal{C}_n$ be circular contours of radius R_n, centered at 0, such that $R_n \xrightarrow{n\to\infty} \infty$ and f has no poles on $\mathcal{C}_n$. Further, let there be a real constant $M > 0$, such that for all n, f is bounded by M on $\mathcal{C}_n$. Then, on its domain, the function can be expressed as
>
> $$f(z) = f(0) + \sum_k \mathrm{Res}(f, z_k) \left(\frac{1}{z - z_k} + \frac{1}{z_k} \right), \tag{A.17}$$
>
> where $\mathrm{Res}(f, z_k)$ is the residue of f at z_k and $f(0) = \lim_{z\to 0} f(z)$.

In the main text, the theorem is applied on a heuristic basis and its convergence characterized visually. Due to the constructive nature of the theorem, we can explicitly calculate the expansion coefficients also by numerical means. For this we note, that the residue of a meromorphic function at a pole z_k can be written as a line integral,

$$\mathrm{Res}(f, z_k) = \frac{1}{2\pi i} \int_{\mathcal{C}} \mathrm{d}z\, f(z), \tag{A.18}$$

where $\mathcal{C}$ is a suitable closed contour around z_k. The integral is readily discretized and evaluated numerically, thus allowing us to check the convergence of the expansion for analytically not accessible cavity systems.

Bibliography

[1] Oliver Diekmann, Dominik Lentrodt, and Jörg Evers. Inverse design of artificial two-level systems with Mössbauer nuclei in thin-film cavities. arXiv:2108.01960 [quant-ph], August 2021. URL http://arxiv.org/abs/2108.01960.

[2] Dominik Lentrodt, Oliver Diekmann, Christoph H. Keitel, Stefan Rotter, and Jörg Evers. Classifying and harnessing multi-mode light-matter interaction in lossy resonators. arXiv:2107.11775 [quant-ph], July 2021. URL http://arxiv.org/abs/2107.11775.

[3] Michael G Raymer and Christopher Monroe. The US National Quantum Initiative. Quantum Sci. Technol., 4(2):020504, February 2019. ISSN 2058-9565. doi: 10.1088/2058-9565/ab0441. URL https://iopscience.iop.org/article/10.1088/2058-9565/ab0441.

[4] Qiang Zhang, Feihu Xu, Li Li, Nai-Le Liu, and Jian-Wei Pan. Quantum information research in China. Quantum Sci. Technol., 4(4):040503, November 2019. ISSN 2058-9565. doi: 10.1088/2058-9565/ab4bea. URL https://iopscience.iop.org/article/10.1088/2058-9565/ab4bea.

[5] Max F Riedel, Daniele Binosi, Rob Thew, and Tommaso Calarco. The European quantum technologies flagship programme. Quantum Sci. Technol., 2(3):030501, September 2017. ISSN 2058-9565. doi: 10.1088/2058-9565/aa6aca. URL https://iopscience.iop.org/article/10.1088/2058-9565/aa6aca.

[6] Antonio Acín, Immanuel Bloch, Harry Buhrman, Tommaso Calarco, Christopher Eichler, Jens Eisert, Daniel Esteve, Nicolas Gisin, Steffen J Glaser, Fedor Jelezko, Stefan Kuhr, Maciej Lewenstein, Max F Riedel, Piet O Schmidt, Rob Thew, Andreas Wallraff, Ian Walmsley, and Frank K Wilhelm. The quantum technologies roadmap: a European community view. New J. Phys., 20(8): 080201, August 2018. ISSN 1367-2630. doi: 10.1088/1367-2630/aad1ea. URL https://iopscience.iop.org/article/10.1088/1367-2630/aad1ea.

[7] Jonathan P. Dowling and Gerard J. Milburn. Quantum technology: the second quantum revolution. Philosophical Transactions of the Royal Society of London. Series A: Mathematical, Physical and Engineering Sciences, 361 (1809):1655–1674, August 2003. ISSN 1364-503X, 1471-2962. doi: 10.1098/rsta.2003.1227. URL https://royalsocietypublishing.org/doi/10.1098/rsta.2003.1227.

[8] Jeremy L. O'Brien, Akira Furusawa, and Jelena Vučković. Photonic quantum technologies. Nature Photon, 3(12):687–695, December 2009. ISSN 1749-4885, 1749-4893. doi: 10.1038/nphoton.2009.229. URL http://www.nature.com/articles/nphoton.2009.229.

[9] Dan Browne, Sougato Bose, Florian Mintert, and M.S. Kim. From quantum optics to quantum technologies. Progress in Quantum Electronics, 54:2–18, August 2017. ISSN 00796727. doi: 10.1016/j.pquantelec.2017.06.002. URL https://linkinghub.elsevier.com/retrieve/pii/S0079672717300186.

[10] J. Ignacio Cirac and H. Jeff Kimble. Quantum optics, what next? Nature Photon, 11(1):18–20, January 2017. ISSN 1749-4885, 1749-4893. doi: 10.1038/nphoton.2016.259. URL http://www.nature.com/articles/nphoton.2016.259.

[11] E. Knill, R. Laflamme, and G. J. Milburn. A scheme for efficient quantum computation with linear optics. Nature, 409(6816):46–52, January 2001. ISSN 0028-0836, 1476-4687. doi: 10.1038/35051009. URL http://www.nature.com/articles/35051009.

[12] Alán Aspuru-Guzik and Philip Walther. Photonic quantum simulators. Nature Phys, 8(4):285–291, April 2012. ISSN 1745-2473, 1745-2481. doi: 10.1038/nphys2253. URL http://www.nature.com/articles/nphys2253.

[13] Nicolas Gisin and Rob Thew. Quantum communication. Nature Photon, 1(3):165–171, March 2007. ISSN 1749-4885, 1749-4893. doi: 10.1038/nphoton.2007.22. URL http://www.nature.com/articles/nphoton.2007.22.

[14] Vittorio Giovannetti, Seth Lloyd, and Lorenzo Maccone. Advances in quantum metrology. Nature Photon, 5(4):222–229, April 2011. ISSN 1749-4885, 1749-4893. doi: 10.1038/nphoton.2011.35. URL http://www.nature.com/articles/nphoton.2011.35.

[15] Joshua W. Silverstone, Damien Bonneau, Jeremy L. O'Brien, and Mark G. Thompson. Silicon Quantum Photonics. IEEE J. Select. Topics Quantum Electron., 22(6):390–402, November 2016. ISSN 1077-260X, 1558-4542. doi: 10.1109/JSTQE.2016.2573218. URL http://ieeexplore.ieee.org/document/7479523/.

[16] Jianwei Wang, Fabio Sciarrino, Anthony Laing, and Mark G. Thompson. Integrated photonic quantum technologies. Nat. Photonics, 14(5):273–284, May 2020. ISSN 1749-4885, 1749-4893. doi: 10.1038/s41566-019-0532-1. URL http://www.nature.com/articles/s41566-019-0532-1.

[17] Kilian Peter Heeg. X-Ray Quantum Optics With Mössbauer Nuclei In Thin-Film Cavities. PhD thesis, 2014. URL http://archiv.ub.uni-heidelberg.de/volltextserver/id/eprint/17869. Publisher: Heidelberg University Library.

[18] Liang Jie Wong and Ido Kaminer. Prospects in x-ray science emerging from quantum optics and nanomaterials. Appl. Phys. Lett., 119(13):130502, September 2021. ISSN 0003-6951, 1077-3118. doi: 10.1063/5.0060552. URL https://aip.scitation.org/doi/10.1063/5.0060552.

[19] Ralf Röhlsberger and Jörg Evers. Quantum Optical Phenomena in Nuclear Resonant Scattering. In Yutaka Yoshida and Guido Langouche, editors, Modern Mössbauer Spectroscopy, volume 137, pages 105–171. Springer Singapore, Singapore, 2021. ISBN 9789811594212 9789811594229. doi: 10.1007/978-981-15-9422-9_3. URL http://link.springer.com/10.1007/978-981-15-9422-9_3. Series Title: Topics in Applied Physics.

[20] Romain Coussement, Rustem Shahkmouratov, Gerda Neyens, and Jos Odeurs. Quantum optics with gamma radiation. Europhysics News, 34(5):190–194, September 2003. ISSN 0531-7479, 1432-1092. doi: 10.1051/epn:2003505. URL http://www.europhysicsnews.org/10.1051/epn:2003505.

[21] G. Neyens, R. Coussement, and J. Odeurs. Quantum optics with nuclear gamma radiation. Hyperfine Interactions, 107(1/4):319–331, 1997. ISSN 03043843. doi: 10.1023/A:1012096815111. URL http://link.springer.com/10.1023/A:1012096815111.

[22] Xiaojing Huang, Hanfei Yan, Evgeny Nazaretski, Raymond Conley, Nathalie Bouet, Juan Zhou, Kenneth Lauer, Li Li, Daejin Eom, Daniel Legnini, Ross Harder, Ian K. Robinson, and Yong S. Chu. 11 nm hard X-ray focus from a large-aperture multilayer Laue lens. Sci Rep, 3(1):3562, December 2013. ISSN 2045-2322. doi: 10.1038/srep03562. URL http://www.nature.com/articles/srep03562.

[23] J. Arthur, G. Materlik, R. Tatchyn, and H. Winick. The LCLS: A fourth generation light source using the SLAC linac. Review of Scientific Instruments, 66(2):1987–1989, February 1995. ISSN 0034-6748, 1089-7623. doi: 10.1063/1.1145778. URL http://aip.scitation.org/doi/10.1063/1.1145778.

[24] Thomas Tschentscher, Christian Bressler, Jan Grünert, Anders Madsen, Adrian Mancuso, Michael Meyer, Andreas Scherz, Harald Sinn, and Ulf Zastrau. Photon Beam Transport and Scientific Instruments at the European XFEL. Applied Sciences, 7(6):592, June 2017. ISSN 2076-3417. doi: 10.3390/app7060592. URL http://www.mdpi.com/2076-3417/7/6/592.

[25] Brian W. J. McNeil and Neil R. Thompson. X-ray free-electron lasers. Nature Photon, 4(12):814–821, December 2010. ISSN 1749-4885, 1749-4893. doi: 10.1038/nphoton.2010.239. URL http://www.nature.com/articles/nphoton.2010.239.

[26] Bernhard Adams, Gabriel Aeppli, Thomas Allison, Alfred Q. R. Baron, Phillip Bucksbaum, Aleksandr I. Chumakov, Christopher Corder, Stephen P. Cramer, Serena DeBeer, Yuntao Ding, Jörg Evers, Josef Frisch, Matthias Fuchs, Gerhard Grübel, Jerome B. Hastings, Christoph M. Heyl, Leo Holberg, Zhirong Huang, Tetsuya Ishikawa, Andreas Kaldun, Kwang-Je Kim, Tomasz Kolodziej, Jacek Krzywinski, Zheng Li, Wen-Te Liao, Ryan Lindberg, Anders Madsen, Timothy Maxwell, Giulio Monaco, Keith Nelson, Adriana Palffy, Gil Porat, Weilun Qin, Tor Raubenheimer, David A. Reis, Ralf Röhlsberger, Robin Santra, Robert Schoenlein, Volker Schünemann, Oleg Shpyrko, Yuri Shvyd'ko, Sharon Shwartz, Andrej Singer, Sunil K. Sinha, Mark Sutton, Kenji Tamasaku, Hans-Christian Wille, Makina Yabashi, Jun Ye, and Diling Zhu. Scientific Opportunities with an X-ray Free-Electron Laser Oscillator. arXiv:1903.09317 [physics.ins-det], March 2019. URL http://arxiv.org/abs/1903.09317.

[27] Bernhard W. Adams, Christian Buth, Stefano M. Cavaletto, Jörg Evers, Zoltán Harman, Christoph H. Keitel, Adriana Pálffy, Antonio Picón, Ralf Röhlsberger, Yuri Rostovtsev, and Kenji Tamasaku. X-ray quantum optics. Journal of Modern Optics, 60(1):2–21, January 2013. ISSN 0950-0340, 1362-3044. doi: 10.1080/09500340.2012.752113. URL http://www.tandfonline.com/doi/abs/10.1080/09500340.2012.752113.

[28] Dominik Lentrodt. Ab initio approaches to x-ray cavity QED - From multi-mode theory to nonlinear dynamics of Mössbauer nuclei. 2021. doi: 10.11588/HEIDOK.00030671. URL https://archiv.ub.uni-heidelberg.de/volltextserver/id/eprint/30671. Publisher: Heidelberg University Library.

[29] F. G. Vagizov. The splitting of hyperfine lines of57Fe nuclei in RF magnetic field. Hyperfine Interact, 61(1-4):1359–1362, August 1990. ISSN 0304-3834, 1572-9540. doi: 10.1007/BF02407625. URL http://link.springer.com/10.1007/BF02407625.

[30] Ilkka Tittonen, Mikk Lippmaa, Panu Helistö, and Toivo Katila. Stepwise phase modulation of recoilless gamma radiation in a coincidence experiment: Gamma echo. Phys. Rev. B, 47(13):7840–7846, April 1993. ISSN 0163-1829, 1095-3795. doi: 10.1103/PhysRevB.47.7840. URL https://link.aps.org/doi/10.1103/PhysRevB.47.7840.

[31] M. Lippmaa, I. Tittonen, J. Lindén, and T. Katila. Mössbauer-NMR double resonance. Phys. Rev. B, 52(14):10268–10277, October 1995. ISSN 0163-1829, 1095-3795. doi: 10.1103/PhysRevB.52.10268. URL https://link.aps.org/doi/10.1103/PhysRevB.52.10268.

[32] Yu. V. Shvyd'ko, T. Hertrich, U. van Bürck, E. Gerdau, O. Leupold, J. Metge, H. D. Rüter, S. Schwendy, G. V. Smirnov, W. Potzel, and P. Schindelmann. Storage of Nuclear Excitation Energy through Magnetic Switching. Phys. Rev. Lett., 77(15):3232–3235, October 1996. ISSN 0031-9007, 1079-7114. doi: 10.1103/PhysRevLett.77.3232. URL https://link.aps.org/doi/10.1103/PhysRevLett.77.3232.

[33] J. Odeurs, R. Coussement, K. Vyvey, H. Muramatsu, S. Gheysen, R. Callens, G. Neyens, I. Serdons, R. N. Shakhmuratov, Y. Rostovtsev, and O. Kocharovskaya. Induced Transparency for Gamma Radiation via Nuclear Level Mixing. Hyperfine Interactions, 143(1):97–110, November 2002. ISSN 1572-9540. doi: 10.1023/A:1024029517332. URL https://doi.org/10.1023/A:1024029517332.

[34] Farit Vagizov, Vladimir Antonov, Y. V. Radeonychev, R. N. Shakhmuratov, and Olga Kocharovskaya. Coherent control of the waveforms of recoilless γ-ray photons. Nature, 508(7494):80–83, April 2014. ISSN 0028-0836, 1476-4687. doi: 10.1038/nature13018. URL http://www.nature.com/articles/nature13018.

[35] Wen-Te Liao, Christoph H. Keitel, and Adriana Pálffy. X-ray-generated heralded macroscopical quantum entanglement of two nuclear ensembles. Sci Rep, 6(1):33361, December 2016. ISSN 2045-2322. doi: 10.1038/srep33361. URL http://www.nature.com/articles/srep33361.

[36] K. P. Heeg, A. Kaldun, C. Strohm, P. Reiser, C. Ott, R. Subramanian, D. Lentrodt, J. Haber, H.-C. Wille, S. Goerttler, R. Rüffer, C. H. Keitel, R. Röhlsberger, T. Pfeifer, and J. Evers. Spectral narrowing of x-ray pulses for precision spectroscopy with nuclear resonances. Science, 357(6349):375–378, July 2017. ISSN 0036-8075, 1095-9203. doi: 10.1126/science.aan3512. URL https://www.sciencemag.org/lookup/doi/10.1126/science.aan3512.

[37] S. Sakshath, K. Jenni, L. Scherthan, P. Würtz, M. Herlitschke, I. Sergeev, C. Strohm, H.-C. Wille, R. Röhlsberger, J. A. Wolny, and V. Schünemann. Optical pump - nuclear resonance probe experiments on spin crossover complexes. Hyperfine Interact, 238(1):89, November 2017. ISSN 0304-3843, 1572-9540. doi: 10.1007/s10751-017-1461-3. URL http://link.springer.com/10.1007/s10751-017-1461-3.

[38] Aleksandr I. Chumakov, Alfred Q. R. Baron, Ilya Sergueev, Cornelius Strohm, Olaf Leupold, Yuri Shvyd'ko, Gennadi V. Smirnov, Rudolf Rüffer, Yuichi Inubushi, Makina Yabashi, Kensuke Tono, Togo Kudo, and Tetsuya Ishikawa. Superradiance of an ensemble of nuclei excited by a free electron laser. Nature Phys, 14(3):261–264, March 2018. ISSN 1745-2473, 1745-2481. doi: 10.1038/s41567-017-0001-z. URL http://www.nature.com/articles/s41567-017-0001-z.

[39] Kilian P. Heeg, Andreas Kaldun, Cornelius Strohm, Christian Ott, Rajagopalan Subramanian, Dominik Lentrodt, Johann Haber, Hans-Christian Wille, Stephan Goerttler, Rudolf Rüffer, Christoph H. Keitel, Ralf Röhlsberger, Thomas Pfeifer, and Jörg Evers. Coherent X-ray-optical control of nuclear excitons. Nature, 590(7846):401–404, February 2021. ISSN 0028-0836, 1476-4687. doi: 10.1038/s41586-021-03276-x. URL http://www.nature.com/articles/s41586-021-03276-x.

[40] Lars Bocklage, Jakob Gollwitzer, Cornelius Strohm, Christian F. Adolff, Kai Schlage, Ilya Sergeev, Olaf Leupold, Hans-Christian Wille, Guido Meier, and Ralf Röhlsberger. Coherent control of collective nuclear quantum states via transient magnons. Sci. Adv., 7(5):eabc3991, January 2021. ISSN 2375-2548. doi: 10.1126/sciadv.abc3991. URL https://advances.sciencemag.org/lookup/doi/10.1126/sciadv.abc3991.

[41] Yu-Hsueh Chen, Po-Han Lin, Guan-Ying Wang, Adriana Pálffy, and Wen-Te Liao. Transient nuclear inversion by X-Ray Free Electron Laser in a tapered x-ray waveguid. arXiv:2104.09624 [physics.optics], April 2021. URL http://arxiv.org/abs/2104.09624.

[42] Douglas Adams. Life, the universe and everything. Ballantine Books, New York, 2005. ISBN 978-0-345-39182-7. OCLC: 156753992.

[43] Rudolf L. Mössbauer. Kernresonanzabsorption von γ-Strahlung in Ir191. Zeitschrift für Naturforschung A, 14(3):211–216, March 1959. ISSN 1865-7109, 0932-0784. doi: 10.1515/zna-1959-0303. URL https://www.degruyter.com/document/doi/10.1515/zna-1959-0303/html.

[44] J.P. Hannon and G.T. Trammell. Coherent γ-ray optics. Hyperfine Interactions, 123-124(1-4):127–274, 1999. ISSN 0304-3843. doi: 10.1023/A:1017011621007.

[45] G. V. Smirnov. Coherent Nuclear Resonance Fluorescence. In G. Kalvius and P. Kienle, editors, The Rudolf Mössbauer Story: His Scientific Work and Its Impact on Science and History. Springer-Verlag Berlin Heidelberg, Berlin, 2012. ISBN 978-3-642-17952-5.

[46] Ralf Röhlsberger. Nuclear Condensed Matter Physics with Synchrotron Radiation, volume 208 of Springer Tracts in Modern Physics. Springer Berlin Heidelberg, Berlin, Heidelberg, 2005. ISBN 978-3-540-23244-5 978-3-540-44699-6. doi: 10.1007/b86125. URL http://link.springer.com/10.1007/b86125.

[47] R. H. Dicke. Coherence in Spontaneous Radiation Processes. Phys. Rev., 93 (1):99–110, January 1954. ISSN 0031-899X. doi: 10.1103/PhysRev.93.99. URL https://link.aps.org/doi/10.1103/PhysRev.93.99.

[48] Dominik Lentrodt, Kilian P. Heeg, Christoph H. Keitel, and Jörg Evers. *Ab initio* quantum models for thin-film x-ray cavity QED. Phys. Rev. Research, 2(2):023396, June 2020. ISSN 2643-1564. doi: 10.1103/PhysRevResearch.2.023396. URL https://link.aps.org/doi/10.1103/PhysRevResearch.2.023396.

[49] Kilian P. Heeg and Jörg Evers. X-ray quantum optics with Mössbauer nuclei embedded in thin-film cavities. Phys. Rev. A, 88(4):043828, October 2013. ISSN 1050-2947, 1094-1622. doi: 10.1103/PhysRevA.88.043828. URL https://link.aps.org/doi/10.1103/PhysRevA.88.043828.

[50] R. Röhlsberger, K. Schlage, B. Sahoo, S. Couet, and R. Ruffer. Collective Lamb Shift in Single-Photon Superradiance. Science, 328(5983):1248–1251, June 2010. ISSN 0036-8075, 1095-9203. doi: 10.1126/science.1187770. URL https://www.sciencemag.org/lookup/doi/10.1126/science.1187770.

[51] Ralf Röhlsberger, Hans-Christian Wille, Kai Schlage, and Balaram Sahoo. Electromagnetically induced transparency with resonant nuclei in a cavity. Nature, 482(7384):199–203, February 2012. ISSN 0028-0836, 1476-4687. doi: 10.1038/nature10741. URL http://www.nature.com/articles/nature10741.

[52] Kilian P. Heeg, Hans-Christian Wille, Kai Schlage, Tatyana Guryeva, Daniel Schumacher, Ingo Uschmann, Kai S. Schulze, Berit Marx, Tino Kämpfer, Gerhard G. Paulus, Ralf Röhlsberger, and Jörg Evers. Vacuum-Assisted Generation and Control of Atomic Coherences at X-Ray Energies. Phys. Rev. Lett., 111(7):073601, August 2013. ISSN 0031-9007, 1079-7114. doi: 10.1103/PhysRevLett.111.073601. URL https://link.aps.org/doi/10.1103/PhysRevLett.111.073601.

[53] Johann Haber, Kai S. Schulze, Kai Schlage, Robert Loetzsch, Lars Bocklage, Tatiana Gurieva, Hendrik Bernhardt, Hans-Christian Wille, Rudolf Rüffer, Ingo Uschmann, Gerhard G. Paulus, and Ralf Röhlsberger. Collective strong coupling of X-rays and nuclei in a nuclear optical lattice. Nature Photon, 10(7): 445–449, July 2016. ISSN 1749-4885, 1749-4893. doi: 10.1038/nphoton.2016.77. URL http://www.nature.com/articles/nphoton.2016.77.

[54] Johann Haber, Xiangjin Kong, Cornelius Strohm, Svenja Willing, Jakob Gollwitzer, Lars Bocklage, Rudolf Rüffer, Adriana Pálffy, and Ralf Röhlsberger. Rabi oscillations of X-ray radiation between two nuclear ensembles. Nature Photon, 11(11):720–725, November 2017. ISSN 1749-4885, 1749-4893. doi: 10.1038/s41566-017-0013-3. URL http://www.nature.com/articles/s41566-017-0013-3.

[55] Kilian P. Heeg, Johann Haber, Daniel Schumacher, Lars Bocklage, Hans-Christian Wille, Kai S. Schulze, Robert Loetzsch, Ingo Uschmann, Gerhard G. Paulus, Rudolf Rüffer, Ralf Röhlsberger, and Jörg Evers. Tunable Subluminal Propagation of Narrow-band X-Ray Pulses. Phys. Rev. Lett., 114(20):203601, May 2015. ISSN 0031-9007, 1079-7114. doi: 10.1103/PhysRevLett.114.203601. URL https://link.aps.org/doi/10.1103/PhysRevLett.114.203601.

[56] Kilian P. Heeg and Jörg Evers. Collective effects between multiple nuclear ensembles in an x-ray cavity-QED setup. Phys. Rev. A, 91(6):063803, June 2015. ISSN 1050-2947, 1094-1622. doi: 10.1103/PhysRevA.91.063803. URL https://link.aps.org/doi/10.1103/PhysRevA.91.063803.

[57] Xiangjin Kong, Darrick E. Chang, and Adriana Pálffy. Green's-function formalism for resonant interaction of x rays with nuclei in structured media. Phys. Rev. A, 102(3):033710, September 2020. ISSN 2469-9926, 2469-9934. doi: 10.1103/PhysRevA.102.033710. URL https://link.aps.org/doi/10.1103/PhysRevA.102.033710.

[58] M. S. Tomaš. Green function for multilayers: Light scattering in planar cavities. Phys. Rev. A, 51(3):2545–2559, March 1995. ISSN 1050-2947, 1094-1622. doi: 10.1103/PhysRevA.51.2545. URL https://link.aps.org/doi/10.1103/PhysRevA.51.2545.

[59] Sean Molesky, Zin Lin, Alexander Y. Piggott, Weiliang Jin, Jelena Vuković, and Alejandro W. Rodriguez. Inverse design in nanophotonics. Nature Photon, 12(11):659–670, November 2018. ISSN 1749-4885, 1749-4893. doi: 10.1038/s41566-018-0246-9. URL http://www.nature.com/articles/s41566-018-0246-9.

[60] Robert Bennett and Stefan Yoshi Buhmann. Inverse design of light–matter interactions in macroscopic QED. New J. Phys., 22(9):093014, September 2020. ISSN 1367-2630. doi: 10.1088/1367-2630/abac3a. URL https://iopscience.iop.org/article/10.1088/1367-2630/abac3a.

[61] Robert Bennett. Inverse design of environment-induced coherence. Phys. Rev. A, 103(1):013706, January 2021. ISSN 2469-9926, 2469-9934. doi:

10.1103/PhysRevA.103.013706. URL https://link.aps.org/doi/10.1103/PhysRevA.103.013706.

[62] Michael Fleischhauer, Atac Imamoglu, and Jonathan P. Marangos. Electromagnetically induced transparency: Optics in coherent media. Rev. Mod. Phys., 77 (2):633–673, July 2005. ISSN 0034-6861, 1539-0756. doi: 10.1103/RevModPhys.77.633. URL https://link.aps.org/doi/10.1103/RevModPhys.77.633.

[63] K.-J. Boller, A. Imamoğlu, and S. E. Harris. Observation of electromagnetically induced transparency. Phys. Rev. Lett., 66(20):2593–2596, May 1991. ISSN 0031-9007. doi: 10.1103/PhysRevLett.66.2593. URL https://link.aps.org/doi/10.1103/PhysRevLett.66.2593.

[64] L. G. Parratt. Surface Studies of Solids by Total Reflection of X-Rays. Phys. Rev., 95(2):359–369, July 1954. ISSN 0031-899X. doi: 10.1103/PhysRev.95.359. URL https://link.aps.org/doi/10.1103/PhysRev.95.359.

[65] Jens Als-Nielsen and Des McMorrow. Elements of modern X-ray physics. Wiley, Chichester, 2nd edition, 2011. ISBN 978-1-119-99731-3 978-0-470-97394-3 978-0-470-97395-0 978-1-119-99836-5 978-1-119-97015-6 978-1-119-97016-3. OCLC: 746250800.

[66] George B. Arfken, Hans-Jurgen Weber, and Frank E. Harris. Mathematical methods for physicists: a comprehensive guide. Elsevier, Amsterdam ; Boston, 7th edition, 2013. ISBN 978-0-12-384654-9.

[67] Philippe Lalanne, Wei Yan, Kevin Vynck, Christophe Sauvan, and Jean-Paul Hugonin. Light Interaction with Photonic and Plasmonic Resonances. Laser & Photonics Reviews, 12(5):1700113, May 2018. ISSN 18638880. doi: 10.1002/lpor.201700113. URL https://onlinelibrary.wiley.com/doi/10.1002/lpor.201700113.

[68] Mittag-Leffler's Expansion Theorem, November 2021. URL https://proofwiki.org/wiki/Mittag-Leffler's_Expansion_Theorem. accessed 22.11.2021.

[69] A. Asenjo-Garcia, J. D. Hood, D. E. Chang, and H. J. Kimble. Atom-light interactions in quasi-one-dimensional nanostructures: A Green's-function perspective. Phys. Rev. A, 95(3):033818, March 2017. ISSN 2469-9926, 2469-9934. doi: 10.1103/PhysRevA.95.033818. URL https://link.aps.org/doi/10.1103/PhysRevA.95.033818.

[70] Stefan Yoshi Buhmann. Dispersion Forces I, volume 247 of Springer Tracts in Modern Physics. Springer Berlin Heidelberg, Berlin, Heidelberg, 2012. ISBN

978-3-642-32483-3 978-3-642-32484-0. doi: 10.1007/978-3-642-32484-0. URL http://link.springer.com/10.1007/978-3-642-32484-0.

[71] R. Friedberg, S.R. Hartmann, and J.T. Manassah. Frequency shifts in emission and absorption by resonant systems ot two-level atoms. Physics Reports, 7(3):101–179, March 1973. ISSN 03701573. doi: 10.1016/0370-1573(73)90001-X. URL https://linkinghub.elsevier.com/retrieve/pii/037015737390001X.

[72] Marlan O. Scully. Collective Lamb Shift in Single Photon Dicke Superradiance. Phys. Rev. Lett., 102(14):143601, April 2009. ISSN 0031-9007, 1079-7114. doi: 10.1103/PhysRevLett.102.143601. URL https://link.aps.org/doi/10.1103/PhysRevLett.102.143601.

[73] Janne Ruostekoski and Juha Javanainen. Emergence of correlated optics in one-dimensional waveguides for classical and quantum atomic gases. Phys. Rev. Lett., 117(14):143602, September 2016. ISSN 0031-9007, 1079-7114. doi: 10.1103/PhysRevLett.117.143602. URL https://link.aps.org/doi/10.1103/PhysRevLett.117.143602.

[74] J. Keaveney, A. Sargsyan, U. Krohn, I. G. Hughes, D. Sarkisyan, and C. S. Adams. Cooperative Lamb Shift in an Atomic Vapor Layer of Nanometer Thickness. Phys. Rev. Lett., 108(17):173601, April 2012. ISSN 0031-9007, 1079-7114. doi: 10.1103/PhysRevLett.108.173601. URL https://link.aps.org/doi/10.1103/PhysRevLett.108.173601.

[75] W. Guerin, M.T. Rouabah, and R. Kaiser. Light interacting with atomic ensembles: collective, cooperative and mesoscopic effects. Journal of Modern Optics, 64(9):895–907, May 2017. ISSN 0950-0340, 1362-3044. doi: 10.1080/09500340.2016.1215564. URL https://www.tandfonline.com/doi/full/10.1080/09500340.2016.1215564.

[76] T. Peyrot, Y. R. P. Sortais, A. Browaeys, A. Sargsyan, D. Sarkisyan, J. Keaveney, I. G. Hughes, and C. S. Adams. Collective Lamb Shift of a Nanoscale Atomic Vapor Layer within a Sapphire Cavity. Phys. Rev. Lett., 120(24):243401, June 2018. ISSN 0031-9007, 1079-7114. doi: 10.1103/PhysRevLett.120.243401. URL https://link.aps.org/doi/10.1103/PhysRevLett.120.243401.

[77] S. J. Roof, K. J. Kemp, M. D. Havey, and I. M. Sokolov. Observation of Single-Photon Superradiance and the Cooperative Lamb Shift in an Extended Sample of Cold Atoms. Phys. Rev. Lett., 117(7):073003, August 2016. ISSN 0031-9007, 1079-7114. doi: 10.1103/PhysRevLett.117.073003. URL https://link.aps.org/doi/10.1103/PhysRevLett.117.073003.

[78] S. L. Bromley, B. Zhu, M. Bishof, X. Zhang, T. Bothwell, J. Schachenmayer, T. L. Nicholson, R. Kaiser, S. F. Yelin, M. D. Lukin, A. M. Rey, and J. Ye. Collective atomic scattering and motional effects in a dense coherent medium. Nat Commun, 7(1):11039, April 2016. ISSN 2041-1723. doi: 10.1038/ncomms11039. URL http://www.nature.com/articles/ncomms11039.

[79] M. Gross and S. Haroche. Superradiance: An essay on the theory of collective spontaneous emission. Physics Reports, 93(5):301–396, December 1982. ISSN 03701573. doi: 10.1016/0370-1573(82)90102-8. URL https://linkinghub.elsevier.com/retrieve/pii/0370157382901028.

[80] M. O. Scully and A. A. Svidzinsky. The Super of Superradiance. Science, 325 (5947):1510–1511, September 2009. ISSN 0036-8075, 1095-9203. doi: 10.1126/science.1176695. URL https://www.sciencemag.org/lookup/doi/10.1126/science.1176695.

[81] Barry M. Garraway. The Dicke model in quantum optics: Dicke model revisited. Phil. Trans. R. Soc. A., 369(1939):1137–1155, March 2011. ISSN 1364-503X, 1471-2962. doi: 10.1098/rsta.2010.0333. URL https://royalsocietypublishing.org/doi/10.1098/rsta.2010.0333.

[82] K. P. Heeg, C. Ott, D. Schumacher, H.-C. Wille, R. Röhlsberger, T. Pfeifer, and J. Evers. Interferometric phase detection at x-ray energies via Fano resonance control. Phys. Rev. Lett., 114(20):207401, May 2015. ISSN 0031-9007, 1079-7114. doi: 10.1103/PhysRevLett.114.207401. URL https://link.aps.org/doi/10.1103/PhysRevLett.114.207401.

[83] C. Ott, A. Kaldun, P. Raith, K. Meyer, M. Laux, J. Evers, C. H. Keitel, C. H. Greene, and T. Pfeifer. Lorentz Meets Fano in Spectral Line Shapes: A Universal Phase and Its Laser Control. Science, 340(6133):716–720, May 2013. ISSN 0036-8075, 1095-9203. doi: 10.1126/science.1234407. URL https://www.sciencemag.org/lookup/doi/10.1126/science.1234407.

[84] Mikhail F. Limonov, Mikhail V. Rybin, Alexander N. Poddubny, and Yuri S. Kivshar. Fano resonances in photonics. Nature Photon, 11(9):543–554, September 2017. ISSN 1749-4885, 1749-4893. doi: 10.1038/nphoton.2017.142. URL http://www.nature.com/articles/nphoton.2017.142.

[85] Malte Vassholz and Tim Salditt. Observation of electron-induced characteristic x-ray and bremsstrahlung radiation from a waveguide cavity. Sci. Adv., 7(4):eabd5677, January 2021. ISSN 2375-2548. doi: 10.1126/sciadv.abd5677. URL https://advances.sciencemag.org/lookup/doi/10.1126/sciadv.abd5677.

[86] Lukas Novotny and Bert Hecht. Principles of Nano-Optics. Cambridge University Press, Cambridge, 2006. ISBN 978-0-511-81353-5. doi: 10.1017/CBO9780511813535. URL http://ebooks.cambridge.org/ref/id/CBO9780511813535.

[87] Mikhail V. Rybin, Sergei F. Mingaleev, Mikhail F. Limonov, and Yuri S. Kivshar. Purcell effect and Lamb shift as interference phenomena. Sci Rep, 6(1):20599, August 2016. ISSN 2045-2322. doi: 10.1038/srep20599. URL http://www.nature.com/articles/srep20599.

[88] Paolo Longo, Christoph H. Keitel, and Jörg Evers. Tailoring superradiance to design artificial quantum systems. Sci Rep, 6(1):23628, April 2016. ISSN 2045-2322. doi: 10.1038/srep23628. URL http://www.nature.com/articles/srep23628.

[89] Nihal Yılmaz Özgür. On the Circle Preserving Property of Möbius Transformations. In Themistocles M. Rassias and Panos M. Pardalos, editors, Mathematics Without Boundaries, pages 397–413. Springer New York, New York, NY, 2014. ISBN 978-1-4939-1105-9 978-1-4939-1106-6. doi: 10.1007/978-1-4939-1106-6_17. URL http://link.springer.com/10.1007/978-1-4939-1106-6_17.

[90] K. P. Heeg. PYNUSS. private communication.

[91] F. Pfeiffer. Two-Dimensional X-ray Waveguides and Point Sources. Science, 297(5579):230–234, July 2002. ISSN 00368075, 10959203. doi: 10.1126/science.1071994. URL https://www.sciencemag.org/lookup/doi/10.1126/science.1071994.

[92] A. Jarre, C. Fuhse, C. Ollinger, J. Seeger, R. Tucoulou, and T. Salditt. Two-Dimensional Hard X-Ray Beam Compression by Combined Focusing and Waveguide Optics. Phys. Rev. Lett., 94(7):074801, February 2005. ISSN 0031-9007, 1079-7114. doi: 10.1103/PhysRevLett.94.074801. URL https://link.aps.org/doi/10.1103/PhysRevLett.94.074801.

[93] Ralf Röhlsberger, Jörg Evers, and Sharon Shwartz. Quantum and Nonlinear Optics with Hard X-Rays. In Eberhard J. Jaeschke, Shaukat Khan, Jochen R. Schneider, and Jerome B. Hastings, editors, Synchrotron Light Sources and Free-Electron Lasers, pages 1399–1431. Springer International Publishing, Cham, 2020. ISBN 978-3-030-23200-9 978-3-030-23201-6. doi: 10.1007/978-3-030-23201-6_32. URL http://link.springer.com/10.1007/978-3-030-23201-6_32.

[94] Ralf Röhlsberger. Grazing Incidence Optics for Nuclear Resonant Filtering of Synchrotron Radiation, 1994. phd thesis, DESY HASYLAB 94-06.

[95] Petr M. Anisimov, Jonathan P. Dowling, and Barry C. Sanders. Objectively Discerning Autler-Townes Splitting from Electromagnetically Induced Transparency. Phys. Rev. Lett., 107(16):163604, October 2011. ISSN 0031-9007, 1079-7114. doi: 10.1103/PhysRevLett.107.163604. URL https://link.aps.org/doi/10.1103/PhysRevLett.107.163604.

[96] Ramy El-Ganainy, Konstantinos G. Makris, Mercedeh Khajavikhan, Ziad H. Musslimani, Stefan Rotter, and Demetrios N. Christodoulides. Non-Hermitian physics and PT symmetry. Nature Phys, 14(1):11–19, January 2018. ISSN 1745-2473, 1745-2481. doi: 10.1038/nphys4323. URL http://www.nature.com/articles/nphys4323.

[97] Mohammad-Ali Miri and Andrea Alù. Exceptional points in optics and photonics. Science, 363(6422):eaar7709, January 2019. ISSN 0036-8075, 1095-9203. doi: 10.1126/science.aar7709. URL https://www.science.org/doi/10.1126/science.aar7709.

[98] Dominik Lentrodt. Multi-mode effects from spectral overlap in weakly coupled cavity QED. Technical report, February 2021. private communications.

[99] SciPy 1.0 Contributors, Pauli Virtanen, Ralf Gommers, Travis E. Oliphant, Matt Haberland, Tyler Reddy, David Cournapeau, Evgeni Burovski, Pearu Peterson, Warren Weckesser, Jonathan Bright, Stéfan J. van der Walt, Matthew Brett, Joshua Wilson, K. Jarrod Millman, Nikolay Mayorov, Andrew R. J. Nelson, Eric Jones, Robert Kern, Eric Larson, C J Carey, İlhan Polat, Yu Feng, Eric W. Moore, Jake VanderPlas, Denis Laxalde, Josef Perktold, Robert Cimrman, Ian Henriksen, E. A. Quintero, Charles R. Harris, Anne M. Archibald, Antônio H. Ribeiro, Fabian Pedregosa, and Paul van Mulbregt. SciPy 1.0: fundamental algorithms for scientific computing in Python. Nat Methods, 17(3):261–272, March 2020. ISSN 1548-7091, 1548-7105. doi: 10.1038/s41592-019-0686-2. URL http://www.nature.com/articles/s41592-019-0686-2.

[100] Andrew Sarangan. Optical thin film design. 2021. ISBN 978-0-429-42335-2 978-0-429-75175-2 978-0-429-75174-5 978-0-429-75173-8. URL https://www.taylorfrancis.com/books/9780429423352. OCLC: 1153339064.

[101] S. Cabrini, A. Carpentiero, R. Kumar, L. Businaro, P. Candeloro, M. Prasciolu, A. Gosparini, C. Andreani, M. De Vittorio, T. Stomeo, and E. Di Fabrizio. Focused ion beam lithography for two dimensional array structures for photonic applications. Microelectronic Engineering, 78-79:11–15, March 2005. ISSN 01679317. doi: 10.1016/j.mee.2004.12.006. URL https://linkinghub.elsevier.com/retrieve/pii/S0167931704005404.

[102] M. Campbell, D. N. Sharp, M. T. Harrison, R. G. Denning, and A. J. Turberfield. Fabrication of photonic crystals for the visible spectrum by holographic lithography. Nature, 404(6773):53–56, March 2000. ISSN 0028-0836, 1476-4687. doi: 10.1038/35003523. URL http://www.nature.com/articles/35003523.

[103] C. Tokgoz and G. Dural. Closed-form Green's functions for cylindrically stratified media. IEEE Trans. Microwave Theory Techn., 48(1):40–49, January 2000. ISSN 00189480. doi: 10.1109/22.817470. URL http://ieeexplore.ieee.org/document/817470/.

[104] K. P. Heeg, C. H. Keitel, and J. Evers. Inducing and detecting collective population inversions of Mössbauer nuclei. arXiv:1607.04116 [quant-ph], July 2016. URL http://arxiv.org/abs/1607.04116.

[105] Johann Haber, Jakob Gollwitzer, Sonia Francoual, Martin Tolkiehn, Jörg Strempfer, and Ralf Röhlsberger. Spectral Control of an X-Ray L -Edge Transition via a Thin-Film Cavity. Phys. Rev. Lett., 122(12):123608, March 2019. ISSN 0031-9007, 1079-7114. doi: 10.1103/PhysRevLett.122.123608. URL https://link.aps.org/doi/10.1103/PhysRevLett.122.123608.

Erklärung:

Ich versichere, dass ich diese Arbeit selbstständig verfasst habe und keine anderen als die angegebenen Quellen und Hilfsmittel benutzt habe.

Heidelberg, den 30.11.2021